Simulation of realistic ground roll via 2-D finite-difference elastic seismic-wave propagation modeling with irregular near-surface

Ing. Ivan Javier Sánchez Galvis

Universidad Industrial de Santander
Facultad de Ingenierías Físico-Mecánicas
Escuela de Ingenierías Eléctrica, Electrónica y de Telecomunicaciones
Bucaramanga
2017

Simulation of realistic ground roll via 2-D finite-difference elastic seismic-wave propagation modeling with irregular near-surface

COLCIENCIAS
Ciencia, Tecnología e Innovación

ecopetrol
ENERGÍA PARA EL FUTURO

Ing. Ivan Javier Sánchez Galvis

Trabajo de investigación para obtener el título de
Maestría en Ingeniería Electrónica

Director
PhD. Daniel Alfonso Sierra Bueno

Codirector
PhD. César Antonio Duarte Gualdrón

Universidad Industrial de Santander
Facultad de Ingenierías Físico-Mecánicas
Escuela de Ingenierías Eléctrica, Electrónica y de Telecomunicaciones
Bucaramanga
2017

A Mayra Alejandra. Porque ahora somos uno solo. Un mismo sueño, un mismo camino y un mismo sentir. TE AMO.

Acknowledgements

Todo en mi vida se lo debo a Dios. Por eso quiero empezar esta sección agradeciendo a aquel que me creó y trazó un propósito para mi vida. La Santa Biblia dice en Eclesiastés 5:7 "Donde abundan los sueños, también abundan las vanidades y las muchas palabras; mas tú, teme a Dios." Le he creído a Dios, y Él ha cumplido mis sueños. Muchas gracias Señor.

Ahora quiero agradecer a todas aquellas personas que aportaron su tiempo y conocimiento en este trabajo. A mis directores, el profesor Daniel Sierra y el profesor César Duarte, por sus valiosos aportes para hacer de este trabajo, una investigación de buena calidad. Al Doctor William Agudelo, por su sapiencia en temas de geofísica y su gran habilidad para enfocar las ideas a un propósito claro. Al profesor Carlos Niño y al ingeniero Saúl Guevara, que aportaron sus muy buenas ideas en diferentes conversaciones. A Jheyston Serrano y Yenni Villa, por su trabajo en algunos de los capítulos de este libro. A David Rincón, por las conversaciones que tuvimos, que en muchos casos abrieron el escenario de posibilidades para desarrollar esta investigación. A los estudiantes, y ahora ingenieros, Yesid, Arnold y Edwin; quienes trabajaron y aportaron en este trabajo.

Finalmente, agradezco a toda mi familia por su incondicional apoyo. A mi esposa por su gran amor y comprensión. A mis padres por todo su cariño y a mis hermanos por su entrañable compañía.

A todos, muchas gracias.

Table of contents

List of figures

List of tables

RESUMEN

TÍTULO: SIMULACIÓN DE GROUND ROLL REALISTA MEDIANTE EL MODELADO DE PROPAGACIÓN DE ONDAS SÍSMICAS ELÁSTICAS EN DIFERENCIAS FINITAS 2D CON SUPERFICIE CERCANA IRREGULAR [1]

AUTOR: Ivan Javier Sánchez Galvis [2]

PALABRAS CLAVE: Ondas superficiales, sísmica multicomponente, atributos sísmicos, diferencias finitas.

DESCRIPCIÓN:
El modelado numérico de las ondas elásticas se ha utilizado para estudiar cómo las ondas sísmicas se propagan dentro de la Tierra. Este estudio ha permitido a los geofísicos interpretar los sismogramas para construir una imagen del subsuelo de la Tierra. Los sismogramas son señales que contienen información de los fenómenos físicos presentados en la propagación de las ondas sísmicas (por ejemplo, Reflexiones, refracciones, difracciones, dispersión, dispersión). Esta información se utiliza para estimar las propiedades mecánicas de los materiales de los cuales se forma la Tierra.
En este trabajo, se implementa un método de diferencias finitas 2D con precisión de segundo orden en tiempo y cuarto orden en el espacio para modelar la propagación elástica de ondas sísmicas. La topografía superficial compleja se contempla en los modelos terrestres con el objetivo de producir datos sísmicos sintéticos con comportamiento realista de las ondas superficiales. Se desarrollaron varios experimentos sintéticos de propagación de ondas de superficie a través de modelos terrestres con superficies cercanas irregulares para obtener un rodado de tierra realista. Se realizó una comparación del comportamiento de los atributos sísmicos de las ondas superficiales, entre los datos sísmicos sintéticos y reales para analizar cómo es realista el rodado de tierra simulado. En general, el comportamiento de los atributos sísmicos en los datos sintéticos es similar al comportamiento en los datos de campo. A partir de los experimentos, se muestra que la dispersión, la difusión y la retro-difusión de las ondas superficiales es causada por la topografía de la superficie y el lecho rocoso irregular.

[1] Tesis de Maestría

[2] Facultad de Ingenierías Físico-Mecánicas. Escuela de Ingenierías Eléctrica, Electrónica y de Telecomunicaciones. Director: PhD. Daniel Alfonso Sierra, Codirector: PhD. César Antonio Duarte Gualdrón

ABSTRACT

TITLE: SIMULATION OF REALISTIC GROUND ROLL VIA 2-D FINITE-DIFFERENCE ELASTIC SEISMIC-WAVE PROPAGATION MODELING WITH IRREGULAR NEAR-SURFACE [3]

AUTHOR: Ivan Javier Sánchez Galvis [4]

KEYWORDS: Surface waves, multicomponent seismic, seismic attributes, finite differences.

DESCRIPTION:
Numerical modeling of elastic waves has been used to study how seismic waves are propagated inside the Earth. This study has allowed geophysicists to interpret seismograms in order to build an image of the Earth's subsurface. Seismograms are signals that contains information of physical phenomena presented in seismic waves propagation (eg. Reflections, refractions, diffractions, scattering, dispersion). This information is used to estimate mechanical properties of materials of which the Earth is formed.
In this work, A 2D finite differences method with second order accurate in time and fourth order accurate in space to model elastic seismic-wave propagation is implemented. Complex surface topography is contemplated in the earth models aiming to produce synthetic seismic data with realistic behavior of surface waves. Several synthetic experiments of surface waves propagation through earth models with irregular near-surface to obtain realistic ground roll were developed. A comparison of the behavior of the seismic attributes of the surface waves, between synthetic and real seismic data to analyze how realistic is the simulated ground-roll, was performed. In general, the seismic attributes behavior in the synthetic data is similar to the behavior in the field data. From the experiments, it is shown that the dispersion, the scattering and the backscattering of surface waves is caused by the surface topography and irregular bedrock.

[3] Master Thesis

[4] Faculty of Physical-Mechanical Engineering. Electrical, Electronics and Telecommunications School. Advisor: PhD. Daniel Alfonso Sierra, Co-advisor: PhD. César Antonio Duarte Gualdrón

Introduction

Seismic signal processing is a fundamental research area to synthesize and analyze the information provided by seismic waves propagation. This information has enabled geophysicists to study the Earth's interior, which is composed by a variety of minerals and elements essential for the survival of humanity. Most natural resources used by humans are extracted from the first hundred meters under Earth's surface. Filtering the information acquired is a mandatory step in the seismic data processing, since it allows to highlight the information of interest by attenuating the energy considered as noise. The subsequent stages, namely deconvolution, stacking and migration, are highly dependent on the filtering stage, since the output in each of these processes would not be consistent with the subsurface structure if the input data contained considerable amounts of noise. The most common noise to be attenuated is the ground roll which is a type of coherent noise produced by surface waves. This noise corrupts the information contained in the reflected waves, which provides valuable information about the geometric arrangement of sub-surface's layers and its most likely lithologies. Unlike conventional seismic, in which only pressure waves are recorded in one component, multi-component seismic uses the information provided by these seismic waves recorded in several directions. This additional information has allowed the development of polarization filters with which it is intended to filter the ground roll present in the seismic data from the information provided by the vector movements of the waves present in the seismograms. Therefore, obtaining multicomponent synthetic earthquakes with a realistic ground roll will allow a characterization of the ground roll according to the subsoil models used in the simulation. In addition, by processing these synthetic data, it is possible to tune the polarization filters in order to improve the ground roll attenuation.

In this project, we implement a 2D finite difference elastic wave modeling with irregular near-surface to compute synthetic seismic data with realistic ground roll. The synthetic data are compared to real data by using seismic attributes analysis. The real data are three different 2D-3C data sets acquired in Colombia, which exhibit a markedly differentiated behavior within the surface-waves zone.

In Chapter 2, the ground roll concept is introduced, showing its importance and the methods available for its analysis. A revision about ground roll composition is mentioned, as well as an analysis of its principal features is described. Finally, an example of ground roll characterization, using seismic attributes, is performed on real multicomponent seismic data acquired in Colombia.

In Chapter 3, a methodology that uses pattern recognition to select the best seismic attributes that should be chosen to detect and classify surface waves in a seismic record, based on the notion of similarity, is presented. The methodology is applied on the automatic interpretation of three different seismic data record sets. The results obtained for these different real datasets exhibit markedly differentiated surface waves that improve and automatize the expert judgment interpretation.

In Chapter 4, a review about two-dimensional finite-difference modeling of elastic waves is presented. We have focused on all possible considerations that should be taken into account to model elastic wave propagation in complex media. Surface topography is contemplated in the earth models aiming to produce realistic seismic data. For this, the improved vacuum formulation is implemented, which requires a number of points per wavelength higher than conventional modeling to ensure accurate Rayleigh wave. Numerical results are contrasted with analytic solutions in order to quantify and compare the performance of the algorithm proposed.

In Chapter 5, the results of different synthetic experiments of surface waves propagation through earth models with irregular near-surface are presented. In each experiment, seismic data are acquired and later seismic attributes are computed from the seismograms. From our simulation results, it is shown that the moveout of surface waves is strongly affected by the surface topography, the soil-column and the irregular bedrock. Similarly, The Rayleigh wave dispersion is highly related to the thickness of the soil-column layer and surface waves scattering is strongly depending on thickness variations of the soil-column. Seismic attributes from the synthetic data are computed in order to enhance the surface wave properties. Therefore, the higher modes, scattering and backscattering of surface waves were identified by means of seismic attributes.

In Chapter 6, a comparison of the behavior of the seismic attributes of the surface waves between synthetic and real seismic data is presented. The synthetic acquisition was performed by finite differences modeling of the elastic wave propagation through the earth's models presented in the Chapter 5. The real data correspond to three different acquisition in Colombian surveys. Different surface waves behavior is noted in each type of data and the seismic attributes show the similitudes and differences between real and synthetic seismic data.

Finally, in Chapter 7, the conclusions and future work of the project are presented.

Chapter 1

Ground roll characterization in real seismic data

Abstract

Surface waves analysis is very useful in near-surface characterization. Information extracted from seismic signals of surfaces waves allows to construct an image of the Earth's surface. However, despite the information in the surface waves, in exploration seismology that information is removed because it is considered as a noise, called *ground roll*, which masks information of interest from reflection waves. From a revision of the literature, we found ground roll is a concept that involves different kind of waves, resulting in different features in the seismic signal. We perform an example of ground roll analysis using seismic attributes extracted from real seismic data acquired in Colombia. The analysis shows the ground roll complexity inasmuch as features change with time and space.

1.1 Introduction

The Earth's subsurface is mainly characterized using the information provided by seismic waves. According to [Yilmaz, 2015], Earth's interior can be divided in three categories of study. Earthquake seismology allows to investigate the deeper earth interior from the analysis of seismic waves (usually less than 10 Hz) produced by earthquakes, allowing the study of depths down to 100 km or more. Exploration seismology is used for exploration and development of oil and gas fields. Seismic waves (usually less than 100 Hz) produced by artificial sources allow to study a depth of interest down to 10 km. Engineering seismology

is applied to study near-surface geology. Here, seismic waves (usually less than 1000 Hz) allow to image depths of interest down to 1 km.

Seismic waves can be separated into two groups. Body waves correspond to the energy from seismic sources that travel into the Earth's interior. In contrast, surface waves travel along or near the surface of the ground. The latter ones are commonly known as ground roll in exploration seismology and their attenuation is a problem in seismic data processing since they tend to mask desired reflection signals. Ground roll differs from body waves in frequency content, polarization and velocity. Internal waves exhibit linear polarization, higher frequency content and lower amplitudes compared to surface waves.

Ground roll interferes with body waves and is considered the most harmful noise generated by seismic acquisition sources, thus the attenuation of ground roll has been of great interest since the beginning of seismic acquisition. A great number of methods have been proposed for this purpose; among the most popular are: $f-k$ filters, band-pass filters, and stacking [Yilmaz, 2001]. However, these methods have some practical limitations because ground roll in most cases is consistent (coherent) with the information of body waves and sometimes has a similar frequency band, as in the case for some P-S converted waves. With the emergence of multicomponent seismic, the idea of using polarizing filters emerged, based on the assumption that the motion of particles for body waves tends to be linear, whereas in surface waves, it tends to be elliptical.

In this chapter, the ground roll concept is introduced, showing its importance and what methods are available to analyze it. A revision about ground roll composition is mentioned, as well as an analysis of its principal features is described. Finally, an example of ground roll characterization via seismic attributes analysis is done on real multicomponent seismic data acquired in Colombia.

1.2 Ground roll composition

Ground roll is a broad concept that comprises energy of a rich variety of wave types that propagate close to the earth surface. In seismic records, ground roll is delineated by a kind of conical form that masks the information of interest [Sheriff, 2002]. Among this mixture of waves, Rayleigh waves are significant. They are a type of surface wave characterized by elliptical polarization, slow speed, low frequency, and high amplitude that result from the interaction between P and SV waves in areas close to the surface. The innermost energy component in the "ground roll cone" comes generally from the interference of scattered waves, refraction, and reverberations. The scattering of surface and body waves is caused by inhomogeneities in shallow layers (near-surface), which is physically equivalent to the

radiation field of elastic excitation sources located at scattering points [Almuhaidib and Toksöz, 2014]. More information about the waves that make up the ground roll are shown below.

1.2.1 Rayleigh waves

Rayleigh waves are the principal kind of wave composing ground roll. These waves are produced by interaction between compressional and shear waves in the surface. When a compressional wave energy incidents at an interface, it is partitioned into four components (Figure 1.1a): reflected compressional wave, reflected shear wave of SV-type, transmitted compressional wave, and transmitted shear wave of SV-type [Yilmaz, 2015]. If the compressional wave energy incidents at the soil-bedrock interface, then the P-to-P reflected and P-to-SV mode-converted wave energy that exceed the critical angle are trapped within the soil column and travel along the surface and the particles move in retrograde sense around an ellipse that has its major axis vertical and minor axis in the direction of wave propagation (Figure 1.1b) [Lowrie, 2007].

Figure 1.1 a) Compressional wave energy partitioned into four components b) Rayleigh wave propagation with coupled P-SV-type particle motion.

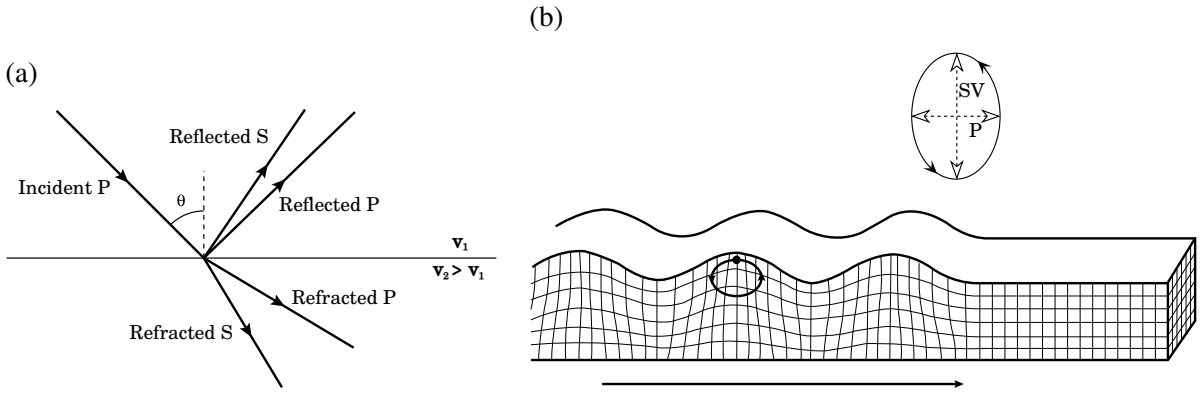

1.2.2 Higher Modes

In real seismic acquisitions, the media is not homogeneous and ground roll may involve other higher modes than a pure Rayleigh. From a physical point of view, the existence of different modes of propagation at a given frequency is due to constructive interference occurring among waves. This interference is called *geometric dispersion*, a phenomenon by which the velocity of surface waves is a multi-valued function of the frequency of excitation

and it is responsible for the existence of several modes of propagation each traveling at a different phase and group modal velocity. The phenomenon of geometric dispersion is caused by the effects of constructive interference occurring in media that are either bounded or inhomogeneous [Foti et al., 2014].

In general, there are several modes of propagation at a given frequency, with the higher modes characterized by a higher speed of propagation. Also, as the frequency increases, the number of modes associated with that frequency increases as well and the modes appear more closely spaced. Figures 1.2a and 1.2b show a real seismic data-set and its $f-k$ spectra respectively. It is possible to observe ground roll dispersion inasmuch as three different modes travel at different frequencies and different wavenumbers. A common feature of multi-mode Rayleigh wave propagation is that higher modes have a greater penetration depth than lower modes.

Figure 1.2 a) Real seismic data. b) Seismic data in the wavenumber-frequency domain. Three different propagation modes of Rayleigh waves were identified, each one of them traveling at a different wavenumber and frequency.

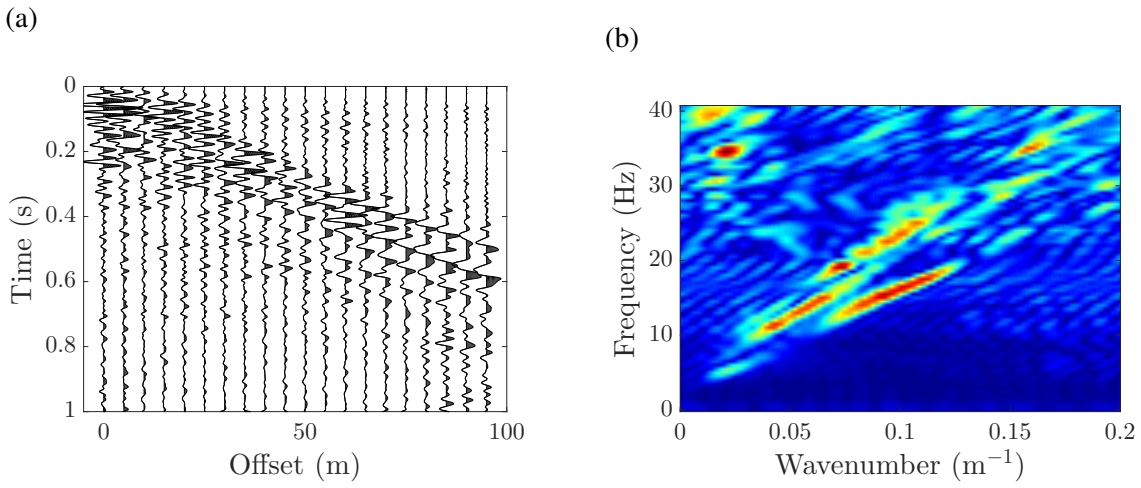

1.2.3 Scattering

Scattering is the energy that is forced to deviate from a straight trajectory by one or more paths due to near-surface heterogeneities According to [Levander, 1990], depending on the type of heterogeneity present, the scattering can include body wave scattering, surface wave scattering, body-to-surface, and surface-to-body wave scattering. Figure 1.3 shows how seismic wave scattering is produced. Some information about these kind of scattered waves will be presented shortly.

- **Body wave scattering** includes reverberations in a smooth surface layer, and body-to-body wave scattering from heterogeneities Reverberations are the multiple reflection presented in the upper layer (soil-column), that means seismic energy has been reflected more than once between the base of a surface layer, which is generally a low velocity zone, and the free surface. Body-to-body wave scattering was simulated by [Almuhaidib and Toksöz, 2014] who shows the effects of near-surface heterogeneities in scattering seismic waves. Figure 1.3a shows how a body wave is scattered in body waves.

- **Surface wave scattering** is the surface wave energy that is deviated from the scatterer as surface wave. It is produced by surface waves interaction with irregular topographies or near-surface heterogeneities, specially scattering of Rayleigh waves in the free surface is strongly wavelength dependent compared to size of scatterers and topography. The perturbation analysis performed by [Hudson and Knopoff, 1967] shows that backscattering energy is higher than forward scattering. Figure 1.3b shows how surface wave is scattered to surface waves.

- **Body-to-surface** wave scattering is the energy of the incident compressional wave that is converted to a surface wave in the scatterer location. There are two causes by which these scattered waves are generated. First, when near-surface heterogeneities are present, seismic energy of body waves is scattered and converted to surface waves. The scattered seismic energy depends strongly on the properties of the scatterers (impedance contrast, size relative to the incident wavelength, depth, attenuation factor of the medium) [Almuhaidib and Toksöz, 2014]. Second, when an incident body wave strikes an irregular free surface or an irregular surface layer, some incident wave energy is converted as surface waves. When the height and slope of the irregularity is small compared to the wavelength of the incident wave, the stresses caused by the topography behave like a new source applied to a smooth surface [Gilbert and Knopoff, 1960] [Hudson and Knopoff, 1967].

- **Surface-to-body** wave scattering is the energy of surface wave that is converted as body wave from the scattering locale. Surface wave propagation in a irregular free surface or an irregular wave guide can produce scattered body waves. Actually, no matter the incidence direction of a Rayleigh wave at the surface, converted body waves is about 80% of the incident wave [Martel et al., 1977].

Figure 1.3 Generation of seismic wave scattering. An incident seismic wave is scattered by near-surface heterogeneities and irregular free-surface. a) Body-to-body wave scattering. b) Surface-to-surface wave scattering. c) Body-to-surface wave scattering. d) Surface-to-body wave scattering.

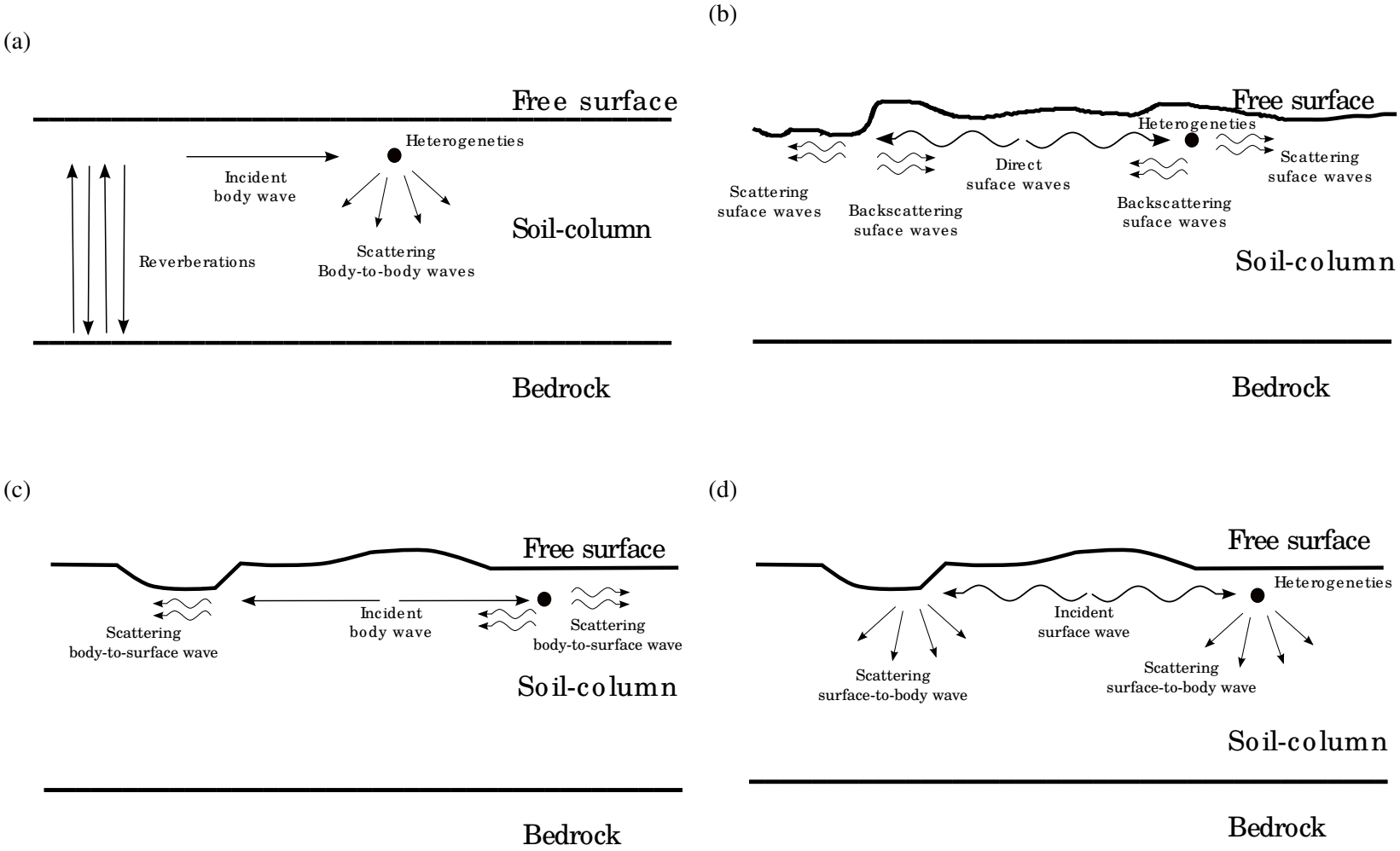

1.3 Ground roll features

We have shown that ground roll is composed by different kind of waves. This implies that ground roll has different features which should be studied if want to reproduce them by elastic wave modeling. According to [Foti et al., 2014], the complexity of the surface waves depends on the the velocity variations within the soil-column because dispersion and multiple modes are generated by the presence of these variations. Some of the main ground roll features are mentioned below, as well as they are affected by variations with-in the soil-column.

1.3.1 Amplitude and Attenuation

In exploration seismic records, surface waves have amplitudes higher than body waves. Therefore, surface waves energy tends to mask desired reflection signals, reason by which its attenuation it is a common problem in seismic signal processing.

It has been found that the amplitudes of Rayleigh waves are greatly influenced by the geometry of lateral heterogeneities within the soil column [Yilmaz, 2015]. From the model and field experiments, [Yilmaz, 2015] shows that, in general, the amplitudes of the waves that travel along a free-surface boundary or an interface between two layers indeed, decay rapidly in depth.. Moreover, surface wave amplitudes are higher when the source is closer to the free surface.

Surface waves attenuates rapidly with depth. In a uniform half-space, the amplitude of the particle displacement decreases exponentially with increasing depth [Lowrie, 2007]. On the other hand, surface waves attenuate less rapidly with distance along the direction of propagation because they have a quasi-cylindrical wave-front, compared to body waves that have a quasi-spherical wave-front. Therefore, surface waves amplitude declines proportional to $1/\sqrt{r}$ (the inverse of the square root of the distance from the source), unlike body waves which their geometrical spreading factor is proportional to $1/r$ (the inverse of the distance from the source). This is valid only in homogeneous media, because in stratified media this attenuation law does not hold since surface waves are composed by several modes of Rayleigh waves [Foti et al., 2014]. As it is shown in section 1.2.2, several modes of the Rayleigh wave are produced by constructive interference among waves undergoing multiple reflections and refractions at the layer interfaces.

Wave attenuation means that part of the energy of the waves is consumed when the wave pass through a medium. The most important cause by which seismic waves are attenuated is the presence of fluids in pores, which acts as a low-pass filter affecting strongly high-frequency wave motion. Similarly, compressional waves are more influenced by pore fluids

than shear waves. Hence, Rayleigh waves suffer a frequency-dependent attenuation because they are a coupling of P-waves with SV-waves [Zhang et al., 2014].

1.3.2 Velocity

Rayleigh wave velocity is said to be slower than body wave velocity. From shot gathers it is possible to observe that arrived times of the Rayleigh waves are greater than arrived times of the body waves. The line that describe arrival times of seismic waves is known as moveout. It is an important aspect constructing a seismic image because it has information about propagation velocity of seismic waves through subsurface media. Figure 1.4 shows the arrival times for three different seismic waves, the slope for each line indicate that Rayleigh wave velocities is smaller than P-reflection and P-refraction wave velocities. Model experiments and appropriate field data analysis performed by [Yilmaz, 2015] show that moveout of surface waves is influenced by topography and soil-column geometry. When the near-surface is vertically inhomogeneous, several modes of Rayleigh waves are produced thus surface waves propagates at a speed that is called apparent phase velocity [Tokimatsu, 1995] [Lai and Rix, 1998]. This speed varies depending on spatial position where it is measured [Foti et al., 2014].

Figure 1.4 Vertical shot gather. Color lines show different velocities for each seismic wave.

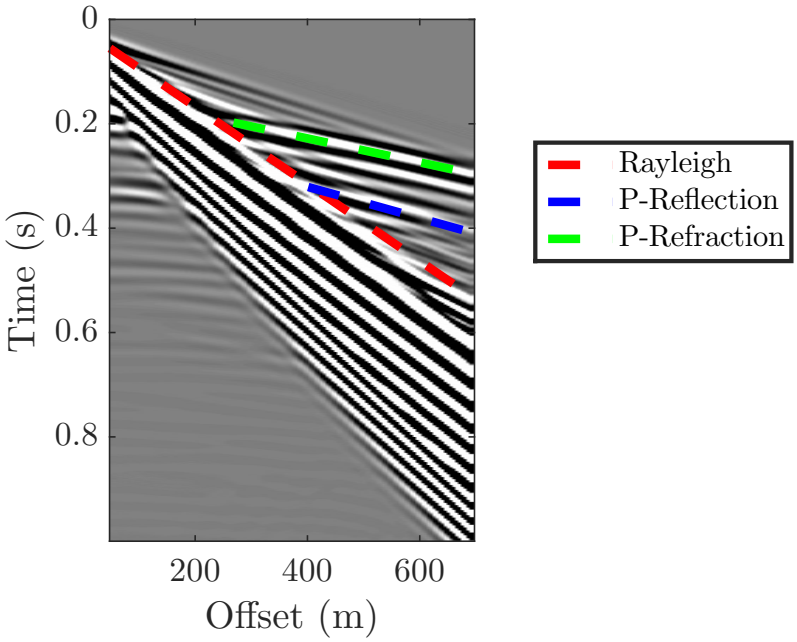

1.3.3 Polarization

Polarization is related to particle movements when a seismic wave is traveling. Compressional waves induce particles to move in the same direction of wave propagation. Thus compressional wave is said to have linear polarization. Meanwhile, Rayleigh waves propagate with elliptic-retrograde particle motion.

Diverse polarization filters for ground roll attenuation have been proposed based on the elliptical behavior of those surface waves. Some of the classical methods are the polarization analysis proposed by [Filnn, 1965], [Samson and Olson, 1981], [Vidale, 1986], [Bobbit, 1984], [Jurkevics, 1988], [Shieh and Herrmann, 1990], [Perelberg and Hornbostel, 1994], [Kragh and Peardon, 1995] among others. These methods focus on the analysis of the covariance matrix of multicomponent data. Methods based on eigen-image analysis were worked by [Liu, 1999], [Chiu et al., 2007], [Chiu et al., 2008]. The method based on singular value decomposition (SVD) was proposed by [M. et al., 1991], suggesting SVD as a technique for analyzing polarization in multicomponent seismic signals. Subsequent work used SVD for designing polarization filters. Some of the work in this area are: [De Franco, 2001], [Mars et al., 2004], [de Meersman and Kendall, 2005], [Jin and Ronen, 2005], [Kendall et al., 2005], [De Meersman et al., 2006], [Donno et al., 2006], [De Meersman, 2008], [Tiapkina et al., 2012].

These polarization-filtering methods assume a surface wave propagation of elliptical-planar type and are valid only for pure Rayleigh waves and reflections or conversions in planar reflectors. However, the actual characteristics of ground roll are not often restricted to planar cases. For instance, when there is scattering, some impinging energy does not have a preferential plane, leading to incident energy on different planes. Figure 1.5 shows that because of heterogeneities in a shallow layer, some scattering points can be involved to cause ground roll to be incident from different directions. It can also be noticed that because of the complexity of interfaces, the direction of arrival of reflection waves is different for each reflection point.

1.3.4 Dispersion

A wave is dispersive if each frequency component travels at a different speed. In that sense, surface waves are dispersive. According to [Yilmaz, 2015] it is possible to identify three causes by which surface waves become more dispersive. First, The high velocity contrast between a low velocity soil column and a high velocity bedrock. When a high velocity soil column is present, surface waves are weakly dispersive. Second, the thinner soil column, the increase dispersive character of surface waves. The experiments performed by [Yilmaz, 2015]

Figure 1.5 Comparison of Rayleigh waves, scattered waves and body waves. Notice the elliptical or linear behavior for each type of wave and the possibility that energy may arrive from out of the vertical-radial plane because of reflections/conversions from off-line dispersion points. The grey ellipse represents a scattering point.

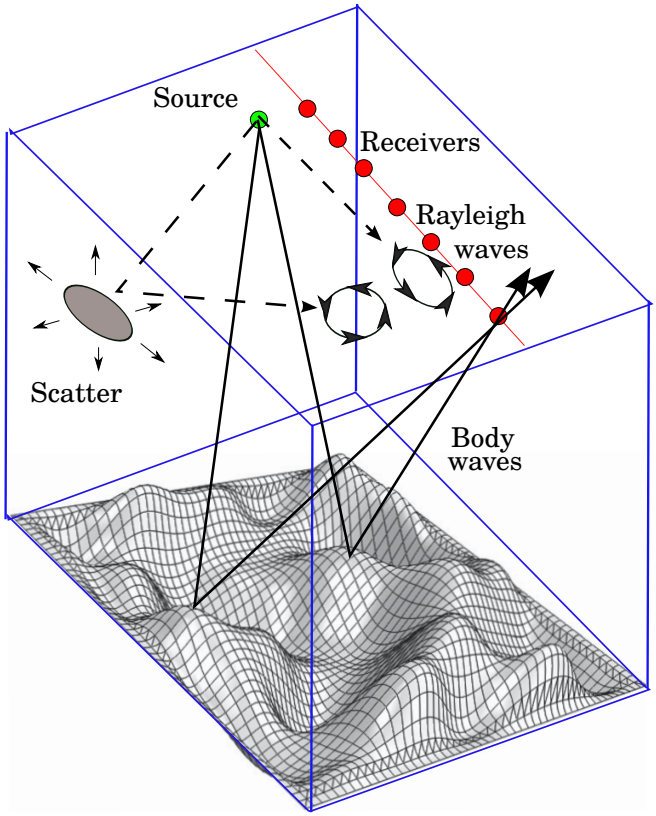

show that the same amount of energy is associated with the seismic source trapped within the soil column no matters the thin of the soil column. Thus, the dispersion phenomenon intensifies because the same amount of energy is trapped to a smaller volume. Third, vertical velocity variations in the soil column results in dispersive Rayleigh waves. If the soil column is formed by thin layers, the dispersive character of Rayleigh waves becomes more prominent.

The dispersive character of surface waves can be analyzed by dispersion curves. these curves are constructed computing the 2-D Fourier transform from a shot gather of seismic data. Thus, to decompose a wavefield into its plane-wave components, each with a unique frequency and each traveling at a unique angle from the vertical direction. Figure 1.6 shows the dispersion curve from a real seismic data set. It is possible to see the dispersive character of surfaces waves inasmuch as three different modes travel with different velocities at different frequencies.

Figure 1.6 a) Real seismic data. b) $f-v$ transform of the data. Three different propagation modes of Rayleigh waves are identified, each one of them travels with different velocity and frequency.

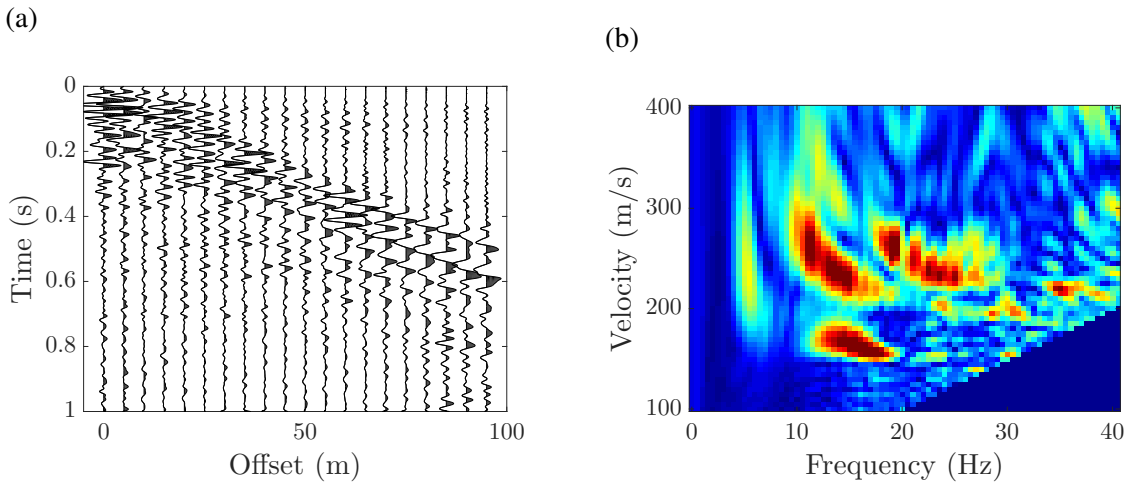

1.4 Surface waves behavior: Example with real data

To record surface-wave data, you need geophones sensitive to particle motion with different components. Consider a Rayleigh wave which travels horizontally in the x-direction along the free surface. To record the Rayleigh-wave particle motion which is in the z-direction, you need to use a vertical-component (z-component) geophone. Consider a Love wave which travels horizontally in the x-direction along the free surface. To record the Love-wave particle motion which is in the y-direction, you need to use a horizontally transverse-component (y-component) geophone [Yilmaz, 2015].

The previous results lead us to propose that one of the reasons why polarizing filters are seldom successful on real data is because investigators assume ground roll has a planar behavior. Attributes such as ellipticity and planarity show us that the ground roll cone exhibits areas with very different behavior. Taking for example the seismic records belonging to the real data, five different zones can be distinguished that have different planarity and ellipticity values (Figure 1.7). Table 1.1 summarizes the qualitative observations made for each of these five zones according to its ellipticity, planarity and amplitude.

Curve A-R is a linear event with S wave velocity ranging from 460 to 740 m/s that has higher energy in the horizontal components of the seismic data. Zone 1 spans between this linear event (AR curve) and the boundary line marked BO. Zone 2 has low-frequency and large-amplitude events in the vertical components. This area ranges from the BO curve to CO curve. Zone 3 extends from the CO line to the DO line and may correspond to higher modes

Table 1.1 Qualitative comparison of the behavior presented in each of the five zones identified with differences in ellipticity, planarity and amplitude.

Zone	**Ellipticity**	**Planarity**	**Amplitude**
1	Low	Medium	Low
2	Medium	Very high	High in radial component.
3	High	Low	High
4 (Rayleigh wave)	Very high	High	High
5	Medium	low	High

of Rayleigh wave. Zone 4 corresponds to the fundamental mode of the Rayleigh wave and it is bounded by the DO and EO lines. This area shows that the fundamental mode has higher values of ellipticity and planarity than do the higher modes. Finally, zone 5 corresponds to the innermost part of the cone limited by the Rayleigh wave (line OE). This area contains reverberations or scatter of the surface energy, which indicates that parameter is impinging from variable directions, and therefore events are not planar.

As was shown in Figure 1.5, due to heterogeneities in the shallow layer, ground roll is commonly not only composed of pure Rayleigh waves but also contains scattered surface waves. This causes the ground roll to propagate in more than one preferential plane, and each polarization plane depends on the angle of arrival of each of these scattering waves. The scattering dominated zone is a region for which a conventional polarization filter (working in only one plane) would have difficulty attenuating ground roll energy (outside of that plane).

Figure 1.7 Zones identified in the medium-frequency real data. a) Vertical-component from the original dataset. b) Radial-component data from the original dataset. c) Computed ellipticity attribute. d) Planarity attribute. Line A-R is a possible S-wave refraction. Zone D-O-E is the fundamental Rayleigh wave. The color bar is dimensionless.

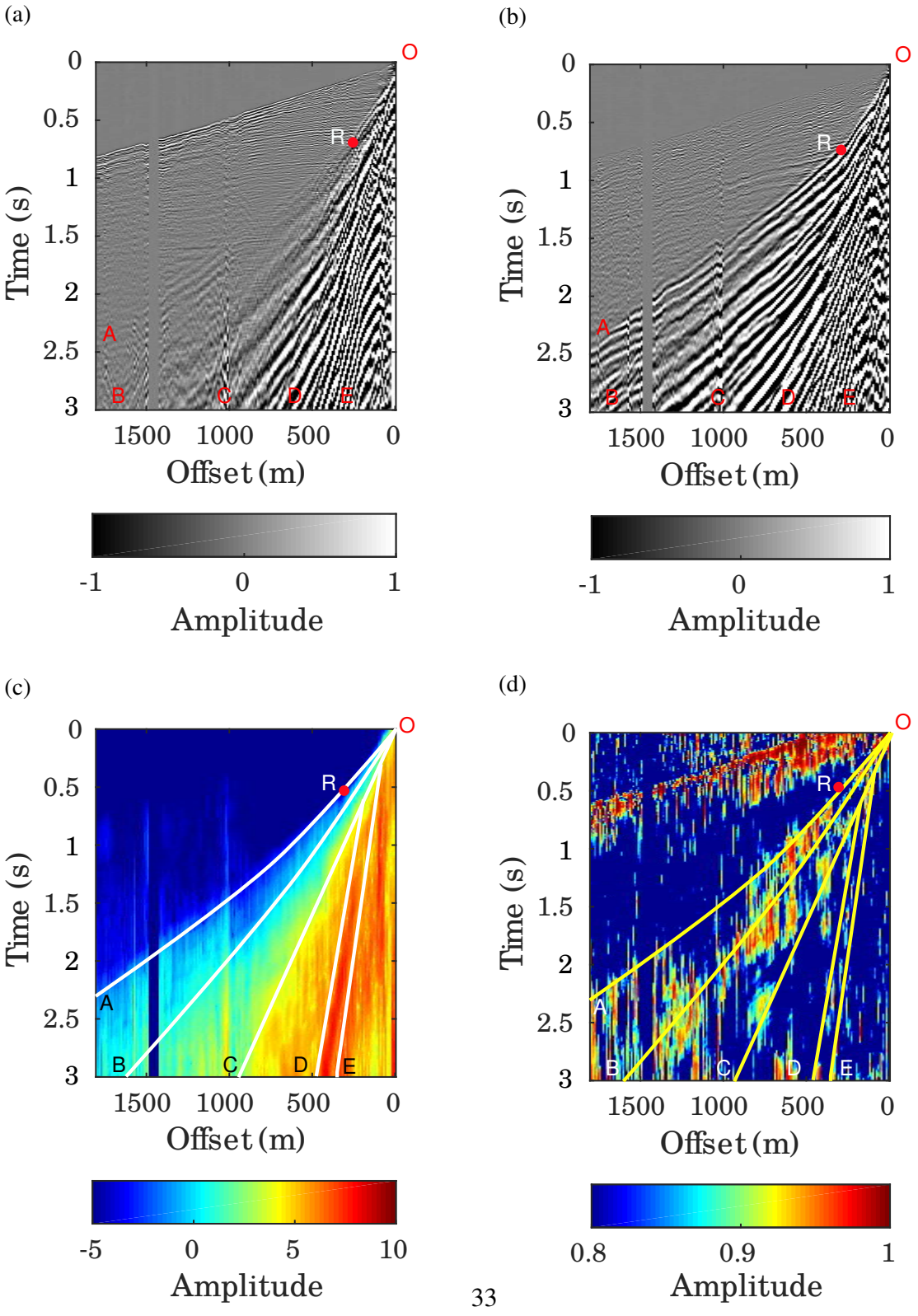

Chapter 2

Seismic attributes selection and clustering to detect and classify surface waves in multicomponent seismic data by using k-means algorithm

Abstract

Seismic records are characterized by a high level of complexity resulting from the interaction of different types of waves propagating in the subsurface. Interpretation of the different wave modes and features present in a seismic record is generally done by expert judgement, and its automatization is a problem that has not been completely solved. We present a methodology that uses pattern recognition to select the best seismic attributes that should be chosen to detect and classify surface waves in a seismic record, based on the notion of similarity, and that is applied on the automatic interpretation of three different seismic data record sets. The results obtained for these different real datasets exhibits markedly differentiated surface waves that improves and automatize the expert judgement interpretation

2.1 Introduction

In the last decades, dozens of different seismic attributes have been proposed to detect, characterize and finally filter surface waves (a partial list is presented in Table 2.1). It is difficult to decide which of these parameters apply better for a particular case or even if they are independent. Pattern recognition provides a data-driven way to classify which

of these attributes contribute the most to detect surface waves on a specific case. Surface wave detection could be considered the first stage before its separation, which is possible by locally filtering through attributes that differentiate surface waves from other wave modes. When detection is not properly done, essential information about wave modes of interest (e.g. reflections) can be lost, since filtering will remove indiscriminately different wave modes. The proper usage of filters reduces the possible damage to the signal since they operate within the record intervals where the surface waves are detected.

Fundamentally, surface waves differ from body waves in frequency content, polarization, its dispersive character and propagation velocity. However, in real cases, surface waves can exhibit a very complex behavior: (1) because of heterogeneities in the shallow layer, some scattering points can be involved causing surface waves to be incident from different directions. (2) surface waves involve other modes than a pure Rayleigh wave produced when the medium is not homogeneous [Sheriff, 2002]. Therefore, surface waves classification is generally done by expert judgement, and its automatization is a problem that has not been completely solved. A careful exam of a seismic record show that there are different regions inside a surface waves cone, each with its own seismic attributes characteristics.

Figure 2.1a displays a real 3-C seismic exploration record, where the Vertical, Radial and Transverse components are given from left to right. There, the surface waves cone is interpreted (by human judgement) as the area under the dashed yellow curve. To illustrate the seismic attributes differences between both surface and body waves, one seismic trace is extracted to compute the spectra and the hodogram of the data within a time sliding window. When this sliding window travels along the body waves zone, the frequency content ranges from 30 to 50 [Hz] and the polarization tends to be linear, as shown in the Normalized Spectra and Hodogram of Figure 2.1b. In contrast, when the sliding window cross the surface waves area, in Figure 2.1c, the frequency content is much lower, ranging from 5 to 15 [Hz] and polarization tends to be elliptical. These basic attribute differences can be used to separate surface waves from reflection waves. Hence, a primary classification by frequency content and polarization is evident. However, real cases show that this simple classification (based on frequency filtering or simple polarization attributes) is not adequate for complex surface waves. Using a more complete set of seismic attributes makes possible to quantify the behavior of the wavefield propagation from seismic data. That raises the question: That raises the question: Which and how many attributes we need to consider obtaining an accurate classification for seismic waves?

This work was motivated by the results obtained in [Sánchez et al., 2016], in which the goal was ground roll attenuation by polarization filtering. At that work two attributes (ellipticity and planarity) were computed and a detection and classification of surface waves

Figure 2.1 a) Vertical, Radial and Transverse components of the 3-C seismic show gather. Comparison between (b) body waves and (c) surface waves behavior by means of the Normalized Spectra and Hodograms obtained for each sliding time window.

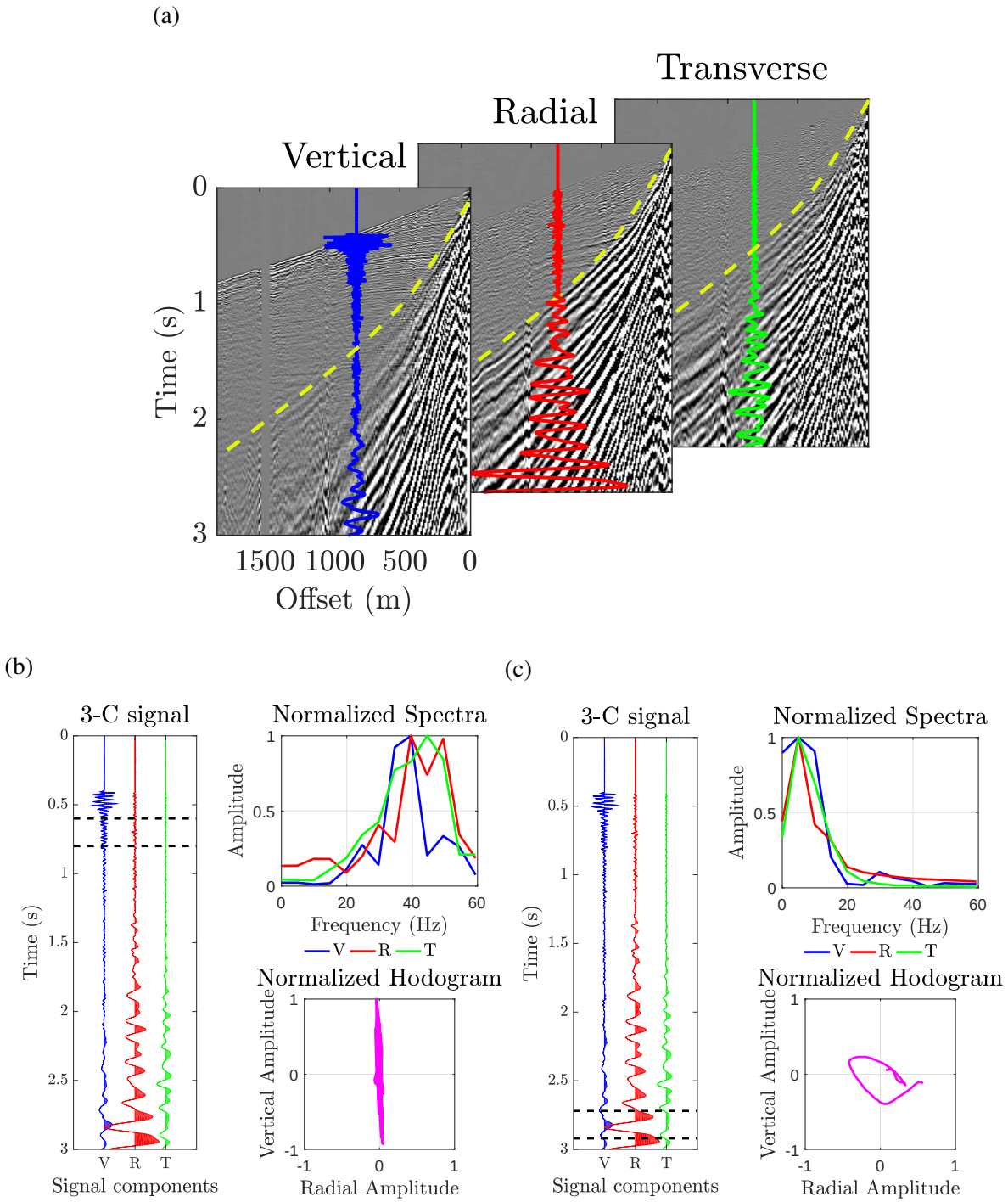

was done interpretatively by human judgment. The aim of this work is to show that is it possible to perform this detection and classification automatically using pattern recognition techniques which allow to separate the information with different behavior and with the use of an arbitrary number of attributes.

Pattern recognition tools allow to minimize errors in classification process. These have been used for seismic events detection, signal classification and data visualization. There are two ways for developing them. Supervised learning is mainly used when labelled data, based on expert knowledge, is available. This approach has been used in seismology to discriminate different events and to automatically detect seismic phases [Joswig, 1990], [Bai and Kennett, 2000], [Ohrnberger, 2001], [Riggelsen et al., 2007]. On the other hand, unsupervised learning allows to cluster input data in classes based on their statistical properties, by giving a probabilistic model of the data when the machine is not given supervision or reward; allowing data speaking by itself. On this approach, Self-Organizing Maps have been used for the discovery, imaging and interpretation of temporal patterns in seismic array recordings [Köhler et al., 2008], [Köhler et al., 2010].

This work takes advantage of the discrimination capacity of the seismic attributes to discern the different behavior attributes of the wave propagation and, based on these differences, build a robust attribute model that allows to detect and classify the surface waves. Then, the practical expectations of this method are two-fold: (1) to detect the surface waves zones by separating them from the rest of the information and (2) to classify these surface waves into subgroups, according to analogous behavior within the surface waves cone zone.

To assess the performance of this surface waves detection and classification methodology, we apply it to three different real 2D-3C data sets acquired in Colombia and that exhibits a markedly differentiated behavior within the surface waves zone. Pattern recognition was performed using the unsupervised clustering technique k-means.

2.2 *k*-means clustering algorithm

k-means is the most popular clustering algorithm employed to partition a dataset of n points into k groups so that each of the n observations belong to the cluster with the nearest mean. Its advantage is that is used when no a priori knowledge such as expert classification of the data, is assumed to be available. This is why is called an unsupervised learning technique. In this method, any information is given about where each of the data points should be placed within the partition, they are clustered according to some notion of similarity presented in the set of attributes provided to the algorithm.

The algorithm starts with the assumption that the number of clusters k for the database, shown in Figure 2.2a, is known. When this is not true, it is possible to use a wrapper search to find the best value of k; however, other approaches have been proposed in literature to find the optimal number of clusters [Honarkhah and Caers, 2010]. Then, k initial cluster points, known as seeds, are randomly chosen within the space of attributes to be the centroids of the clusters, as shown in Figure 2.2b. Then, each data point is grouped to the nearest centroid. After assigning all the points to their corresponding nearest centroids, the first iteration of clusters of Figure 2.2c is obtained.

In each iteration, the mean of each of the k clusters is recomputed and hence the centroids are relocated, Figure 2.2d, changing the distribution of the data points within each cluster, as shown in Figure 2.2e. This procedure is done iteratively, as illustrated from Figures 2.2f to 2.2g, until no changes in the objective function are evident. The objective function comes down to minimize the sum of distance functions of each point in the cluster to its centroid, given in the optimization problem in equation 2.1. In summary, the search of these centroids aims to minimize the within-distances while maximizing the between-cluster distances.

$$J = \sum_{j=1}^{k} \sum_{i=1}^{n} \| \boldsymbol{x}_i - \boldsymbol{c}_j \| \tag{2.1}$$

Where J is the objective function to be minimized, $\boldsymbol{x}_i^j$ is an attribute vector corresponding to the ith observation in the of the jth cluster and $\boldsymbol{c}_j$ is the location of the centroid of the jth cluster in the attribute space.

As a final remark, it is important to say that despite this algorithm is efficient, easy to understand and to implement, if the objective function J is used, it can converge to a local optimum since the global optimum is hard to find due to its complexity.

2.3 Method: surface waves detection and classification

Seismic attributes are quantities extracted from seismic data to provide additional information to enhance the geophysical understanding of the data. Thanks to its elliptical and low frequency motion, surface waves attributes are focused on frequency content and polarization analysis, hence multicomponent seismic data should be available. The flowchart in the Figure 2.3 shows step by step how the method was carried out. The process in each step will be briefly explained.

Attribute Generation: seismic attributes were computed using 6 different polarization analysis methods from short-time windows of three-component seismic data. Table 2.1 shows the seismic attributes computed for each trace.

Figure 2.2 Clustering by *k*-means. In this example three classes are determined. (a) Set of data-points (b) The *k* seeds are randomly chosen within the space vector and (c) each data point is matched to the closest centroid. (d) The means are re-computed and the centroids re-located and (e) the distribution of the data points within each cluster is changed. (f) This process is repeated until no changes in the objective function are evident and (g) the final classification is obtained.

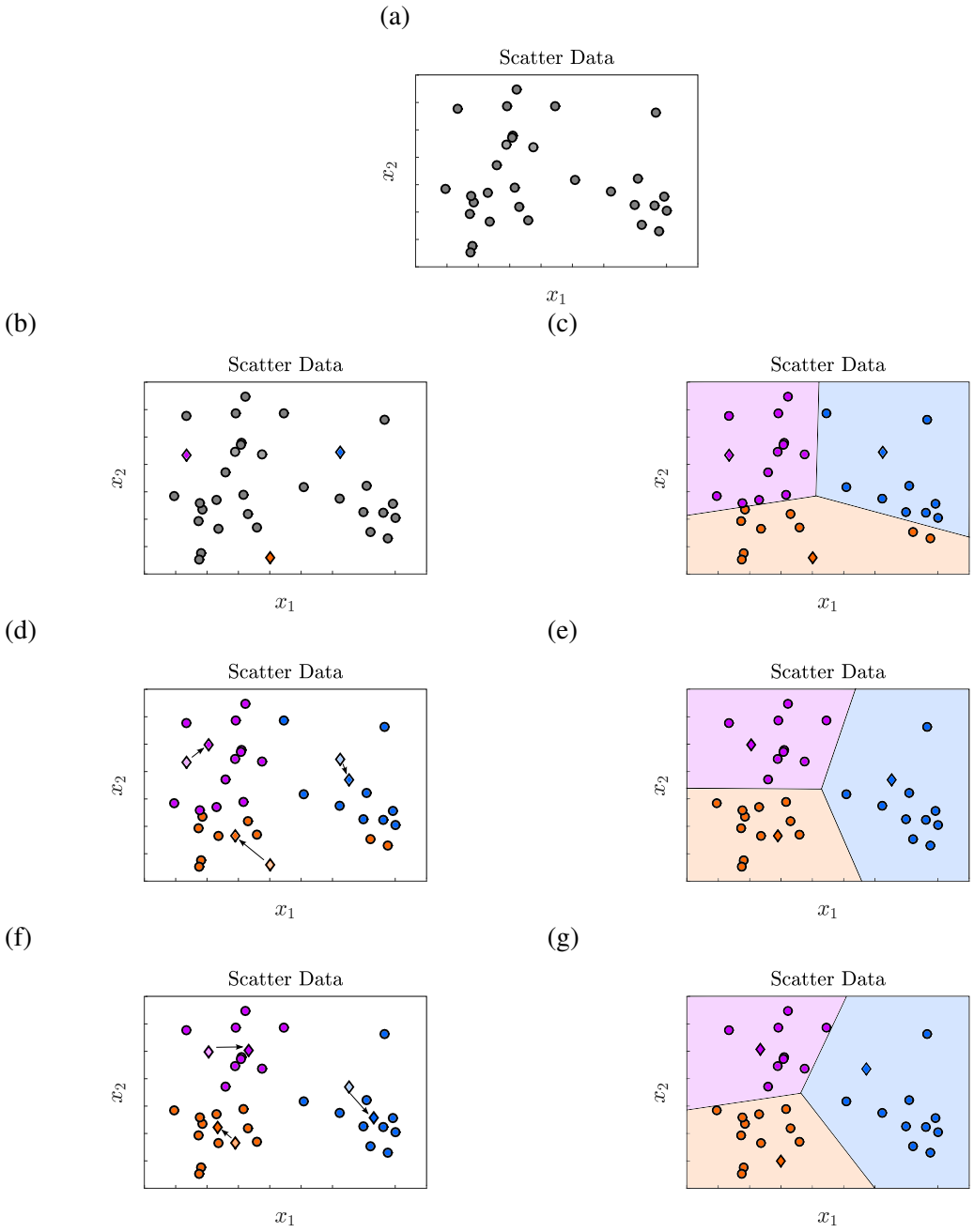

Figure 2.3 The flowchart shows the step by step of the work carried out along this research.

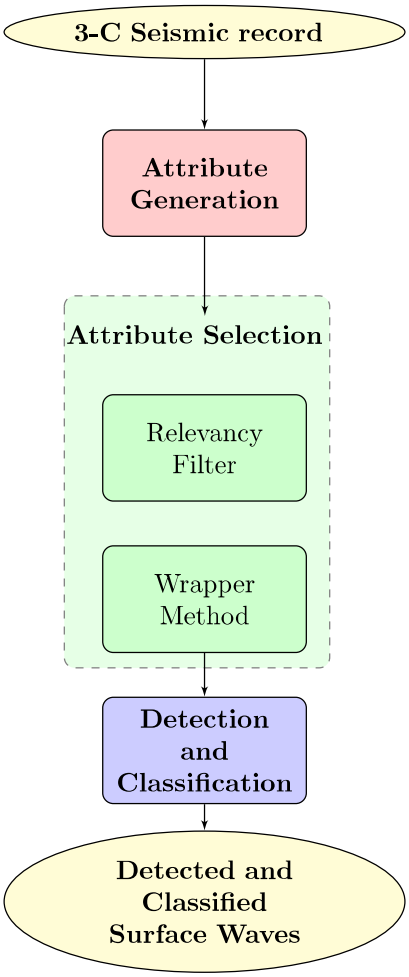

Attribute Selection the objective of this step is three-fold: improving the prediction performance, providing faster and more cost-effective predictors as well as providing a better understanding of the underlying process by reducing the complexity of the model. A relevancy filter comparing the correlation between features was used. Features were sorted in ascending order and those whose correlation was greater than 0.9 were removed from the dataset (see Figure 2.5a). A wrapper forward method was the second feature selection algorithm. This method considers the selection as a search problem where different combinations of seismic attributes are evaluated and compared based on its cost function. The cost function set in this work was the accuracy of classification and, the predictive model used to evaluate this cost function, given a number of seismic attributes, was *k*-means. The search process starts by identifying the couple of features giving the highest accuracy classification and each new feature is added iteratively only if this enhances the accuracy given by the previous group. In short, this works as a recursive feature addition algorithm.

Classification: this step is comprised of two stages: (1) surface waves detection and (2) surface waves classification. In the former one, observations are clustered into two groups: surface waves and body waves, from the features selected in the last step; this clustering is performed using the unsupervised pattern recognition technique *k*-means. In the latter one, observations belonging to the surface waves cluster are classified into two and three clusters in order to identify and separate areas with different behavior.

2.4 Results

The detection and classification of surface waves were performed in three types of real data, each one showing a markedly differentiated behavior within the surface waves zone. The first dataset corresponds to a 2D-3C acquisition using a relative low frequency source (close to the frequencies commonly used for oil prospecting). The second and third datasets are from a 2D-3C acquisition using a relatively high-frequency source. Table 2.2 shows the acquisition parameters for each dataset.

2.4.1 Field data example 1

The Figure 2.4 shows the Vertical, Radial and Transverse components from the field data 1. The attribute selection was performed following the methodology presented in the last section. The relevancy filter allowed reducing the number of attributes from the initials 45 to 35 based on their correlation matrix (Figure 2.5a). Meanwhile, a wrapping, using k-means and human-labeled data, allowed to reduce the number of significant attributes to 12, based on Accuracy of Classification as the cost function (Figure 2.5b). The list of significant attributes is shown in Table 2.3.

Figure 2.6a shows the areas manually labeled from the seismic record shown in Figure 2.4. Dispersion data of this label areas are shown in Figure 2.6b. Surface waves detection was done using *k*-means with $k = 2$. Figure 2.6c and Figure 2.6d show the result of the detection with its corresponding dispersion data.

2.4.2 Field data example 2

The shot gathers of the second type of data are shown in Figure 2.8. In this dataset, a more homogeneous behavior within the surface waves zone is evident. After following the flowchart given in Figure 2.3, the correlation matrix illustrated in Figure 2.9a is obtained and, as a result, 9 attributes were removed. The accuracy of the surface waves detection as a function of the number of the remaining 36 attributes, is shown in Figure 2.9b. From this

Table 2.1 Seismic attributes computed using different feature extraction methods in seismic data. V: Vertical Component, R: Radial Component and T: Transverse Component.

Attribute Extraction Method	No.	Seismic Attributes
Instantaneous Complex Trace [Morozov and Smithson, 1996]	1-3	Instantaneous Amplitude (V, R, T).
	4-6	Instantaneous Phase (V, R, T).
	7-9	Instantaneous Frequency (V, R, T).
	10-12	Instantaneous Reciprocal Ellipticity (V-R, V-T,R-T).
	13-15	Instantaneous Signed Reciprocal Ellipticity (V-R, V-T, R-T).
	16-18	Instantaneous Tilt Angle (V-R, V-T, R-T).
	19-21	Instantaneous Rise Angle (V-R, V-T, R-T).
Covariance Analysis [Jurkevics, 1988]	22	Azimuth Angle.
	23	Incidence Angle.
	24	Planarity.
	25	Rectilinearity.
Complex Covariance Analysis [Vidale, 1986]	26	Dip Angle.
	27	Strike Angle.
	28	Strength of Polarization.
	29	Degree of planar polarization.
Singular Value Decomposition [De Franco, 2001], [Tiapkina et al., 2012]	30	Ground roll detector.
	31	Energy.
	32	Planarity.
	33	Rectilinearity along the first principal axis.
	34	Rectilinearity along the second principal axis.
Spectral Analysis [Tiapkina et al., 2012]	35-37	Centroid of the power spectrum (V, R, T).
Spectrum of Polarization Ellipsoid [Pinnegar, 2006]	38	Semi-major axis S spectrum.
	39	Semi-minor axis S spectrum.
	40	Centroid of the power spectrum (V, R, T).
	41	Difference between semi-major and semi-minor axis S spectrum.
	42	Total-power S spectrum.
	43	Inclination S spectrum.
	44	Argument of maximum S spectrum.
	45	Phase S spectrum.

figure, we may conclude that only three attributes are necessary to achieve the best result (see list in Table 2.4).

Table 2.2 Information about seismic acquisitions for the three sets of real data used in this work.

Acquisition Parameters	**Field Data 1**	**Field Data 2**	**Field Data 3**
Source type	Explosive gel	Explosive gel/caps	Explosive gel/caps
Load Size	1800/2250 g	150 g	150 g
Source Depth	10 m	10 m	10 m
Receiver Interval	10 m	5 m	5 m
Maximum Offset	1.8 Km	100 m	300 m
Sampling Rate	2 ms	0.5 ms	0.5 ms
Data Bandwidth	3-120 Hz	5-450 Hz	5-500 Hz

Figure 2.4 Vertical, Radial and Transverse components of the first dataset.

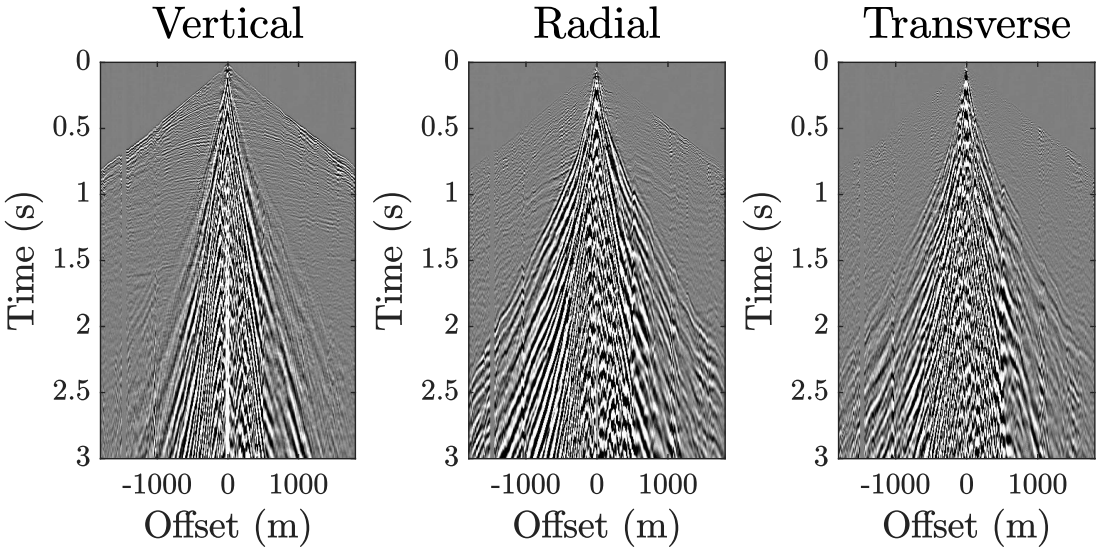

The figure showing the labeled zones and the scatter-plot of two attributes are shown in Figure 2.10a and 2.10b, respectively. In Figure 2.10c the surface wave zones are detected by using k-means with $k = 2$, and Figure 2.10d shows the correspondent cross-plot with two attributes as surface waves in this dataset present a homogeneous behavior, the classification was not performed by clustering in the detected surface waves but in the entire dataset. Then, the classification of these surface waves is realized by using k-means with $k = 3$, as shown in Figure 2.10e. The algorithm allows to identify a second zone of surface waves. The green area may correspond to the backscattered surface waves. The corresponding cross-plot with the same two attributes are shown in Figure 2.10f.

Figure 2.5 a) Correlation Matrix using the 45 seismic attributes computed in the first dataset. b) Accuracy of classification using k-means and labeled data like function of number of attributes.

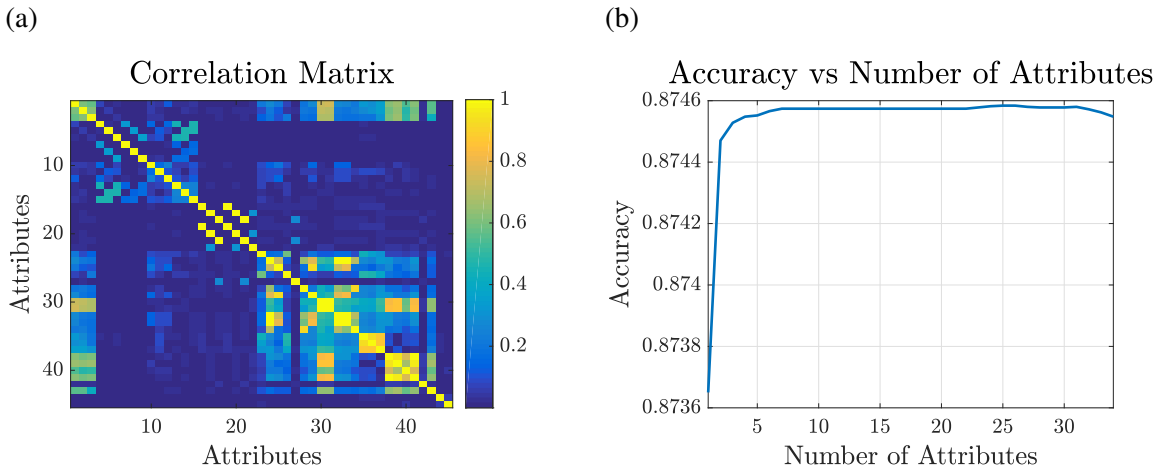

Table 2.3 Ranking of the best attributes for field data example 1. V: Vertical Component, R: Radial Component and T: Transverse Component

Rank position	**Seismic attribute**	**Attribute extraction method**
1	Semi-major axis S spectrum.	Spectrum of Polarization Ellipsoid
2	Centroid of the power spectrum (R).	Spectral Analysis
3	Centroid of the power spectrum (T).	Spectral Analysis
4	Instantaneous Frequency (V).	Instantaneous Complex Trace
5	Instantaneous Phase (T).	Instantaneous Complex Trace
6	Instantaneous Reciprocal Ellipticity (V-T).	Instantaneous Complex Trace
7	Instantaneous Reciprocal Ellipticity (V-R).	Instantaneous Complex Trace
8	Rectilinearity along the first principal axis	Singular Value Decomposition
9	Rectilinearity along the second principal axis.	Singular Value Decomposition
10	Instantaneous Amplitude (V)	Instantaneous Complex Trace
11	Instantaneous Amplitude (R)	Instantaneous Complex Trace
12	Instantaneous Amplitude (T)	Instantaneous Complex Trace

2.4.3 Field data example 3

The shot gathers of the third dataset are shown in Figure 2.11. In this kind of data, a very inhomogeneous behavior within the surface waves zone is present. In this case the two steps of the flowchart in Figure 2.3 were not performed. Instead, we took the same attributes selected in the previous case to detect the surface waves. Figures 2.12a and 2.12b depict the

Figure 2.6 Results of surface waves detection for dataset 1. a) Areas from the seismic record labeled by experts. b) Dispersion data from label areas c) Labeled areas by k-means with $k = 2$ d) Dispersion data from label areas by k-means with $k = 2$ e) Labeled areas by k-means with $k = 2$ inside the surface waves cone.

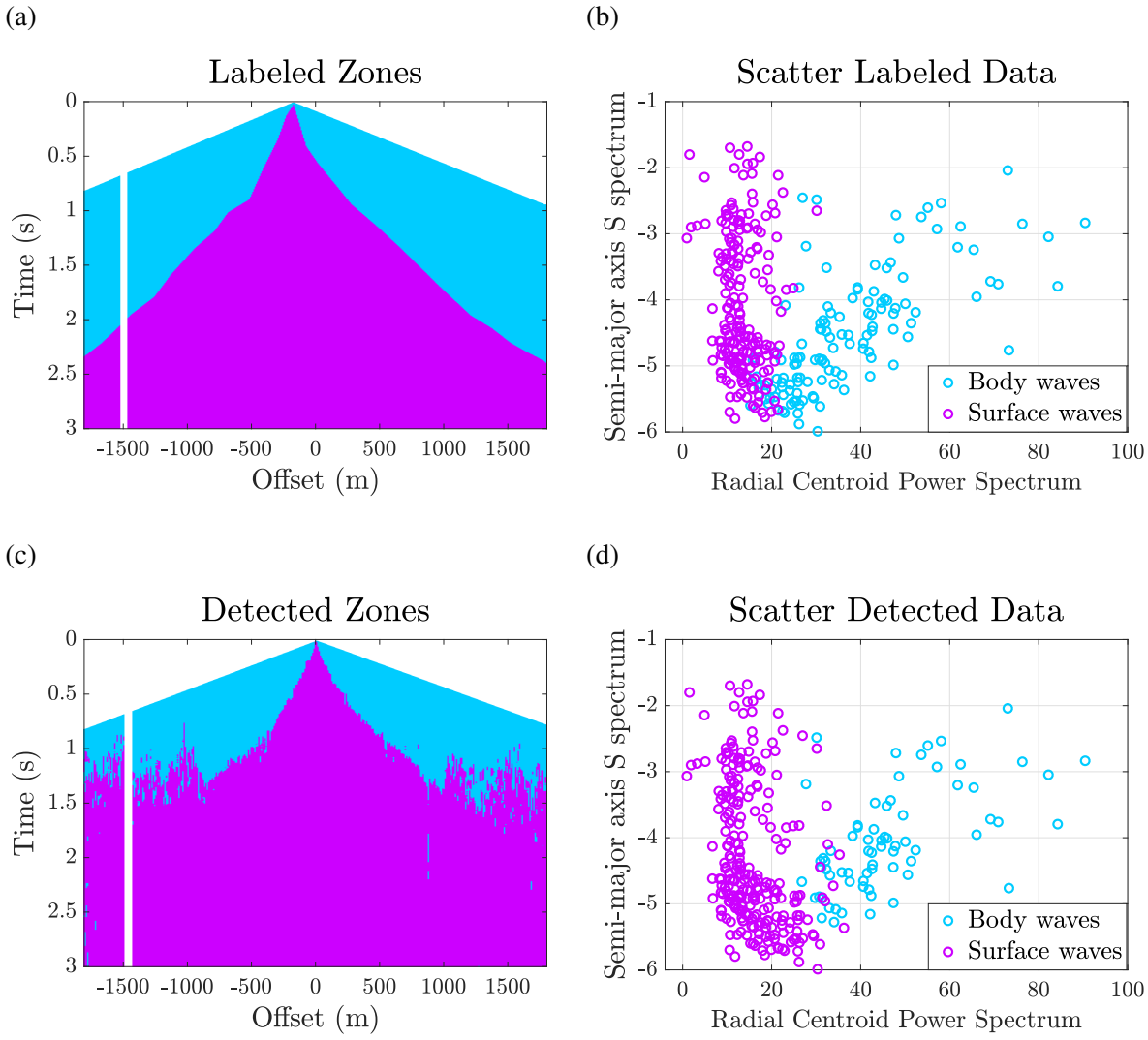

results of the detection by using k-means with $k = 2$ and Figures 2.12c and 2.12d the results of the detection by using k-means with $k = 3$.

2.5 Discussion and Conclusion

Seismic attributes for surface waves detection allow to numerically differentiate between surface waves from reflections. In some cases, this differentiation is realized by determining

Figure 2.7 Results of surface waves classification. a) Labeled areas by k-means with $k = 2$ inside the surface waves cone b) Dispersion data from label areas by k-means with $k = 3$ inside the ground roll cone c) Labeled areas by k-means with $k = 3$ allow to identify three different wave modes within surface waves cone d) Dispersion data from labeled areas by k-means with $k = 3$ inside the surface waves cone.

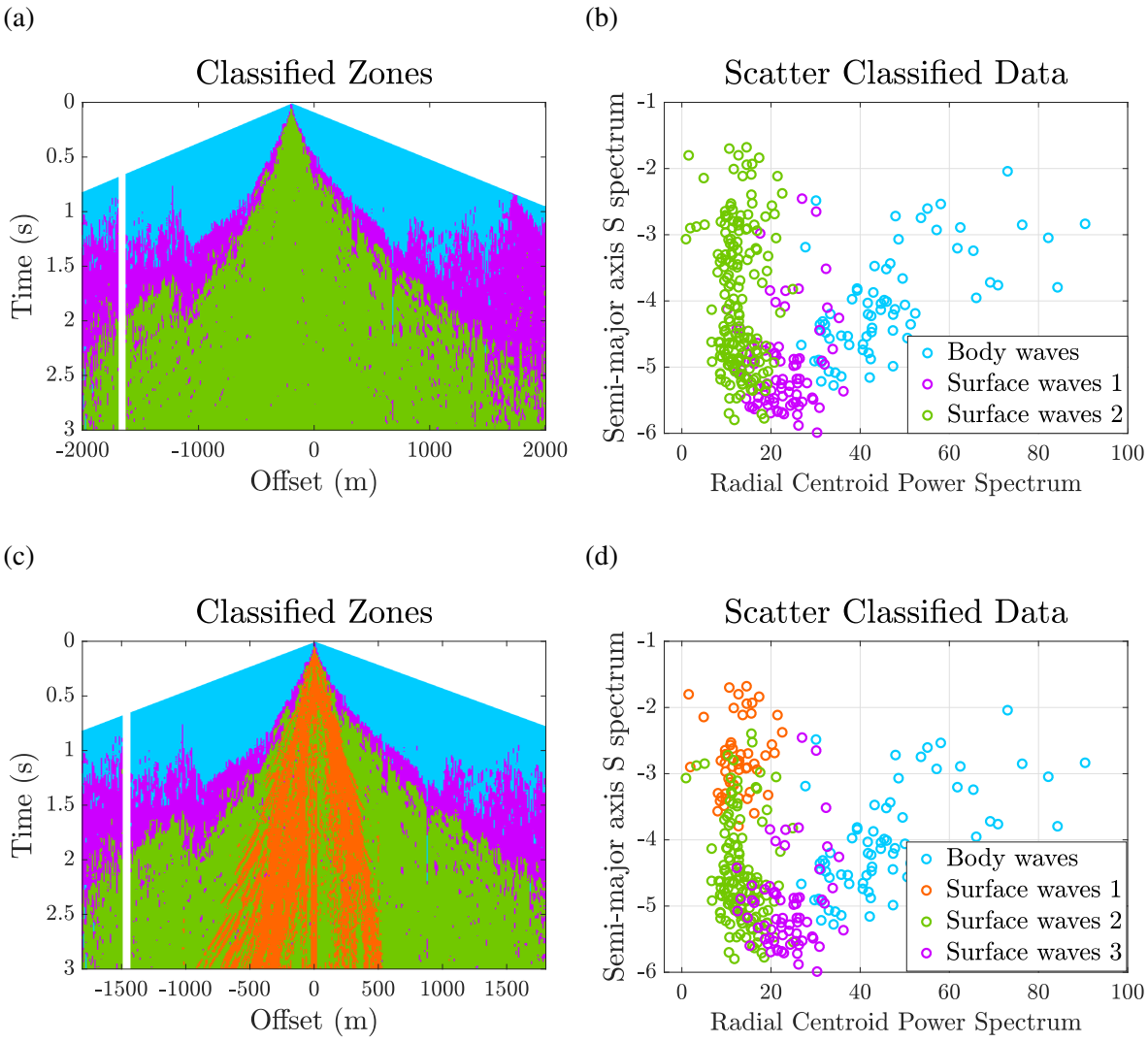

thresholds in a heuristic way. Then results are biased by the human judgment; to mitigate possible errors with these methods, minimizing the classification cost function as solution.

From the previous results, it is clear that not all attributes are created equal. In our field data example, some attributes had high correlation and it was necessary a stage of attribute selection to have an optimal set of attributes. These seismic attributes can be clustered in families where each family can describe an attribute in particular.

Figure 2.8 Vertical, Radial and Transverse components of the second dataset.

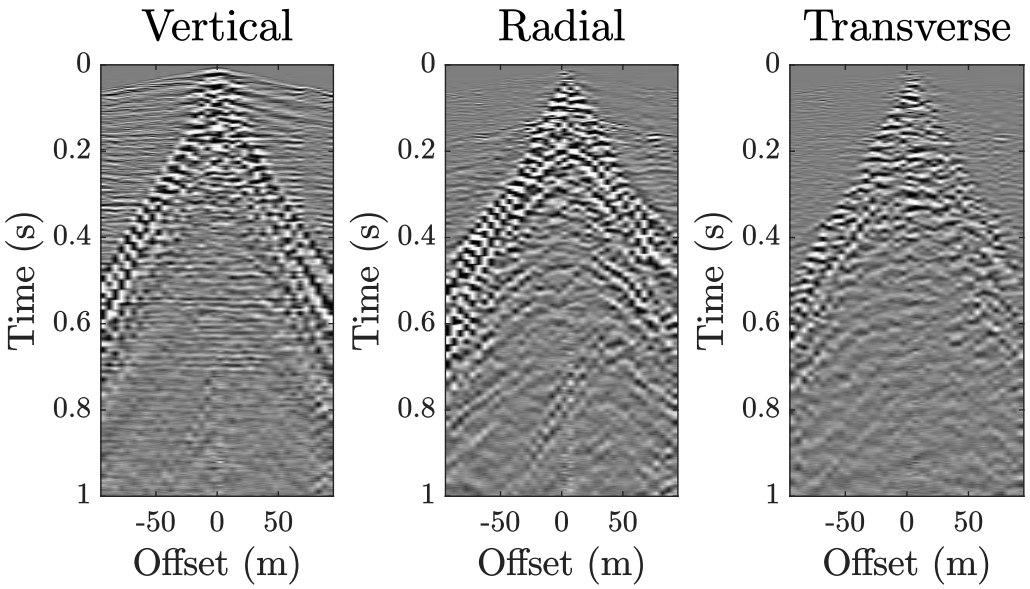

Table 2.4 Ranking of the best attributes for field data example 2. V: Vertical Component, R: Radial Component and T: Trasversal Component

Rank position	**Seismic attribute**	**Attribute extraction method**
1	Incidence Angle.	Covariance Analysis
2	Energy.	Singular Value Decomposition
3	Instantaneous Reciprocal Ellipticity (V-R)	Instantaneous Complex Trace

Based on the results obtained in the detection of the surface waves cone of Figure 2.1a, it is possible to conclude that in spite of the fact that the automatic detection differs from the manually labeled data in the adjacent zones just above the cone, in general the attributes were able to successfully describe the surface-wave behavior to ease its automatic distinction from the body waves. When the difference area (violet color) is examined, corresponds to a zone with different characteristics from the body waves and the surface waves, possibly is related to S-wave refractions and guided waves. A further *k*-means classification separates a green and orange area. The green area may be interpreted as higher modes of Rayleigh waves, while the orange is possibly related to scattering and reverberations.

The results in the field data example 2 are quite different from what was obtained in the first example. There is no differentiated inner surface waves cone, but only a strong outer limit band (associated with pure Rayleigh waves). When performing the attribute selection and classification, unlike the previous case, only this strong amplitude outer band is clearly

Figure 2.9 a) Correlation Matrix using the 45 seismic attributes computed in the second dataset. b) Accuracy of classification using *k*-means and labeled data like function of number of attributes.

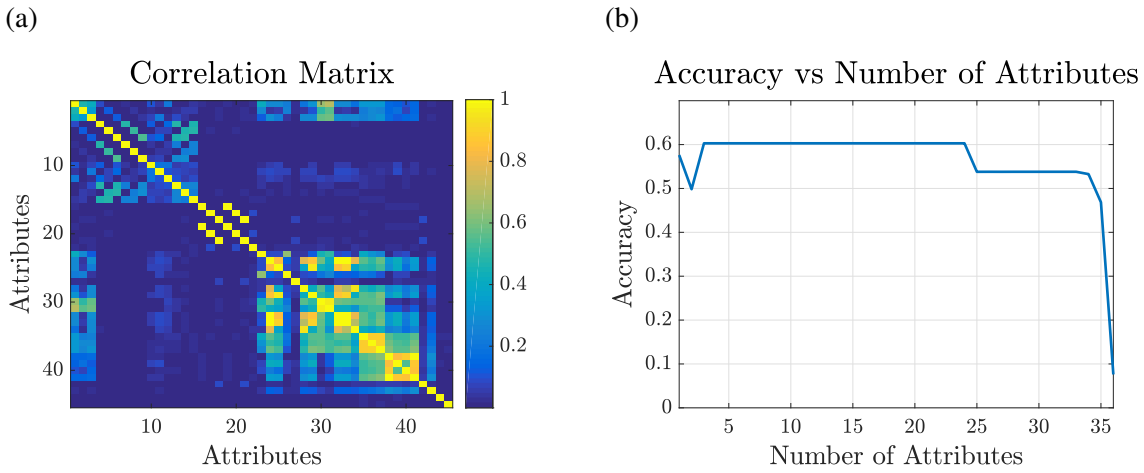

identified by the algorithm. The absence of inner energy in the surface waves cone can be explained by two characteristics in the seismic source: (1) It is a small source (explosive mass 150 g) of low energy and high frequency, so that reverberations and scattering resulting of medium heterogeneities are reduced (the relation of wavelength and near surface thickness and heterogeneity size has changed) (2) Unlike the clearly cylindrical 1800 g source of the first field data (explosive dimensions were 320 cm height and 15 cm hole diameter), the 150 g source was closer to a spherical source (15 cm x 15 cm) which is more symmetrical and less prone to generate shear energy. It is interesting to notice that a possible Rayleigh wave backscattering linear event is partially identified by the algorithm (green color linear event with negative slope starting at 0.6 s and offset +50 m in Figure 2.10a).

The field data example 3 (Figure 2.11) was performed in a zone with rough topography and rapidly varying near surface properties (thickness and velocity). In this case, a human interpretation is challenging due to the complexity in the surface waves characteristics. Here pattern recognition techniques show at its best. We used the attributes chosen in a flat topography area (field data example 2), where they can be guided during the relevance filter stage and then applied in the more complex data example 3. Surface waves limit is clearly identified (green color Figure 2.12c). A band of high amplitude is identified (violet color) that could correspond to a localized scattering caused by the topographic and thickness variations in this rough topography area.

Two disadvantages of the *k*-means algorithm are: (1) the location of the seeds needed to start the iterative process and the optimal number of clusters *k* that best clusters the dataset

must be determined for each problem. (2) the selection of the seed's position in this paper is done randomly. Random seeding is the simplest form of seeding, as a future work, it is highly recommended to find the optimum values of the k clusters and trying different methods for seeding selection.

Our selection of seismic attributes has been somehow biased towards single-station multicomponent attributes. A suggested continuation of this work involves the use of multi-station seismic attributes to take into account other attributes like the velocity (slope) of movement of the particles [Bear et al., 1999], [De Meersman et al., 2006]. Applications of surface waves classification involves design of adaptive filters for ground roll attenuation and studies in near-surface characterization through surface wave inversion adapted to each wave mode identified inside the surface waves cone.

2.6 Acknowledgments

This work was carried on the framework of the Agreement "*Acta No. 4 del Convenio de Cooperación Tecnológica 5211794*" between Universidad Industrial de Santander and Ecopetrol S.A.- Instituto Colombiano del Petróleo. The work in this chapter was done with the participation of Yenni Villa. We are grateful to Saúl Guevara and Carlos Niño for the fruitful discussions about the use of attributes in surface waves classification.

Figure 2.10 Results of surface waves detection and classification for dataset 2. a) Areas from the seismic record labeled by experts. b) Dispersion data of labeled areas. c) Areas detected by k-means with $k = 2$. d) Dispersion data of detected areas by k-means with $k = 2$. f) Areas classified by k-means with $k = 3$. Two different wave modes of surface waves were identified. f) Dispersion data of detected areas by k-means with $k = 3$.

(a)

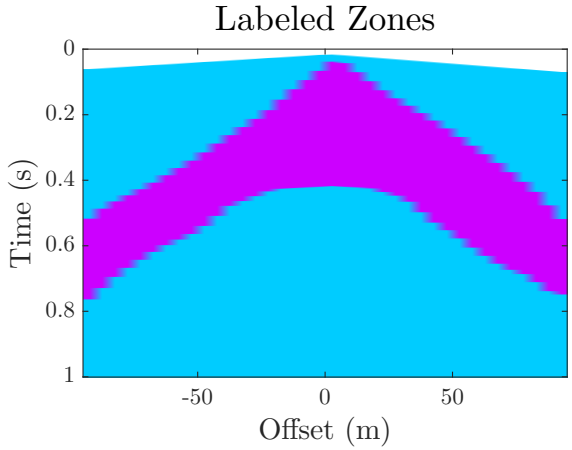

(b)

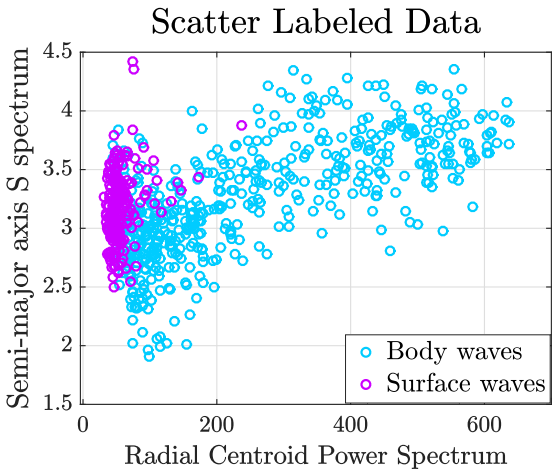

(c)

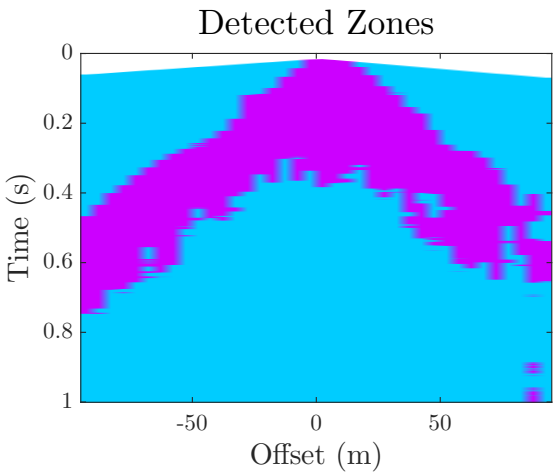

(d)

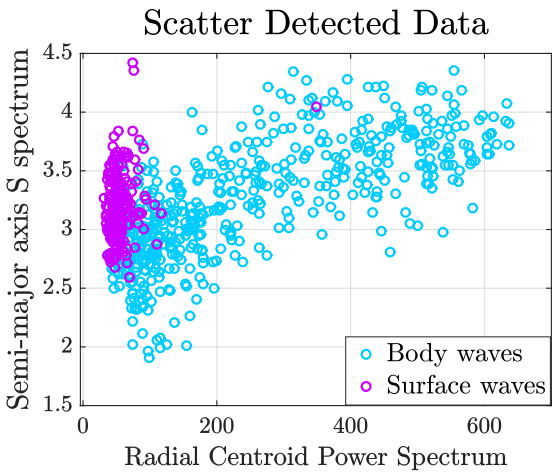

(e)

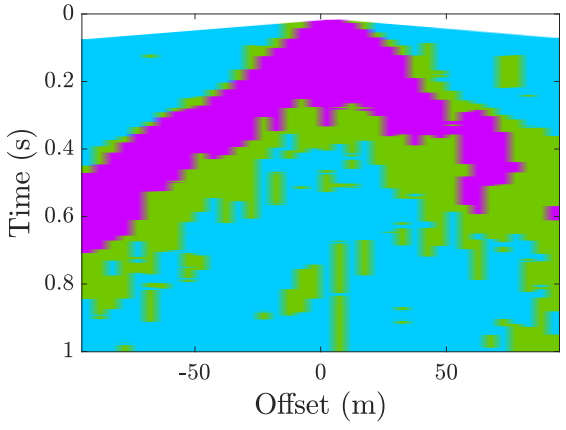

(f)

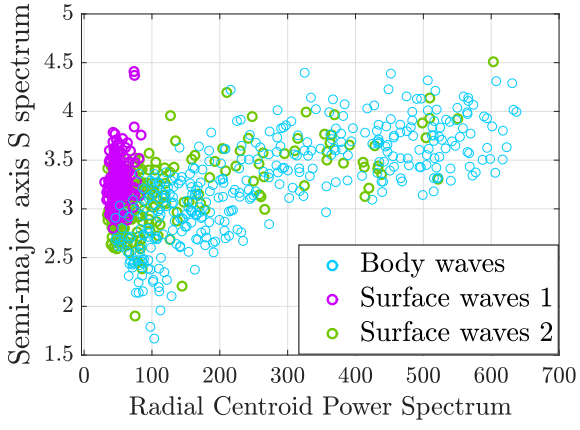

Figure 2.11 Vertical, Radial and Transverse components of the third dataset.

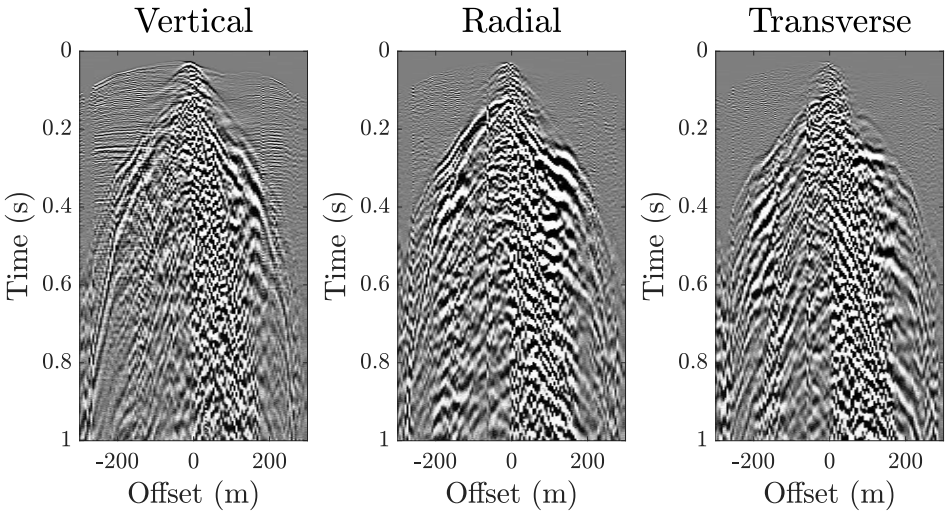

Figure 2.12 Results of surface waves detection and classification for dataset 3. a) Areas classified by k-means with $k = 2$. b) Dispersion data of detected areas with $k = 2$. c) Areas classified by k-means with $k = 3$. d) Dispersion data of detected areas $k = 3$.

(a)

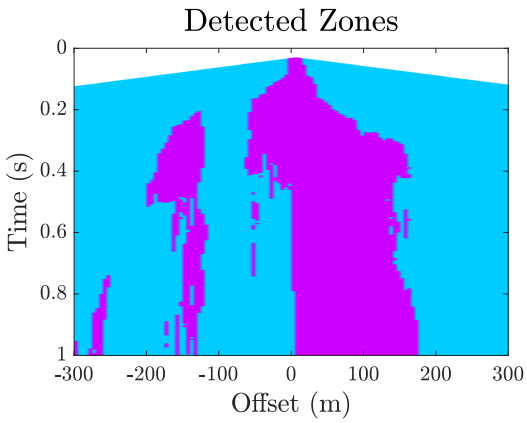

(b)

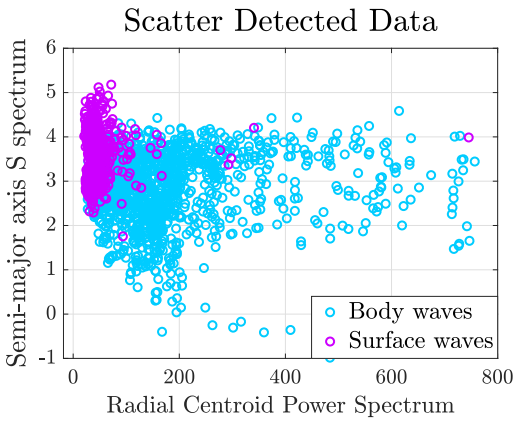

(c)

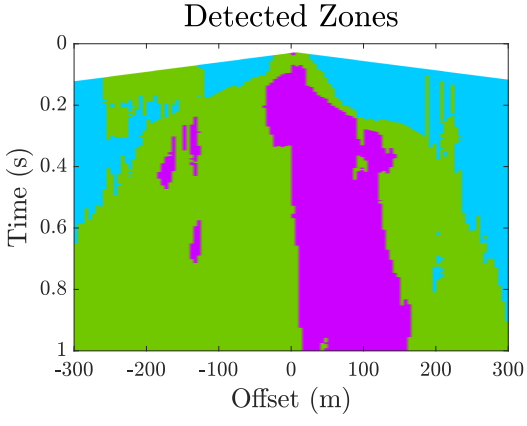

(d)

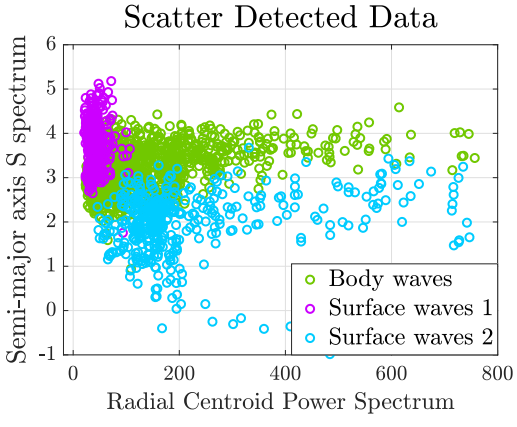

Chapter 3

2D Finite difference elastic wave modeling

Abstract

Real seismograms are contaminated by different kind of noise and it is difficult for geophysicists to relate physical properties in the signal with the model of the Earth's subsurface, which is not known. For its part, synthetic seismograms are indispensable for seismic signal processing. Because avoiding signal noise can help to extract physical characteristics in the seismic signal to estimate mechanical properties of materials inside the Earth. In that sense, A 2D finite differences method with second order accurate in time and fourth order accurate in space is implemented to model elastic wave propagation. The numerical test showed the performance of the algorithm implemented where the correlation between numerical and analytical seismograms were higher than 99% for most simulation tests.

3.1 Introduction

Numerical modeling of elastic waves has been used to study how seismic waves are propagated inside the Earth. This study has allowed geophysicists to interpret seismograms in order to build an image of the Earth's subsurface. Seismograms are signals that contains information of physical phenomena presented in seismic waves propagation (eg. Reflections, refractions, diffractions, scattering, dispersion). This information is used to estimate mechanical properties of materials of which the Earth is formed.

There are several reasons by which numerical modeling of elastic wave propagation in complex media is important. We are going to mention two reasons. First, realistic synthetic

seismic data are required to evaluate the performance from seismic data processing tools. Synthetic data help researchers to tune or improve their algorithms in order to achieve better results. Second, information about behavior of seismic wave propagation in complex media is unreliable using only seismic real data, this is because barely a small portion of the seismic wave-field is measured since seismic acquisitions are realized in the surface of the Earth. Therefore, a complete wave-field to study seismic waves propagation in complex media only is possible through numerical modeling of waves.

Two common problems should be treated when elastic wave modeling in complex media is developed. Surface topography and curvilinear interfaces are the principal challenges to be faced. The first because free-surface condition should be satisfied, thus normal stress at topography should be set to zero. The second because spurious values are generated in the numerical solution since the grid is not adapted with the interface.

Several methods have been proposed in order to solve these problems. For the case of modeling via finite differences have been proposed three different approaches to include free-surface topography in the earth models. The first approach is refining the grid in the curvilinear surface and the shape of the topography are approximated by small vertical and horizontal lines [Robertsson, 1996] [Moczo et al., 2007] [Zeng et al., 2012]. The second approach is compute fictitious values of the solution near the surface outside of the model to estimate the true values in the points inside the model [Lombard et al., 2008] [Almuhaidib and Toksöz, 2015]. The third approach is solving the elastic wave equation using curvilinear coordinates, so that the grid is adapted to the shape of the topography [Hestholm and Ruud, 1998] [Zhang and Chen, 2006] [Solano et al., 2016].

In this chapter, a review about two-dimensional finite-difference modeling of elastic waves, is presented. We have focused our attention in considerations that should be taken into account to model elastic wave propagation in complex media. Surface topography is contemplated in the earth models aiming to produce realistic seismic data. For this, the improved vacuum formulation is implemented, which requires a number of ppw higher than conventional modeling to ensure accurate Rayleigh waves. Numerical results are contrasted with analytic solutions showing the performance of the algorithm implemented.

3.2 Elastic wave modeling

Seismic waves can be represented as elastic waves. For a homogeneous and isotropic medium, the elastic wave propagation is governed by equation 3.1.

$$\rho \frac{\partial^2 \boldsymbol{u}}{\partial t^2} = (\lambda + 2\mu)\nabla\nabla \cdot \boldsymbol{u} - \mu \nabla \times \nabla \times \boldsymbol{u}. \tag{3.1}$$

Where $\boldsymbol{u}$ is the displacement vector; λ, μ and ρ are the elastic parameters from earth model (Lamé parameters and density). Commonly, the elastic parameters are given in terms of P-wave velocity and S-wave velocities, V_P and V_S respectively.

$$V_P = \sqrt{\frac{\lambda + 2\mu}{\rho}}, \qquad V_S = \sqrt{\frac{\mu}{\rho}} \tag{3.2}$$

For numerical modeling via finite-difference, is preferred the velocity-stress formulation introduced by [Virieux, 1986]. The two-dimensional elastic wave propagation in velocity-stress formulation is governed by equations 3.3.

$$\begin{aligned}
\frac{\partial v_x}{\partial t} &= \frac{1}{\rho}\left(\frac{\partial \sigma_{xx}}{\partial x} + \frac{\partial \sigma_{xz}}{\partial z}\right) + \varphi_{v_x}, \\
\frac{\partial v_z}{\partial t} &= \frac{1}{\rho}\left(\frac{\partial \sigma_{xz}}{\partial x} + \frac{\partial \sigma_{zz}}{\partial z}\right) + \varphi_{v_z}, \\
\frac{\partial \sigma_{xx}}{\partial t} &= (\lambda + 2\mu)\frac{\partial v_x}{\partial x} + \lambda \frac{\partial v_z}{\partial z} + \varphi_{\sigma_{xx}}, \\
\frac{\partial \sigma_{zz}}{\partial t} &= (\lambda + 2\mu)\frac{\partial v_z}{\partial z} + \lambda \frac{\partial v_x}{\partial x} + \varphi_{\sigma_{zz}}, \\
\frac{\partial \sigma_{xz}}{\partial t} &= \mu\left(\frac{\partial v_x}{\partial z} + \frac{\partial v_z}{\partial x}\right) + \varphi_{\sigma_{xz}},
\end{aligned} \tag{3.3}$$

Where x and z are the Cartesian coordinates; v_x and v_z are the velocity components; σ_{xx}, σ_{zz} and σ_{xz}; and φ represents the source term.

3.2.1 Free-surface condition

In numerical modeling of seismic waves, the medium of propagation is the Earth subsurface. Given that the medium above the Earth's surface is the air, and the air is replaced by vacuum in most of applications, the Earth's surface is considered a traction-free surface [Moczo et al., 2014]. This condition states that the stress component normal to the surface is set of zero. If the surface is a planar interface perpendicular to the z-axis (vertical axis), the condition is

$$\sigma_{ij} n_{ij} = 0; \qquad \sigma_{iz} = 0; \qquad i \in \{x, z\} \tag{3.4}$$

Therefore, the elastic waves propagation in the surface is governed by 3.5.

$$\frac{\partial v_z}{\partial z} = -\frac{\lambda}{\lambda + 2\mu}\frac{\partial v_x}{\partial x}, \qquad \frac{\partial v_x}{\partial z} = -\frac{\partial v_z}{\partial x}, \tag{3.5}$$

3.2.2 Convolutional perfectly matched layer

The non-reflective boundaries are necessary conditions in the modeling of seismic waves because the computational domain is a finite space. The perfectly matched layer (PML) is an efficient method to prevent reflections of seismic waves at boundaries in the computational domain. The PML was proposed by [Berenger, 1994] for absorbing electromagnetic waves. The application of PML into modeling of seismic waves was introduces by [Chew and Liu, 1996] and [Hastings et al., 1996]. The convolutional PML (C-PML) technique was proposed by [Komatitsch and Martin, 2007]. This technique improves the accuracy of the PML at grazing incidence.

The Convolutional PML for elastic implementation is

$$\begin{aligned}
\frac{\partial v_x}{\partial t} &= \frac{1}{\rho}\left(\frac{\partial \sigma_{xx}}{\partial x} + \frac{\partial \sigma_{xz}}{\partial z}\right) - \Omega_{xx} - \Omega_{xz}, \\
\frac{\partial v_z}{\partial t} &= \frac{1}{\rho} + \frac{1}{2}\left(\frac{\partial \sigma_{xz}}{\partial x} + \frac{\partial \sigma_{zz}}{\partial z}\right) - \Omega_{zx} - \Omega_{zz}, \\
\frac{\partial \sigma_{xx}}{\partial t} &= (\lambda + 2\mu)\frac{\partial v_x}{\partial x} + \lambda \frac{\partial v_z}{\partial z} - (\lambda + 2\mu)\Psi_{xx} - \lambda \Psi_{zz}, \\
\frac{\partial \sigma_{zz}}{\partial t} &= (\lambda + 2\mu)\frac{\partial v_z}{\partial z} + \lambda \frac{\partial v_x}{\partial x} - \lambda \Psi_{xx} - (\lambda + 2\mu)\Psi_{zz}, \\
\frac{\partial \sigma_{xz}}{\partial t} &= \mu\left(\frac{\partial v_x}{\partial z} + \frac{\partial v_z}{\partial x}\right) - \mu \Psi_{zx} - \mu \Psi_{xz}
\end{aligned} \tag{3.6}$$

the auxiliary variables are governed by equation 3.7.

$$\begin{aligned}
\frac{\partial \Omega_{xx}}{\partial t} + d(x)\Omega_{xx} &= d(x)\frac{\partial \sigma_{xx}}{\partial x}, & \frac{\partial \Omega_{xz}}{\partial t} + d(z)\Omega_{xz} &= d(z)\frac{\partial \sigma_{xz}}{\partial z}, \\
\frac{\partial \Omega_{zx}}{\partial t} + d(x)\Omega_{zx} &= d(x)\frac{\partial \sigma_{xx}}{\partial x}, & \frac{\partial \Omega_{zz}}{\partial t} + d(z)\Omega_{zz} &= d(z)\frac{\partial \sigma_{zz}}{\partial z}, \\
\frac{\partial \Psi_{xx}}{\partial t} + d(x)\Psi_{xx} &= d(x)\frac{\partial v_x}{\partial x}, & \frac{\partial \Psi_{xz}}{\partial t} + d(z)\Psi_{xz} &= d(z)\frac{\partial v_x}{\partial z}, \\
\frac{\partial \Psi_{zx}}{\partial t} + d(x)\Psi_{zx} &= d(x)\frac{\partial v_z}{\partial x}, & \frac{\partial \Psi_{zz}}{\partial t} + d(z)\Psi_{zz} &= d(z)\frac{\partial v_z}{\partial z},
\end{aligned} \tag{3.7}$$

Where $d(x)$ and $d(z)$ are coefficients functions used to attenuate the reflections in the C-PML zone. A model for the coefficients function proposed by [Collino and Tsogka, 2001] is showed in equations 3.8.

$$\begin{aligned}
d(u) &= d_0\left(\frac{u}{L}\right)^2, \qquad u = \{x, z\}, \\
d_0 &= -\frac{3V}{2L}\ln(R),
\end{aligned} \tag{3.8}$$

Where L is the length of the attenuation zone, the parameter V is a chosen velocity in the model (commonly the maximum velocity V_p), and the constant R is always chosen as $10^{-3} \sim 10^{-6}$. A numerical example of the absorption of the C-PML for elastic wave propagation is shown in Figure 3.1.

Figure 3.1 Elastic wave propagation trough a medium defined by $V_p = 3000$ (m/s), $V_s = 1730$ (m/s). $\rho = 2500$ (kg/m) . a) $t = 0.3$ (s). b) $t = 0.4$ (s). c) $t = 0.5$ (s). d) $t = 0.6$ (s).

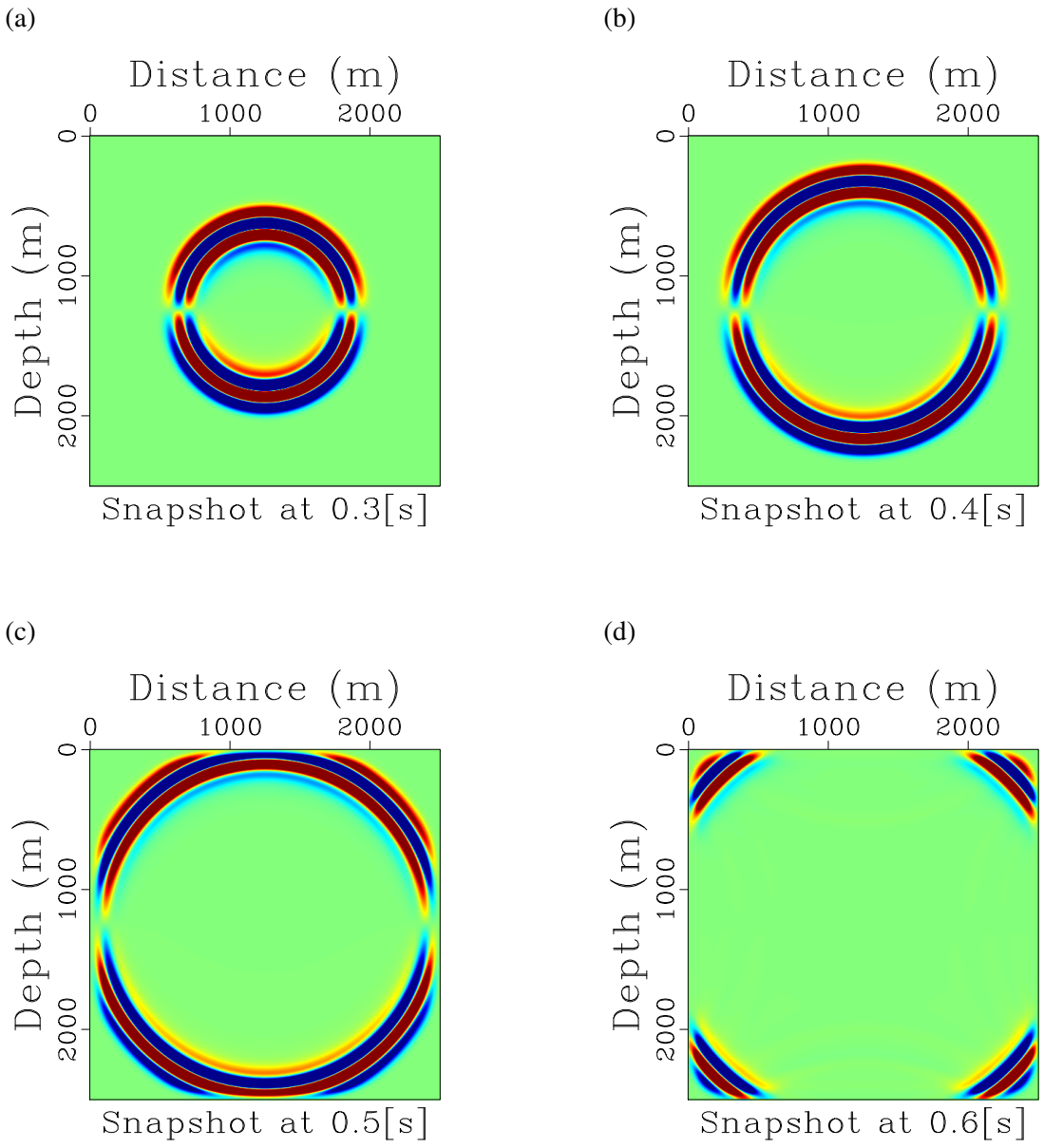

3.2.3 Discretization

For the implementation of equations 3.3, 3.6, 3.7; we use a second-order discretization in time and a fourth-order discretization in space. The time and space derivatives of a generic function $f^t_{(x,z)}$ are discretized as:

$$\begin{aligned}
\frac{\partial f^t_{(x,z)}}{\partial t} &= \frac{1}{\Delta t}\left[f^{t+\frac{\Delta t}{2}}_{(x,z)} - f^{t-\frac{\Delta t}{2}}_{(x,z)}\right] \\
\frac{\partial f^t_{(x,z)}}{\partial x} &= \frac{1}{\Delta x}\left[\frac{9}{8}\left(f^t_{(x+\frac{\Delta x}{2},z)} - f^t_{(x-\frac{\Delta x}{2},z)}\right) - \frac{1}{24}\left(f^t_{(x+\frac{3\Delta x}{2},z)} - f^t_{(x-\frac{3\Delta x}{2},z)}\right)\right] \\
\frac{\partial f^t_{(x,z)}}{\partial z} &= \frac{1}{\Delta z}\left[\frac{9}{8}\left(f^t_{(x,z+\frac{\Delta z}{2})} - f^t_{(x,z-\frac{\Delta z}{2})}\right) - \frac{1}{24}\left(f^t_{(x,z+\frac{3\Delta z}{2})} - f^t_{(x,z-\frac{3\Delta z}{2})}\right)\right]
\end{aligned} \tag{3.9}$$

Where Δt represents the time differentiation step and Δx and Δz represent the space differentiation steps in the horizontal and vertical components respectively. Defining indices (i,k,n) as the discretized x-axis, z-axis and time, the discretized time and space derivatives are:

$$\begin{aligned}
\frac{\partial f^t_{(x,z)}}{\partial t} &= \frac{1}{\Delta t}\left[f^{n+\frac{1}{2}}_{(i,k)} - f^{n-\frac{1}{2}}_{(i,k)}\right] \\
\frac{\partial f^t_{(x,z)}}{\partial x} &= \frac{1}{\Delta x}\left[\frac{9}{8}\left(f^n_{(i+\frac{1}{2},x)} - f^n_{(i-\frac{1}{2},k)}\right) - \frac{1}{24}\left(f^n_{(i+\frac{3}{2},k)} - f^n_{(i-\frac{3}{2},k)}\right)\right] \\
\frac{\partial f^t_{(x,z)}}{\partial z} &= \frac{1}{\Delta z}\left[\frac{9}{8}\left(f^n_{(i,k+\frac{1}{2})} - f^n_{(i,k-\frac{1}{2})}\right) - \frac{1}{24}\left(f^n_{(i,k+\frac{3}{2})} - f^n_{(i,k-\frac{3}{2})}\right)\right]
\end{aligned} \tag{3.10}$$

The spatial sampling Δx and Δz are set of be the same value Δh to avoid anisotropic effects in the numerical modeling. The value of Δh depends on the maximum dispersion condition accepted in the simulation such that

$$\Delta h \leq \frac{\lambda_{min}}{n_\lambda} = \frac{V_{min}}{f_{max} n_\lambda} \tag{3.11}$$

Where λ_{min} corresponds to the minimum wavelength in the medium, V_{min} is the minimum velocity in the medium, f_{max} is the maximum frequency of the source and the value n_λ is the number of points per wavelength (ppw). It is commonly set above 16 ppw. The higher n_λ, the lower numerical dispersion in the simulation [Virieux, 1986].

The time step Δt depends on the condition for numerical stability. According to [Lines et al., 1999], in the case of second-order discretization in time and fourth-order discretization in space, the condition is:

$$\Delta t \leq \sqrt{\frac{3}{8}}\frac{\Delta h}{V_{max}} \tag{3.12}$$

Where V_{max} is the maximum velocity in the medium.

For the discretization of equations 3.3, 3.6, 3.7; we use the staggered grid proposed by [Robertsson, 1996], which is shown in Figure 3.2.

Figure 3.2 The staggered-grid scheme used for the discretization.

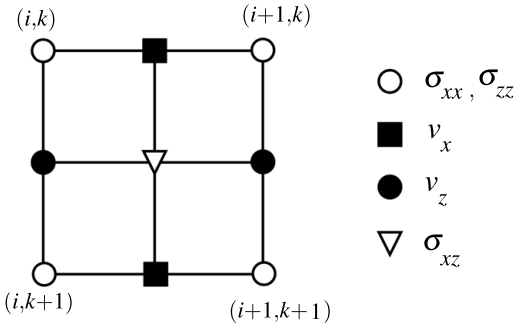

The discretized equations for numerical modeling of elastic wave propagation are:

Equations in the regular zone

$$\begin{aligned}
v^{n}_{x(i+\frac{1}{2},k)} =& v^{n-1}_{x(i+\frac{1}{2},k)} - \frac{\Delta t}{\rho_{i+\frac{1}{2},k}\Delta x}\left[\frac{9}{8}(\sigma^{n-\frac{1}{2}}_{xx(i+1,k)} - \sigma^{n-\frac{1}{2}}_{xx(i,k)}) - \frac{1}{24}(\sigma^{n-\frac{1}{2}}_{xx(i+2,k)} - \sigma^{n-\frac{1}{2}}_{xx(i-1,k)})\right] \\
& - \frac{\Delta t}{\rho_{i+\frac{1}{2},k}\Delta z}\left[\frac{9}{8}(\sigma^{n-\frac{1}{2}}_{xz(i+\frac{1}{2},k+\frac{1}{2})} - \sigma^{n-\frac{1}{2}}_{xz(i+\frac{1}{2},k-\frac{1}{2})}) - \frac{1}{24}(\sigma^{n-\frac{1}{2}}_{xz(i+\frac{1}{2},k+\frac{3}{2})} - \sigma^{n-\frac{1}{2}}_{xz(i+\frac{1}{2},k-\frac{3}{2})})\right] \\
v^{n}_{z(i,k+\frac{1}{2})} =& v^{n-1}_{z(i,k+\frac{1}{2})} - \frac{\Delta t}{\rho_{i,k+\frac{1}{2}}\Delta x}\left[\frac{9}{8}(\sigma^{n-\frac{1}{2}}_{xz(i+\frac{1}{2},k+\frac{1}{2})} - \sigma^{n-\frac{1}{2}}_{xz(i-\frac{1}{2},k+\frac{1}{2})}) - \frac{1}{24}(\sigma^{n-\frac{1}{2}}_{xz(i+\frac{3}{2},k+\frac{1}{2})} - \sigma^{n-\frac{1}{2}}_{xz(i-\frac{3}{2},k+\frac{1}{2})})\right] \\
& - \frac{\Delta t}{\rho_{i,k+\frac{1}{2}}\Delta z}\left[\frac{9}{8}(\sigma^{n-\frac{1}{2}}_{zz(i,k+1)} - \sigma^{n-\frac{1}{2}}_{zz(i,k)}) - \frac{1}{24}(\sigma^{n-\frac{1}{2}}_{zz(i,k+2)} - \sigma^{n-\frac{1}{2}}_{zz(i,k-1)})\right] \\
\sigma^{n+\frac{1}{2}}_{xx(i,k)} =& \sigma^{n-\frac{1}{2}}_{xx(i,k)} - \frac{\Delta t(\lambda_{i,k}+2\mu_{i,k})}{\Delta x}\left[\frac{9}{8}(v^{n}_{x(i+\frac{1}{2},k)} - v^{n}_{x(i-\frac{1}{2},k)}) - \frac{1}{24}(v^{n}_{x(i+\frac{3}{2},k)} - v^{n}_{x(i-\frac{3}{2},k)})\right] \\
& - \frac{\Delta t\lambda_{i,k}}{\Delta z}\left[\frac{9}{8}(v^{n}_{z(i,k+\frac{1}{2})} - v^{n}_{z(i,k-\frac{1}{2})}) - \frac{1}{24}(v^{n}_{z(i,k+\frac{3}{2})} - v^{n}_{z(i,k-\frac{3}{2})})\right] \\
\sigma^{n+\frac{1}{2}}_{zz(i,k)} =& \sigma^{n-\frac{1}{2}}_{zz(i,k)} - \frac{\Delta t(\lambda_{i,k}+2\mu_{i,k})}{\Delta z}\left[\frac{9}{8}(v^{n}_{z(i,k+\frac{1}{2})} - v^{n}_{z(i,k-\frac{1}{2})}) - \frac{1}{24}(v^{n}_{z(i,k+\frac{3}{2})} - v^{n}_{z(i,k-\frac{3}{2})})\right] \\
& - \frac{\Delta t\lambda_{i,k}}{\Delta x}\left[\frac{9}{8}(v^{n}_{x(i+\frac{1}{2},k)} - v^{n}_{x(i-\frac{1}{2},k)}) - \frac{1}{24}(v^{n}_{x(i+\frac{3}{2},k)} - v^{n}_{x(i-\frac{3}{2},k)})\right] \\
\sigma^{n+\frac{1}{2}}_{xz(i+\frac{1}{2},k+\frac{1}{2})} =& \sigma^{n-\frac{1}{2}}_{zz(i+\frac{1}{2},k+\frac{1}{2})} - \frac{\Delta t\mu_{i+\frac{1}{2},k+\frac{1}{2}}}{\Delta z}\left[\frac{9}{8}(v^{n}_{x(i+\frac{1}{2},k+1)} - v^{n}_{x(i+\frac{1}{2},k)}) - \frac{1}{24}(v^{n}_{x(i+\frac{1}{2},k+2)} - v^{n}_{z(i+\frac{1}{2},k-1)})\right] \\
& - \frac{\Delta t\mu_{i+\frac{1}{2},k+\frac{1}{2}}}{\Delta x}\left[\frac{9}{8}(v^{n}_{z(i+1,k+\frac{1}{2})} - v^{n}_{z(i,k+\frac{1}{2})}) - \frac{1}{24}(v^{n}_{z(i+2,k+\frac{1}{2})} - v^{n}_{z(i-1,k+\frac{1}{2})})\right]
\end{aligned} \tag{3.13}$$

Equations in the C-PML zone

$$
\begin{aligned}
v^{n}_{x(i+\frac{1}{2},k)} =& v^{n-1}_{x(i+\frac{1}{2},k)} - \frac{\Delta t}{\rho_{i+\frac{1}{2},k}\Delta x}\left[\frac{9}{8}(\sigma^{n-\frac{1}{2}}_{xx(i+1,k)} - \sigma^{n-\frac{1}{2}}_{xx(i,k)}) - \frac{1}{24}(\sigma^{n-\frac{1}{2}}_{xx(i+2,k)} - \sigma^{n-\frac{1}{2}}_{xx(i-1,k)})\right] \\
& - \frac{\Delta t}{\rho_{i+\frac{1}{2},k}\Delta z}\left[\frac{9}{8}(\sigma^{n-\frac{1}{2}}_{xz(i+\frac{1}{2},k+\frac{1}{2})} - \sigma^{n-\frac{1}{2}}_{xz(i+\frac{1}{2},k-\frac{1}{2})}) - \frac{1}{24}(\sigma^{n-\frac{1}{2}}_{xz(i+\frac{1}{2},k+\frac{3}{2})} - \sigma^{n-\frac{1}{2}}_{xz(i+\frac{1}{2},k-\frac{3}{2})})\right] - \Omega^{n}_{xx(i,k+\frac{1}{2})} - \Omega^{n}_{xz(i+\frac{1}{2},k)} \\
v^{n}_{z(i,k+\frac{1}{2})} =& v^{n-1}_{z(i,k+\frac{1}{2})} - \frac{\Delta t}{\rho_{i,k+\frac{1}{2}}\Delta x}\left[\frac{9}{8}(\sigma^{n-\frac{1}{2}}_{xz(i+\frac{1}{2},k+\frac{1}{2})} - \sigma^{n-\frac{1}{2}}_{xz(i-\frac{1}{2},k+\frac{1}{2})}) - \frac{1}{24}(\sigma^{n-\frac{1}{2}}_{xz(i+\frac{3}{2},k+\frac{1}{2})} - \sigma^{n-\frac{1}{2}}_{xz(i-\frac{3}{2},k+\frac{1}{2})})\right] \\
& - \frac{\Delta t}{\rho_{i,k+\frac{1}{2}}\Delta z}\left[\frac{9}{8}(\sigma^{n-\frac{1}{2}}_{zz(i,k+1)} - \sigma^{n-\frac{1}{2}}_{zz(i,k)}) - \frac{1}{24}(\sigma^{n-\frac{1}{2}}_{zz(i,k+2)} - \sigma^{n-\frac{1}{2}}_{zz(i,k-1)})\right] - \Omega^{n}_{zx(i,k+\frac{1}{2})} - \Omega^{n}_{zz(i,k+\frac{1}{2})} \\
\sigma^{n+\frac{1}{2}}_{xx(i,k)} =& \sigma^{n-\frac{1}{2}}_{xx(i,k)} - \frac{\Delta t(\lambda_{i,k}+2\mu_{i,k})}{\Delta x}\left[\frac{9}{8}(v^{n}_{x(i+\frac{1}{2},k)} - v^{n}_{x(i-\frac{1}{2},k)}) - \frac{1}{24}(v^{n}_{x(i+\frac{3}{2},k)} - v^{n}_{x(i-\frac{3}{2},k)})\right] \\
& - \frac{\Delta t\lambda_{i,k}}{\Delta z}\left[\frac{9}{8}(v^{n}_{z(i,k+\frac{1}{2})} - v^{n}_{z(i,k-\frac{1}{2})}) - \frac{1}{24}(v^{n}_{z(i,k+\frac{3}{2})} - v^{n}_{z(i,k-\frac{3}{2})})\right] - (\lambda+2\mu)\Psi^{n+\frac{1}{2}}_{xx(i,k)} - \lambda\Psi^{n+\frac{1}{2}}_{zz(i,k)} \\
\sigma^{n+\frac{1}{2}}_{zz(i,k)} =& \sigma^{n-\frac{1}{2}}_{zz(i,k)} - \frac{\Delta t(\lambda_{i,k}+2\mu_{i,k})}{\Delta z}\left[\frac{9}{8}(v^{n}_{z(i,k+\frac{1}{2})} - v^{n}_{z(i,k-\frac{1}{2})}) - \frac{1}{24}(v^{n}_{z(i,k+\frac{3}{2})} - v^{n}_{z(i,k-\frac{3}{2})})\right] \\
& - \frac{\Delta t\lambda_{i,k}}{\Delta x}\left[\frac{9}{8}(v^{n}_{x(i+\frac{1}{2},k)} - v^{n}_{x(i-\frac{1}{2},k)}) - \frac{1}{24}(v^{n}_{x(i+\frac{3}{2},k)} - v^{n}_{x(i-\frac{3}{2},k)})\right] - \lambda\Psi^{n+\frac{1}{2}}_{xx(i,k)} - (\lambda+2\mu)\Psi^{n+\frac{1}{2}}_{zz(i,k)} \\
\sigma^{n+\frac{1}{2}}_{xz(i+\frac{1}{2},k+\frac{1}{2})} =& \sigma^{n-\frac{1}{2}}_{zz(i+\frac{1}{2},k+\frac{1}{2})} - \frac{\Delta t\mu_{i+\frac{1}{2},k+\frac{1}{2}}}{\Delta z}\left[\frac{9}{8}(v^{n}_{x(i+\frac{1}{2},k+1} - v^{n}_{x(i+\frac{1}{2},k)}) - \frac{1}{24}(v^{n}_{x(i+\frac{1}{2},k+2)} - v^{n}_{z(i+\frac{1}{2},k-1)})\right] \\
& - \frac{\Delta t\mu_{i+\frac{1}{2},k+\frac{1}{2}}}{\Delta x}\left[\frac{9}{8}(v^{n}_{z(i+1,k+\frac{1}{2})} - v^{n}_{z(i,k+\frac{1}{2})}) - \frac{1}{24}(v^{n}_{z(i+2,k+\frac{1}{2})} - v^{n}_{z(i-1,k+\frac{1}{2})})\right] - \mu\Psi^{n+\frac{1}{2}}_{zx(i+\frac{1}{2},k+\frac{1}{2})} - \mu\Psi^{n+\frac{1}{2}}_{xz(i+\frac{1}{2},k+\frac{1}{2})}
\end{aligned}
\tag{3.14}
$$

Where the auxiliary variables are updating in the following form:

$$
\begin{aligned}
\Omega^{n}_{xx(i,k+\frac{1}{2})} =& c_x\Omega^{n-1}_{xx(i,k+\frac{1}{2})} + \frac{(1-c_x)}{\Delta x}\left[\frac{9}{8}(\sigma^{n-\frac{1}{2}}_{zx(i+1,k)} - \sigma^{n-\frac{1}{2}}_{zx(i,k)}) - \frac{1}{24}(\sigma^{n-\frac{1}{2}}_{xx(i+2,k)} - \sigma^{n-\frac{1}{2}}_{xx(i-1,k)})\right] \\
\Omega^{n}_{xz(i+\frac{1}{2},k)} =& c_z\Omega^{n-1}_{xz(i+\frac{1}{2},k)} + \frac{(1-c_z)}{\Delta z}\left[\frac{9}{8}(\sigma^{n-\frac{1}{2}}_{xz(i+\frac{1}{2},k+\frac{1}{2})} - \sigma^{n-\frac{1}{2}}_{xz(i+\frac{1}{2},k-\frac{1}{2})}) - \frac{1}{24}(\sigma^{n-\frac{1}{2}}_{xz(i+\frac{1}{2},k+\frac{3}{2})} - \sigma^{n-\frac{1}{2}}_{xz(i+\frac{1}{2},k-\frac{3}{2})})\right] \\
\Omega^{n}_{zx(i,k+\frac{1}{2})} =& c_x\Omega^{n-1}_{zx(i,k+\frac{1}{2})} + \frac{(1-c_x)}{\Delta x}\left[\frac{9}{8}(\sigma^{n-\frac{1}{2}}_{xz(i+\frac{1}{2},k+\frac{1}{2})} - \sigma^{n-\frac{1}{2}}_{xz(i-\frac{1}{2},k+\frac{1}{2})}) - \frac{1}{24}(\sigma^{n-\frac{1}{2}}_{xz(i+\frac{3}{2},k+\frac{1}{2})} - \sigma^{n-\frac{1}{2}}_{xz(i-\frac{3}{2},k+\frac{1}{2})})\right] \\
\Omega^{n}_{zz(i,k+\frac{1}{2})} =& c_z\Omega^{n-1}_{zz(i,k+\frac{1}{2})} + \frac{(1-c_z)}{\Delta z}\left[\frac{9}{8}(\sigma^{n-\frac{1}{2}}_{zz(i,k+1)} - \sigma^{n-\frac{1}{2}}_{zz(i,k)}) - \frac{1}{24}(\sigma^{n-\frac{1}{2}}_{zz(i,k+2)} - \sigma^{n-\frac{1}{2}}_{zz(i,k-1)})\right] \\
\Psi^{n+\frac{1}{2}}_{xx(i,k)} =& c_x\Psi^{n-\frac{1}{2}}_{xx(i,k)} + \frac{(1-c_x)}{\Delta x}\left[\frac{9}{8}(v^{n-1}_{x(i+\frac{1}{2},k)} - v^{n-1}_{x(i-\frac{1}{2},k)}) - \frac{1}{24}(v^{n-1}_{x(i+\frac{3}{2},k)} - v^{n-1}_{x(i-\frac{3}{2},k)})\right] \\
\Psi^{n+\frac{1}{2}}_{xz(i+\frac{1}{2},k+\frac{1}{2})} =& c_z\Psi^{n-\frac{1}{2}}_{xz(i+\frac{1}{2},k+\frac{1}{2})} + \frac{(1-c_z)}{\Delta z}\left[\frac{9}{8}(v^{n-1}_{x(i+\frac{1}{2},k+1)} - v^{n-1}_{x(i+\frac{1}{2},k)}) - \frac{1}{24}(v^{n-1}_{x(i+\frac{1}{2},k+2)} - v^{n-1}_{x(i+\frac{1}{2},k-1)})\right] \\
\Psi^{n+\frac{1}{2}}_{zx(i+\frac{1}{2},k+\frac{1}{2})} =& c_x\Psi^{n-\frac{1}{2}}_{zx(i+\frac{1}{2},k+\frac{1}{2})} + \frac{(1-c_x)}{\Delta x}\left[\frac{9}{8}(v^{n-1}_{z(i+1,k+\frac{1}{2})} - v^{n-1}_{z(i,k+\frac{1}{2})}) - \frac{1}{24}(v^{n-1}_{z(i+2,k+\frac{1}{2})} - v^{n-1}_{z(i-1,k+\frac{1}{2})})\right] \\
\Psi^{n+\frac{1}{2}}_{zz(i,k)} =& c_z\Psi^{n-\frac{1}{2}}_{zz(i,k)} + \frac{(1-c_z)}{\Delta z}\left[\frac{9}{8}(v^{n-1}_{z(i,k+\frac{1}{2})} - v^{n-1}_{z(i,k-\frac{1}{2})}) - \frac{1}{24}(v^{n-1}_{z(i,k+\frac{3}{2})} - v^{n-1}_{z(i,k-\frac{3}{2})})\right]
\end{aligned}
\tag{3.15}
$$

Where

$$
\begin{aligned}
c_x =& e^{-d(x)\Delta t} \\
c_z =& e^{-d(z)\Delta t}
\end{aligned}
\tag{3.16}
$$

The coefficients functions $d(x)$ ans $d(z)$ are defined in equation 3.8.

3.2.4 Parameter averaging scheme and free-surface topography

The equations, for numerical modeling of elastic wave propagation presented in the previous section, are valid if the medium is homogeneous. When the medium is not homogeneous, we assume smoothly heterogeneous medium. In that case, a parameter averaging scheme is necessary to compute the velocities and stresses fields. We use the scheme proposed by [Moczo et al., 2002].

$$\frac{1}{\rho_{i+\frac{1}{2},k}} = \begin{cases} 0, & \text{if } \rho_{i,k} = 0 \text{ and } \rho_{i+1,k} = 0 \\ \frac{2}{\rho_{i,k}+\rho_{i+1,k}}, & \text{otherwise;} \end{cases} \tag{3.17}$$

$$\frac{1}{\rho_{i,k+\frac{1}{2}}} = \begin{cases} 0, & \text{if } \rho_{i,k} = 0 \text{ and } \rho_{i,k+1} = 0 \\ \frac{2}{\rho_{i,k}+\rho_{i,k+1}}, & \text{otherwise;} \end{cases} \tag{3.18}$$

$$\mu_{i+\frac{1}{2},k+\frac{1}{2}} = \begin{cases} \left[\frac{1}{4}\left(\frac{1}{\mu_{i,k}} + \frac{1}{\mu_{i+1,k}} + \frac{1}{\mu_{i,k+1}}\frac{1}{\mu_{i+1,k+1}}\right)\right]^{-1}, & \text{if } \mu_{i,k}\mu_{i+1,k}\mu_{i,k+1}\mu_{i+1,k+1} \neq 0 \\ 0, & \text{otherwise;} \end{cases} \tag{3.19}$$

This parameter averaging scheme introduces a fictitious layer above the surface in the Earth model (see Figure 3.3). In this fictitious layer, the free-surface condition is fulfill. Therefore, the scheme can be used to simulate Rayleigh waves including surface topography and internal discontinuities. This method is known as the improved vacuum formulation. According to [Zeng et al., 2012], a number of ppw higher than conventional modeling is required to generate accurate Rayleigh wave with no significant numerical dispersion. An insufficient ppw may incur in a delay in the simulated traces. In most their simulations, the ppw used was above 90.

3.2.5 Earthquake source

The Earthquake source from an explosive can be modeled as:

$$\begin{aligned} \varphi_{\sigma_{xx}} = \varphi_{\sigma_{zz}} = A_{src}, \\ \varphi_{v_x} = \varphi_{v_z} = \varphi_{\sigma_{xz}} = 0, \end{aligned} \tag{3.20}$$

Where A_{src} defines the amplitude and the wave shape of the source for the modeling. The wave shapes usually are derivatives of the Gaussian functions. In our simulations, we use the negative Ricker function, whose expression is presented below.

Figure 3.3 Definition of the conditions in the grid using the improved vacuum method.

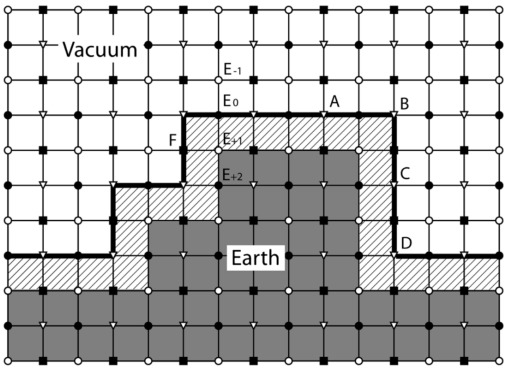

Source: [Zeng et al., 2012]).

$$A_{src} = -(1-2\pi^2 f^2 t^2)e^{-\pi^2 f^2 t^2} \tag{3.21}$$

Where f is the central frequency of the wavelet function. An illustration of the wave shape of this function is showed in Figure 3.4.

Figure 3.4 Wave shape of the source wavelet used in the simulations in this work. The wavelet is a Ricker function of central frequency of 15 [Hz]

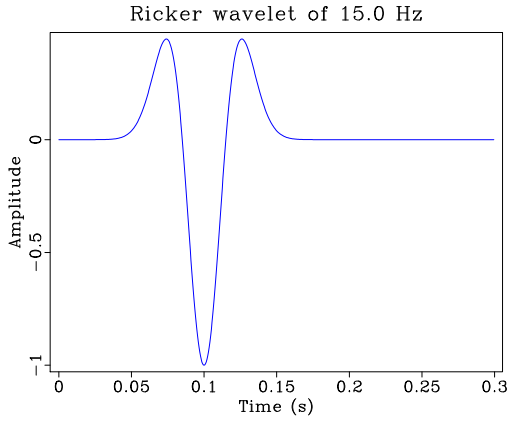

The source wavelet is commonly loaded as a discrete signal in the modeling. The stress source is injected by updating the normal stresses in the source location in the following form:

$$\begin{aligned} \sigma^n_{xx(Sx,Sz)} &= \sigma^n_{xx(Sx,Sz)} + \varphi_{\sigma_{xx}}[n], \\ \sigma^n_{zz(Sx,Sz)} &= \sigma^n_{zz(Sx,Sz)} + \varphi_{\sigma_{zz}}[n], \end{aligned} \tag{3.22}$$

Where Sx and Sz are the horizontal and vertical source location respectively.

3.2.6 Implementation

In the Figure 3.5, the flowchart for the implementation of the 2D finite difference elastic wave modeling is presented.

Figure 3.5 Flowchart illustrating the implementation of the 2D finite difference elastic wave modeling. The yellow boxes indicate the iterations of the spatial indices i and k.

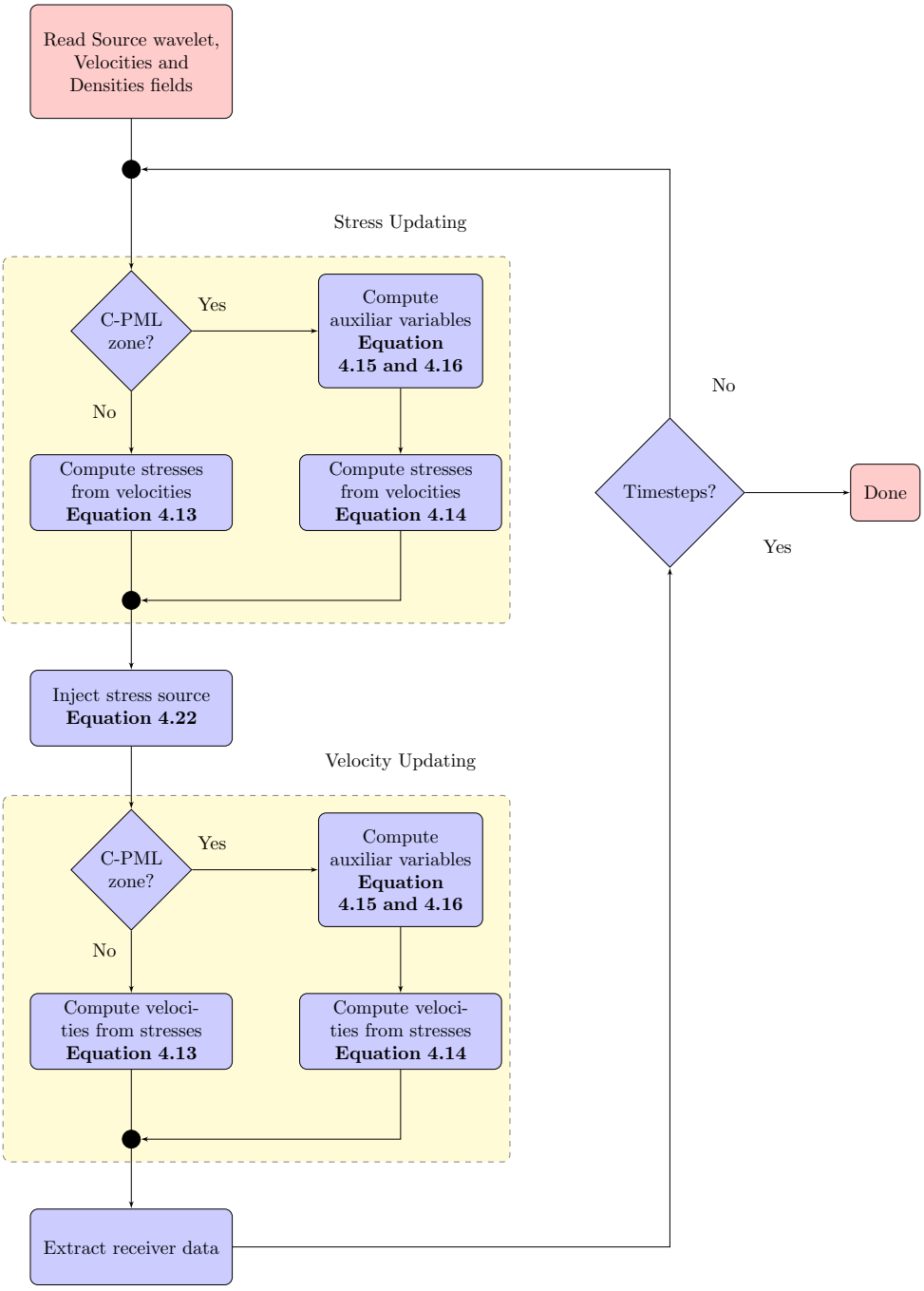

3.3 Numerical results

We test the numerical implementation of the 2D finite difference elastic wave modeling with four different experiments. Two experiments correspond to the Garvin's problem and the other two experiments correspond to the elastic/elastic problem. We compare the simulated traces with analytical traces by computing the mean square error (MSE) and the correlation between the two solutions.

3.3.1 Garvin's problem test

The Garvin's problem is used to study the propagation of P, S and Rayleigh waves in an infinite homogeneous and isotropic medium with free surface and an explosive source [Garvin, 1956]. We propose two experiments to probe the performance of the numerical implementation in this kind of problem. In the first experiment, a planar free-surface is considered, while in the second experiment an inclined free-surface In Figure 3.6 the two models proposed are showed.

Figure 3.6 Earth model used in the Garvin's problem test. The physical parameters of the medium are $V_P = 3000$ (m/s), $V_S = 1730$ (m/s) and $\rho = 2500$ (kg/m^3). R_1 and R_2 are receivers' location. a) Planar free-surface. b) Inclined free-surface.

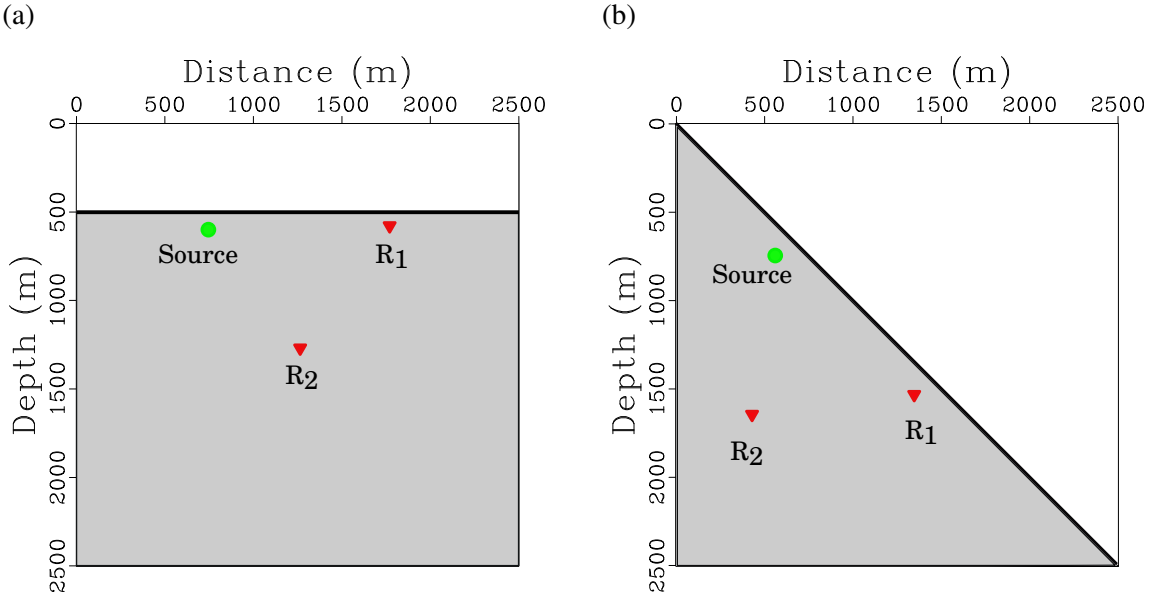

The numerical results for the two experiments of this problem are showed in Figures 3.7 and 3.8. The analytical solutions are computed with the code provided at http://www.spice-rtn.org/library/software/EX2DVAEL.html.

Figure 3.7 Numerical results for the Garvin's problem in the planar free-surface model in Figure 3.6a. MSE: Mean squared error, Corr: Correlation. 100 ppw. Source frequency=15 [Hz].

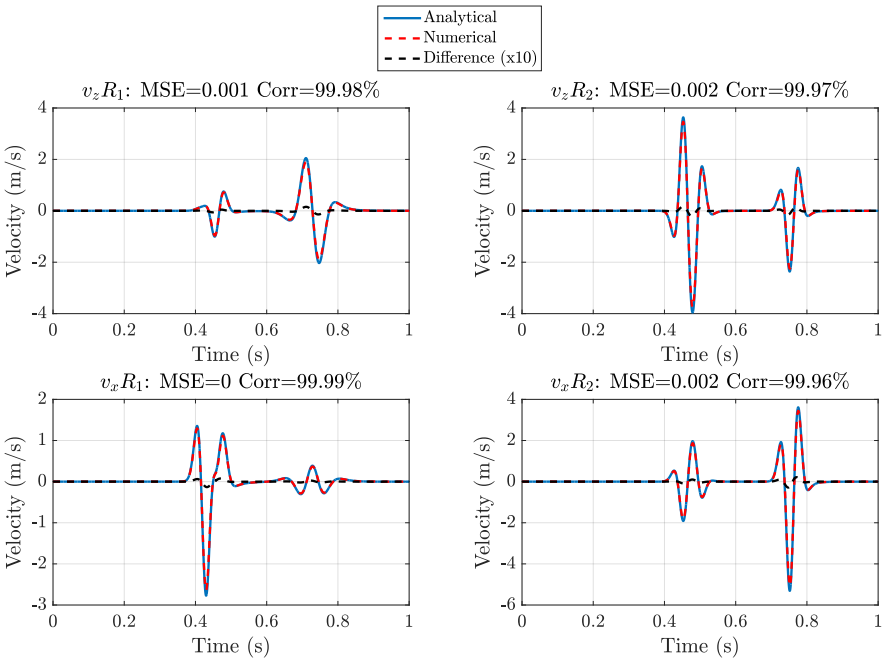

Figure 3.8 Numerical results for the Garvin's problem in the inclined free-surface model of Figure 3.9a. MSE: Mean squared error, Corr: Correlation. 100 ppw. Source frequency=15 [Hz].

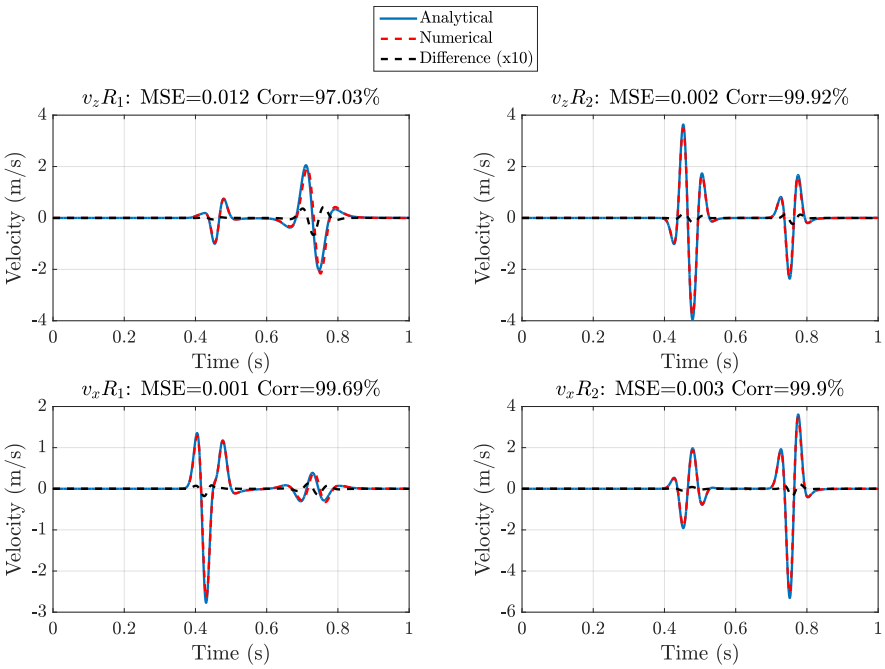

For the numerical results in the Figure 3.8 the simulated traces via finite differences are rotated by the same dip angle to match the flat case, so the two cases, planar and inclined, can be directly compared.

3.3.2 Elastic/elastic problem test

The elastic/elastic problem is used to study the propagation of P and S waves in an interface between two infinite homogeneous and isotropic media with an explosive source [Berg et al., 1994]. We propose two experiments to probe the performance of the numerical implementation in this kind of problem. In the first experiment, we consider a planar interface, while in the second experiment an inclined interface is considered. In Figure 3.9 the two proposed models are shown.

Figure 3.9 Earth model used in the elastic/elastic problem. In the top layer $V_P = 3000$ (m/s), $V_S = 1500$ (m/s) and $\rho = 2500$ (kg/m^3). In the bottom layer $V_P = 5000$ (m/s), $V_S = 2250$ (m/s) and $\rho = 2750$ (kg/m^3). R_1 and R_2 are receivers' location. a) Planar interface. b) Inclined interface.

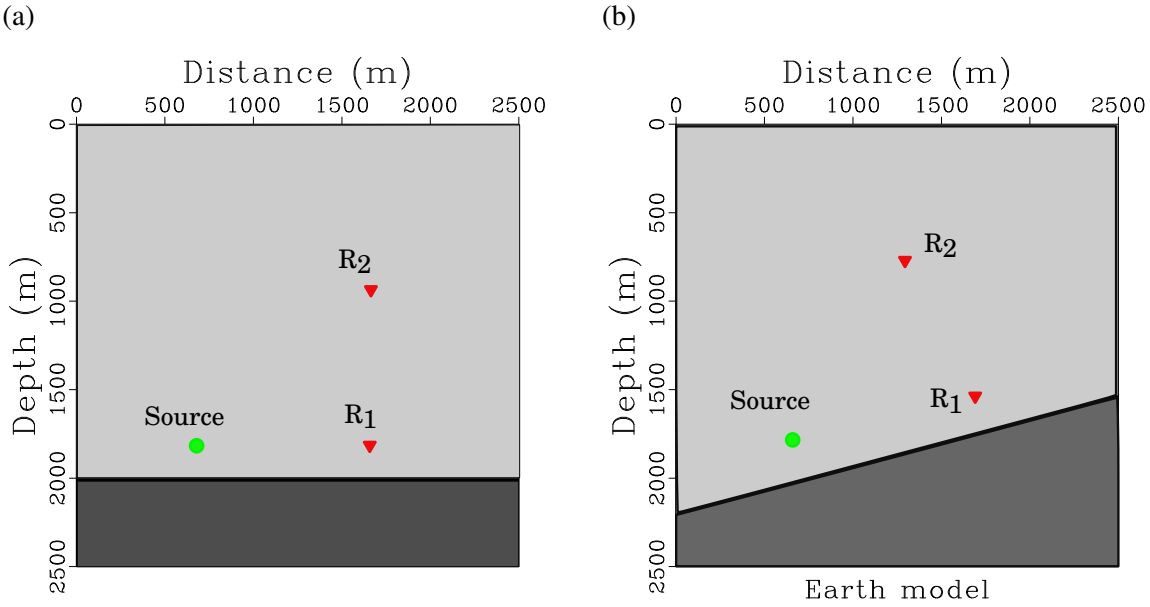

The numerical results for the two experiments of this problem are showed in Figures 3.10 and 3.11. The analytical solutions are computed with the code provided at http://www.spice-rtn.org/library/software/EX2DELEL.html. In the same way that in the Garvin's problem, The numerical results in the Figure 3.11 the simulated traces via finite differences are rotated by the same dip angle to match the flat case, so the two cases, planar and inclined, can be directly compared.

Figure 3.10 Numerical results for the elastic/elastic problem in the planar interface model of Figure 3.9a. MSE: Mean squared error, Corr: Correlation. 100 ppw. Source frequency=15 [Hz].

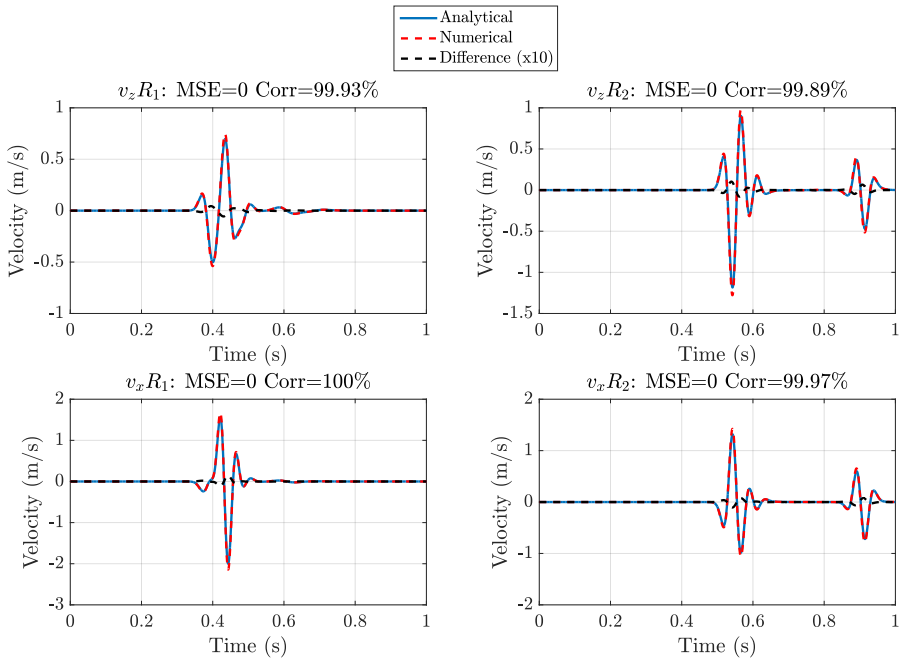

Figure 3.11 Numerical results for the elastic/elastic problem in the inclined interface model of Figure 3.9b. MSE: Mean squared error, Corr: Correlation. 100 ppw. Source frequency=15 [Hz].

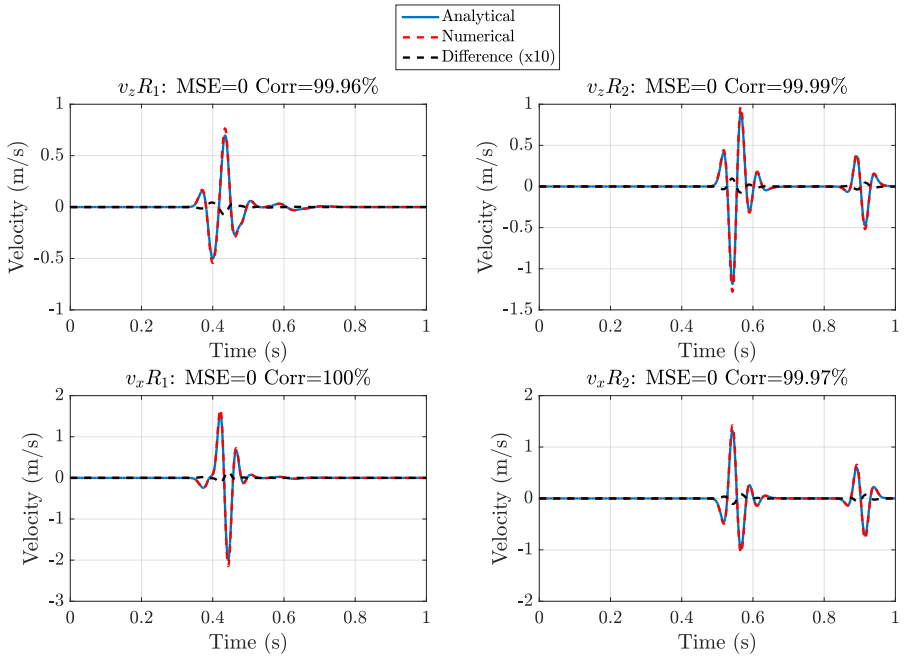

3.3.3 Seismic wave propagation

As it was mentioned in the introduction of this chapter, seismic wave propagation can be studied as an elastic wave propagation. So, an example of seismic wave propagation using the numerical implementation of 2D finite differences elastic wave propagation is given below. For this example, we have created the velocity model with free-surface planar and two layers (see Figure 3.12). For this example, we use the Ricker wavelet source with central frequency of 30 (Hz). The source has been located in 10 m of depth and 200 m of horizontal distance. The receivers are located on the surface with 10 m of depth, with 1 m space intervals, and from 200 to 1800 m of horizontal distance. In this simulation, we use 32 ppw.

Figure 3.12 Earth model. Macro-model parameters for the top layer: $V_P = 1800$ (m/s), $V_S = 1000$ (m/s) and $\rho = 1750$ (kg/m^3) and the bottom layer: $V_P = 3000$ (m/s), $V_S = 1500$ (m/s) and $\rho = 2250$ (kg/m^3).

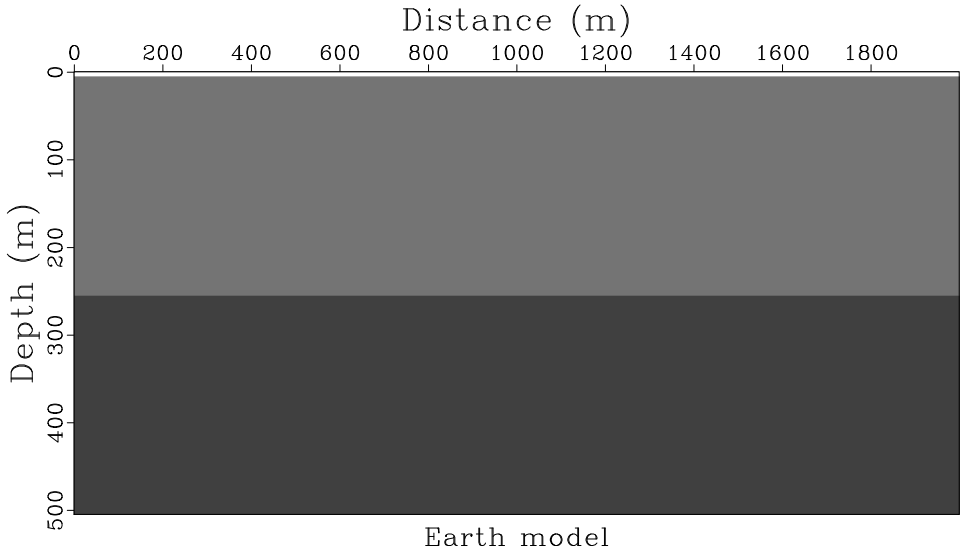

In Figure 3.13, the different types of seismic waves that are propagated in the proposed medium, are observed. It is possible to identify compressional body waves (P direct, P-transmission, P-refraction, P-P reflection, P-multiple), shear body waves (S-transmission, S-S reflection), converted body waves (P-S reflection, P-S transmission, S-P transmission) and surface waves (Rayleigh waves). Some of these wave types can also be identified in the shot gathers of Figure 3.14. The transmitted waves cannot be registered by receivers because they are on the surface.

Figure 3.13 Seismic waves propagation in a medium with planar free-surface and two layers. a) $t = 0.16$ [s]. b) $t = 0.24$ [s]. c) $t = 0.4$ [s]. d) $t = 0.6$ [s].

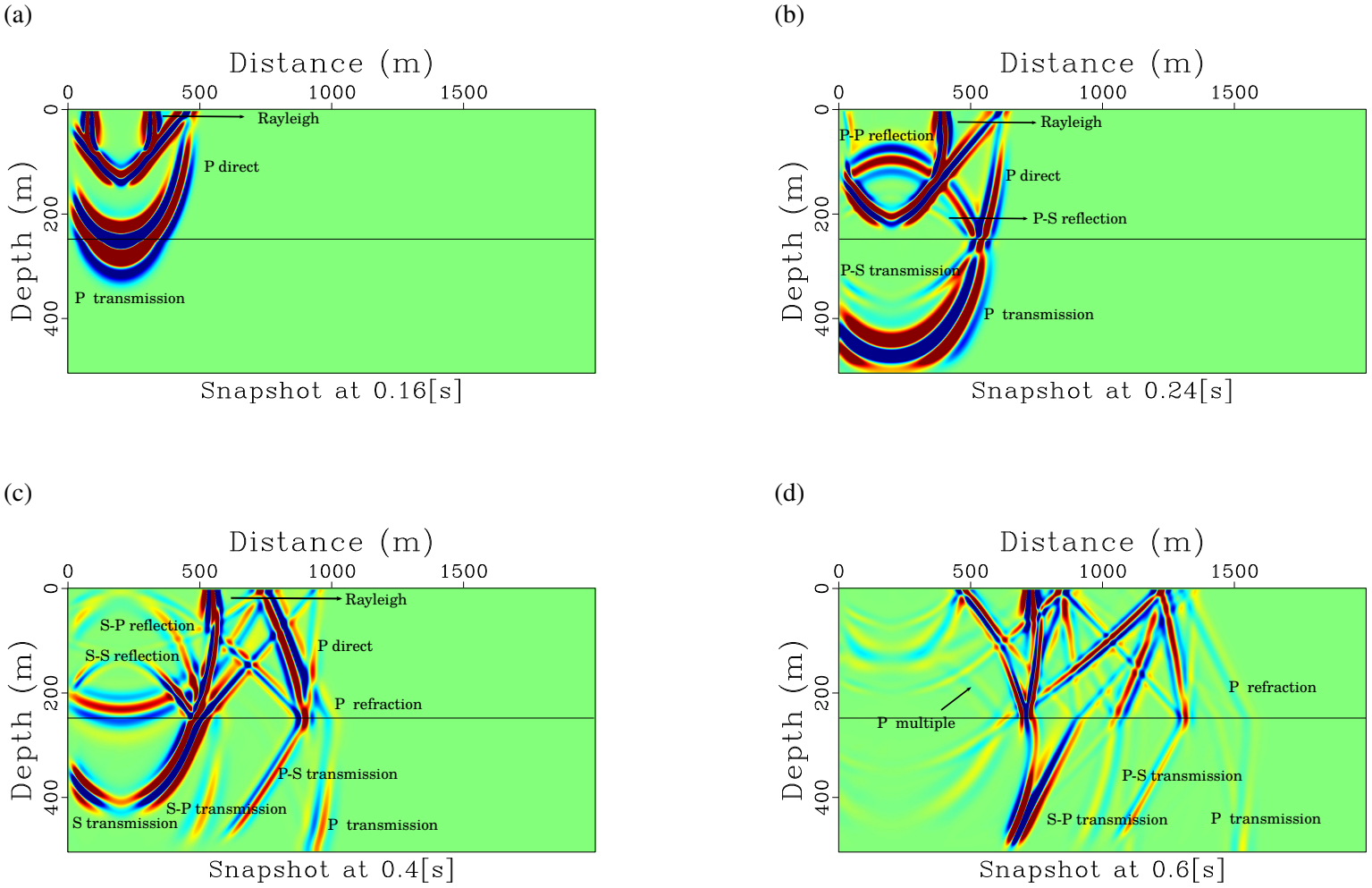

Figure 3.14 Seismic data from model of Figure 3.12. a) Horizontal shot gather. b) Vertical shot gather.

(a) (b)

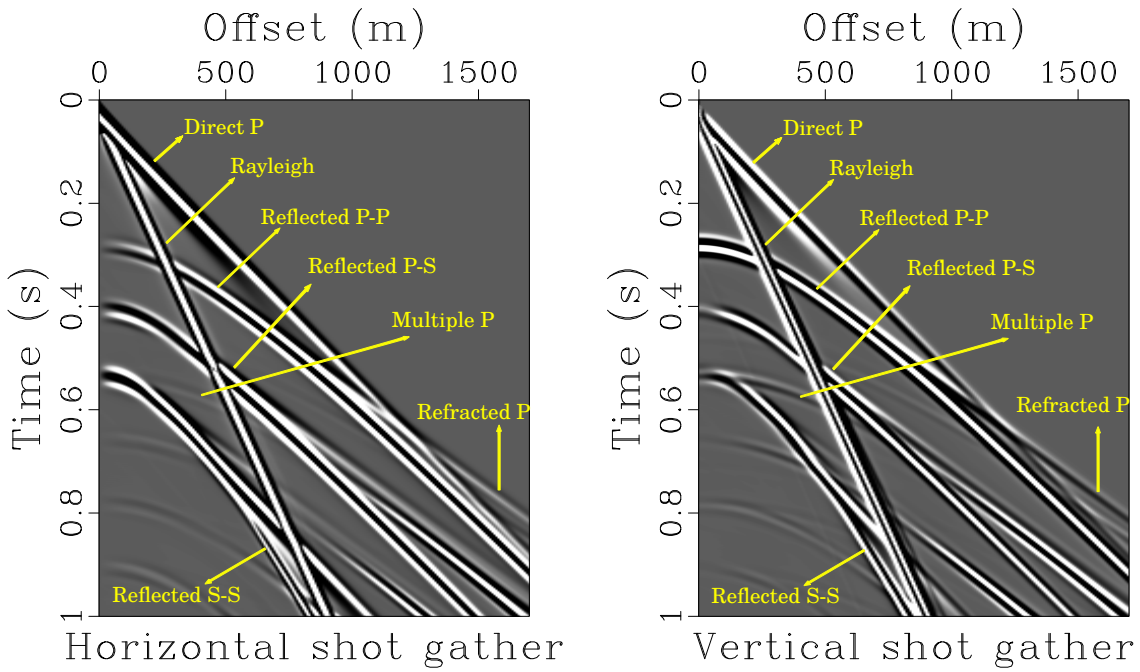

3.4 Conclusions

A 2D finite differences method with second order accuracy in time and fourth order accuracy in space was implemented to model elastic wave propagation in presence of free-surface topography. The parameter averaging scheme allowed the fulfillment of the free traction condition in the surface topography. For modeling, C-PML was used to ensure non-reflective boundaries in the computational domain. The implementation was tested by comparing analytical and numerical solutions for Garvin's problem and (with inclined and planar free-surface) elastic/elastic problem (with inclined and planar interface). The numerical results showed the performance of the algorithm implemented where the correlation between numerical and analytical seismograms were higher than 99% for most simulation tests.

Chapter 4

Surface waves propagation under irregular near-surface

Abstract

Surface waves propagation is a complex process that involves different types of waves, including Rayleigh waves, higher modes and scattering. The complexity of the propagation depends on the velocity variations and geometry of the near-surface. Synthetic seismograms are obtained from different velocity models, including surface topography and irregular bedrock. A qualitative analysis from seismic attributes is performed in order to find a relationship between seismograms and velocity models. Our results exhibit the strong dependence of the moveout of the surface waves on the near-surface geometry and composition, in addition to show the relevance of the seismic attributes to enhance the surface waves properties.

4.1 Introduction

The near-surface is the space that correspond to the first meters below the free surface. According to [Yilmaz, 2015], It is composed of a soil column and low-velocity, unconsolidated, heterogeneous, and weathered layers of rock. The complexity of the near-surface composition is the cause by which surface waves propagation is so complicated. Dispersion, scattering and attenuation of surface waves are some of the phenomena produced by the realistic near-surface. Several synthetic experiments have been performed in order to study how the near-surface geometry and composition affect the surface waves propagation. The scattering of surface waves was studied by [Gilbert and Knopoff, 1960], [Hudson and Knopoff, 1967], [Martel et al., 1977], [Levander, 1990] and [Almuhaidib and Toksöz, 2014]. These

authors found different types of scattering: body wave scattering, surface wave scattering, body-to-surface, and surface-to-body wave scattering. The dispersion of Rayleigh waves is highly studied by [Yilmaz, 2015] who found that the dispersion characteristics of Rayleigh waves are greatly influenced by the geometry of and lateral heterogeneities within the soil column. Even with all the experiments performed, it is still difficult to fully describe the surface waves propagation from seismic data. For that reason, it is necessary to analyze the behavior of the seismic records via seismic attributes that can enhance the information of the surface waves propagation under irregular near-surface.

In this chapter, the results of different synthetic experiments of surface waves propagation through earth models with irregular near-surface are presented. In each experiment, seismic data are acquired and later seismic attributes are computed from the seismograms. From our simulation results, it is shown that the moveout of surface waves is strongly affected by the surface topography, the soil-column and the irregular bedrock. Similarly, The Rayleigh wave dispersion is highly related to the thickness of the soil-column layer and surface waves scattering is strongly depending on thickness variations of the soil-column. Moreover, the computed seismic attributes from the synthetic data enhanced the surface wave properties. Therefore, the higher modes, scattering and backscattering of surface waves were identified by the seismic attributes.

4.2 Synthetic examples

In total, thirteen simulations of seismic wave propagation experiments were performed, which are organized in four different types of experiments. The description of each type of experiment is presented below. For each example, the earth model, the acquired shot gathers and the computed seismic attributes are showed.

4.2.1 Irregular topography effect

Three examples of seismic waves propagation with earth models including irregular topography are proposed (Example 1.1, 1.2 and 1.3). The topography is described by a sinusoidal function where the amplitude and the period depend on the Rayleigh wavelength λ_R. For each example, a different value of period in the sinusoidal topography is used. The periods are $20\lambda_R$, $10\lambda_R$ and $4\lambda_R$. From the results of these examples, it is possible to observe that the irregular topography may affect the moveout of the Rayleigh wave. Additionally, Scattering energy is produced when the surface topography is described by strong variations. In general, the higher variations in the surface topography, the higher scattered energy.

4.2.2 Soil-column effect

The soil-column is the most superficial layer in the earth models. This layer is characterized by its low velocity and its low thickness. Three examples of seismic waves propagation with earth models including the soil-column layer are proposed (Example 2.1, 2.2 and 2.3). In these examples the soil-column is a homogeneous layer with velocities and densities lower than the deeper layer. For each example, a different value of thickness of the soil-column is used. The thicknesses are 5 m, 10 m and 20 m. From the results of these examples, it is possible to observe that the soil-column layer affects strongly the Rayleigh wave propagation. When the soil-column is thin, the Rayleigh waves become dispersive and higher modes are generated. In general, the thinner soil-column layer, the higher Rayleigh waves dispersion.

4.2.3 Irregular bedrock effect

The bedrock is the lithified rock that lies under the soil column layer. It is characterized for having velocities higher than the soil-column layer. Three examples of seismic waves propagation with earth models including irregular bedrock are proposed (Example 3.1, 3.2 and 3.3). In these examples, the bedrock is a homogeneous layer where the contact interface with the soil-column is a sinusoidal function which the amplitude and period depend on Rayleigh wavelength λ_R. For each example, a different value of period in the sinusoidal topography is used. The periods are $10\lambda_R$, $4\lambda_R$ and $2\lambda_R$. From the results of these examples, it is possible to observe that the smooth bedrock affects the moveout of the Rayleigh wave whilst the rugged bedrock produces strong surface-waves scattering and backscattering. In general, the greater roughness bedrock, the higher scattered and backscattered energy.

4.2.4 Effect of soil-column with irregular topography

In the previous examples, the effect of soil-column thickness and the effect of irregular topography over the surface waves propagation are shown. Now, the combination of these two effects are considered. Four examples of seismic waves propagation with earth models including soil-column with irregular topography are proposed (Example 4.1, 4.2, 4.3 and 4.4). In the three first examples, the irregular topography is sinusoidal function which the amplitude and period depend on Rayleigh wavelength λ_R. The periods are $10\lambda_R$, $4\lambda_R$ and $2\lambda_R$. In the fourth example, the irregular topography is a gaussian hill with amplitude $2.6\lambda_R$ and variance $1.3\lambda_R$. From the results of these examples, it is possible to observe that the smooth topography affects the moveout of the Rayleigh wave whilst the rugged topography produces strong surface-waves scattering and backscattering. In general, the greater roughness surface topography, the higher scattered and backscattered energy.

Example 1.1

For this example, we have built the velocity model showed in Figure 4.1. The topography is a sinusoid with amplitude λ_R and period $20\lambda_R$. The source function is a Ricker wavelet with central frequency of 30 (Hz). The source has been located in 7.5 m of depth and 100 m of horizontal distance. The receivers are located on the surface with 0.1 m of depth, with 1 m space intervals, and from 0 to 150 m of horizontal distance from the source. In this simulation, we use a 70 ppw Rayleigh. The recorded data are presented in Figure 4.2.

Figure 4.1 Earth model with surface topography. In the model $V_P = 1800$ (m/s), $V_S = 300$ (m/s) and $\rho = 1500$ (kg/m). The topography is a sinusoid with amplitude λ_R and period $20\lambda_R$.

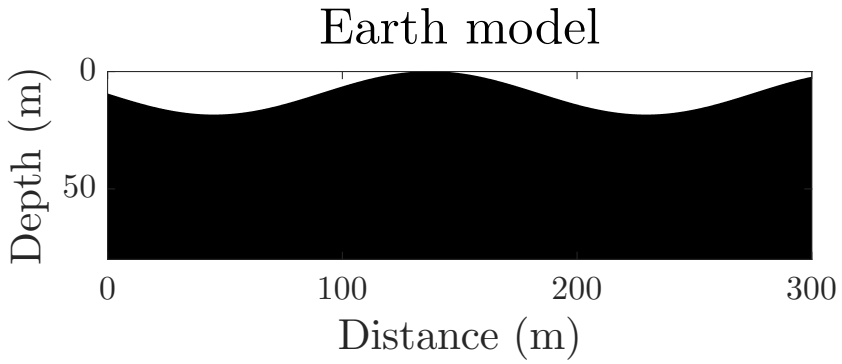

Figure 4.2 Vertical and horizontal shot gathers obtained from the model in Figure 4.1.

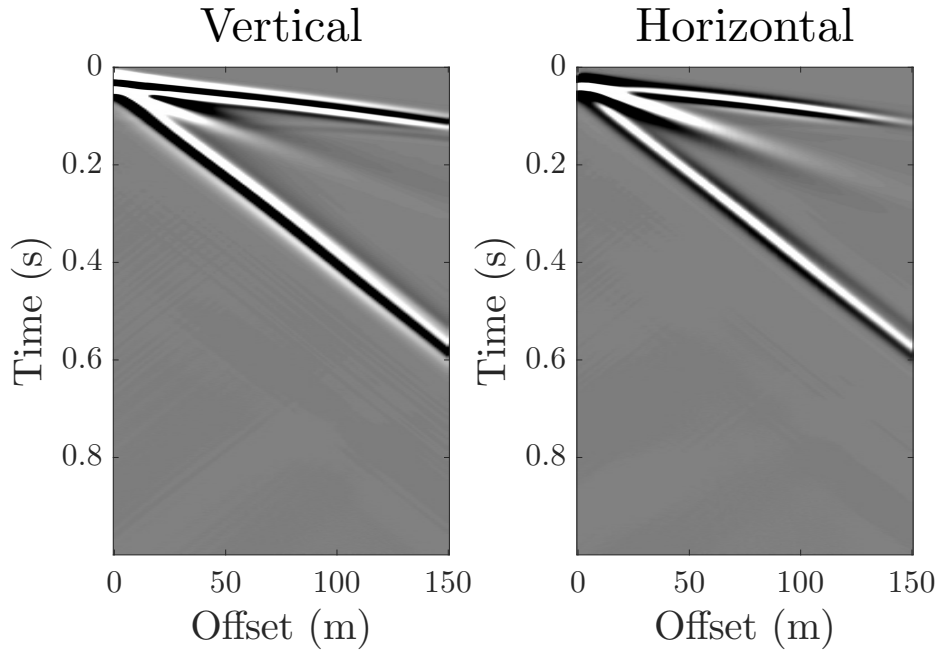

The Figure 4.3 shows the seismic attributes computed from seismic data in Figure 4.2. It is possible to identify the values of the seismic attributes in both the direct body waves and the Rayleigh waves. The Rayleigh wave behavior is similar to the earth model with planar surface, so it is not affected by the proposed topography in this example.

Figure 4.3 Seismic attributes computed from shot gathers in Figure 4.2. The attributes are computed with a time window of 0.4 seconds of duration.

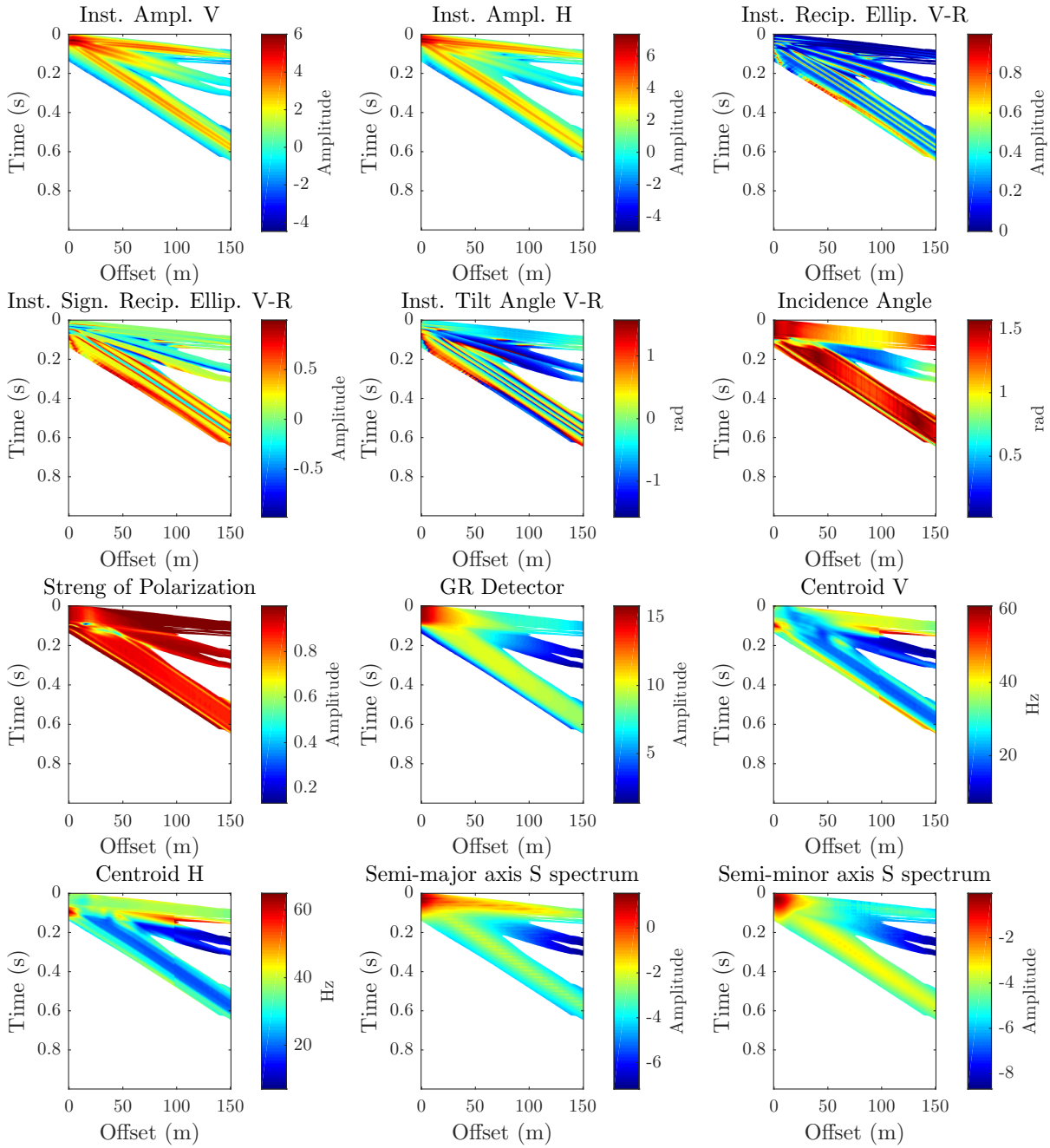

Example 1.2

For this example, we have built the velocity model showed in Figure 4.4. The topography is a sinusoid with amplitude $0.5\lambda_R$ and period $10\lambda_R$. The source function is a Ricker wavelet with central frequency of 30 (Hz). The source has been located in 7.5 m of depth and 100 m of horizontal distance. The receivers are located on the surface with 0.1 m of depth, with 1 m space intervals, and from 0 to 150 m of horizontal distance from the source. In this simulation, we use a 70 ppw Rayleigh. The recorded data are presented in Figure 4.5.

Figure 4.4 Earth model with surface topography. In the model $V_P = 1800$ (m/s), $V_S = 300$ (m/s) and $\rho = 1500$ (kg/m). The topography is in a sinusoid with amplitude $0.5\lambda_R$ and period $10\lambda_R$.

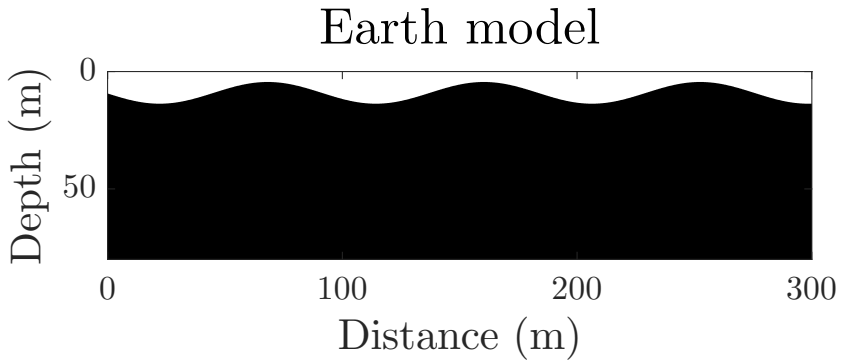

Figure 4.5 Vertical and horizontal shot gathers obtained from the model in Figure 4.4.

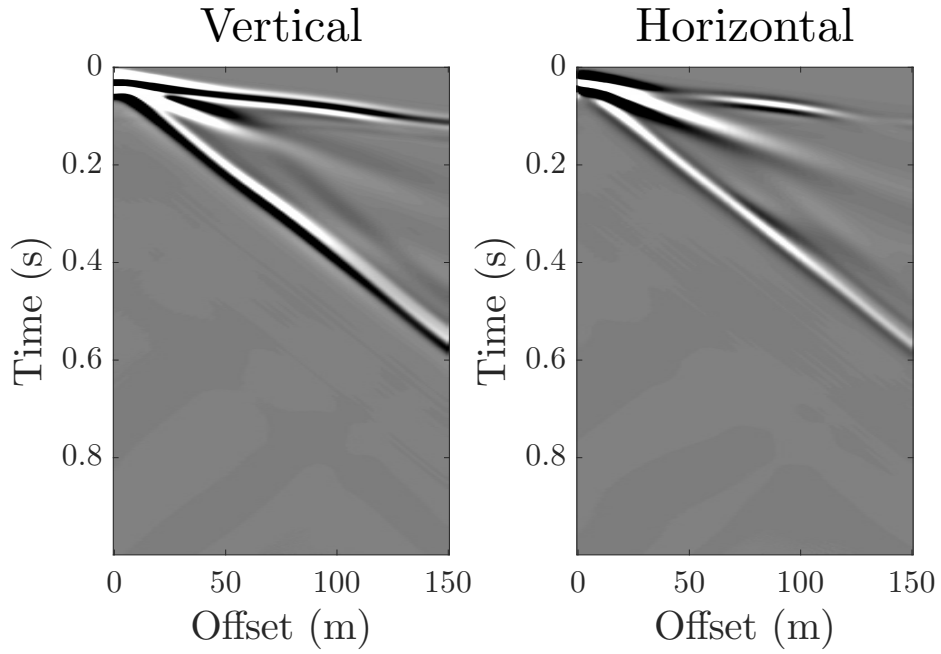

The Figure 4.6 shows the seismic attributes computed from seismic data in Figure 4.5. It is possible to identify the values of the seismic attributes in both the direct body waves and the Rayleigh waves. The Rayleigh wave behavior is similar to the earth model with planar surface, so it is not affected by the proposed topography in this example.

Figure 4.6 Seismic attributes computed from shot gathers in Figure 4.5. The attributes are computed with a time window of 0.4 seconds of duration.

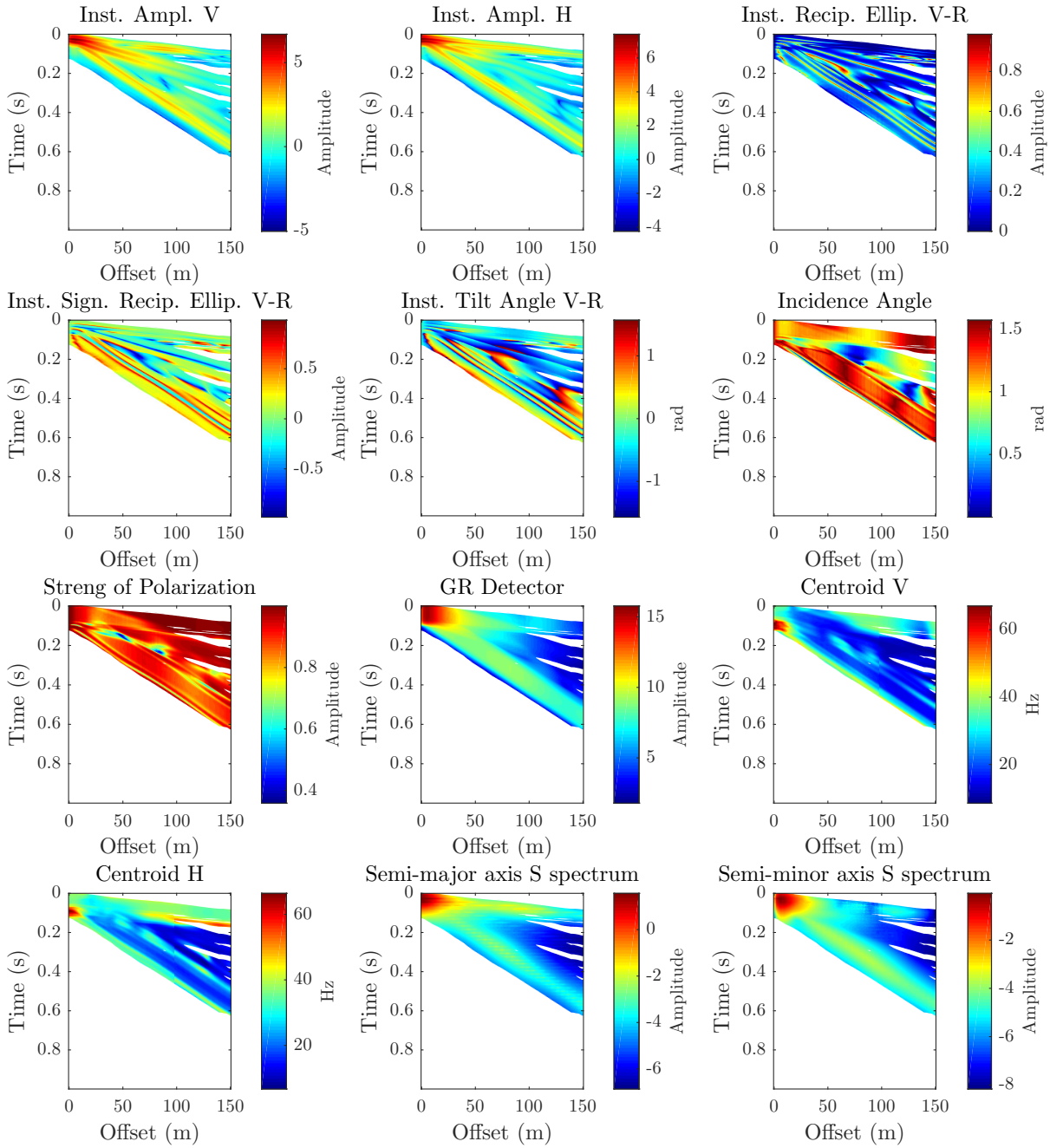

Example 1.3

For this example, we have built the velocity model showed in Figure 4.7. The topography is a sinusoid with amplitude $0.5\lambda_R$ and period $4\lambda_R$. The source function is a Ricker wavelet with central frequency of 30 (Hz). The source has been located in 7.5 m of depth and 100 m of horizontal distance. The receivers are located on the surface with 0.1 m of depth, with 1 m space intervals, and from 0 to 150 m of horizontal distance from the source. In this simulation, we use a 70 ppw Rayleigh. The recorded data are presented in Figure 4.8.

Figure 4.7 Earth model with surface topography. In the model $V_P = 1800$ (m/s), $V_S = 300$ (m/s) and $\rho = 1500$ (kg/m). The topography is a sinusoid with amplitude $0.5\lambda_R$ and period $4\lambda_R$.

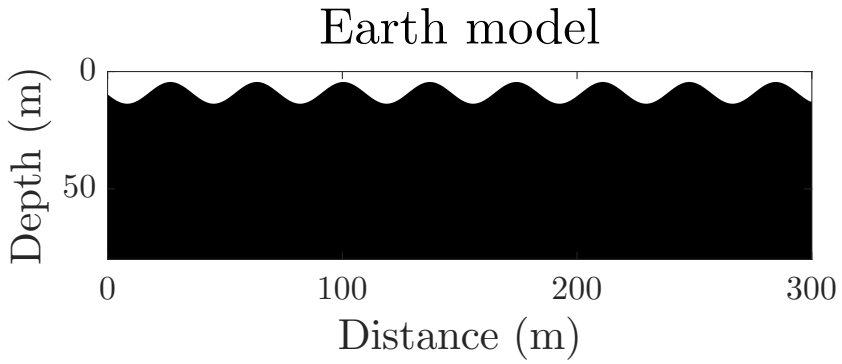

Figure 4.8 Vertical and horizontal shot gathers obtained from the model in Figure 4.7.

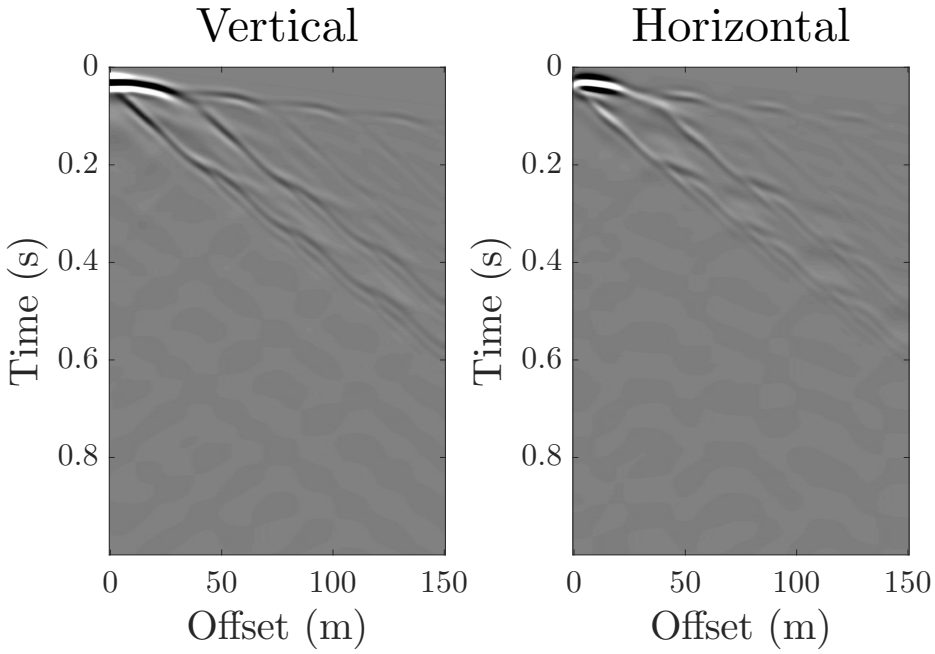

The Figure 4.9 shows the seismic attributes computed from seismic data in Figure 4.8. It is possible to identify the values of the seismic attributes in both the direct body waves and the Rayleigh waves. The Rayleigh wave behavior is similar to the earth model with planar surface, so it is not affected by the proposed topography in this example.

Figure 4.9 Seismic attributes computed from shot gathers in Figure 4.8. The attributes are computed with a time window of 0.4 seconds of duration.

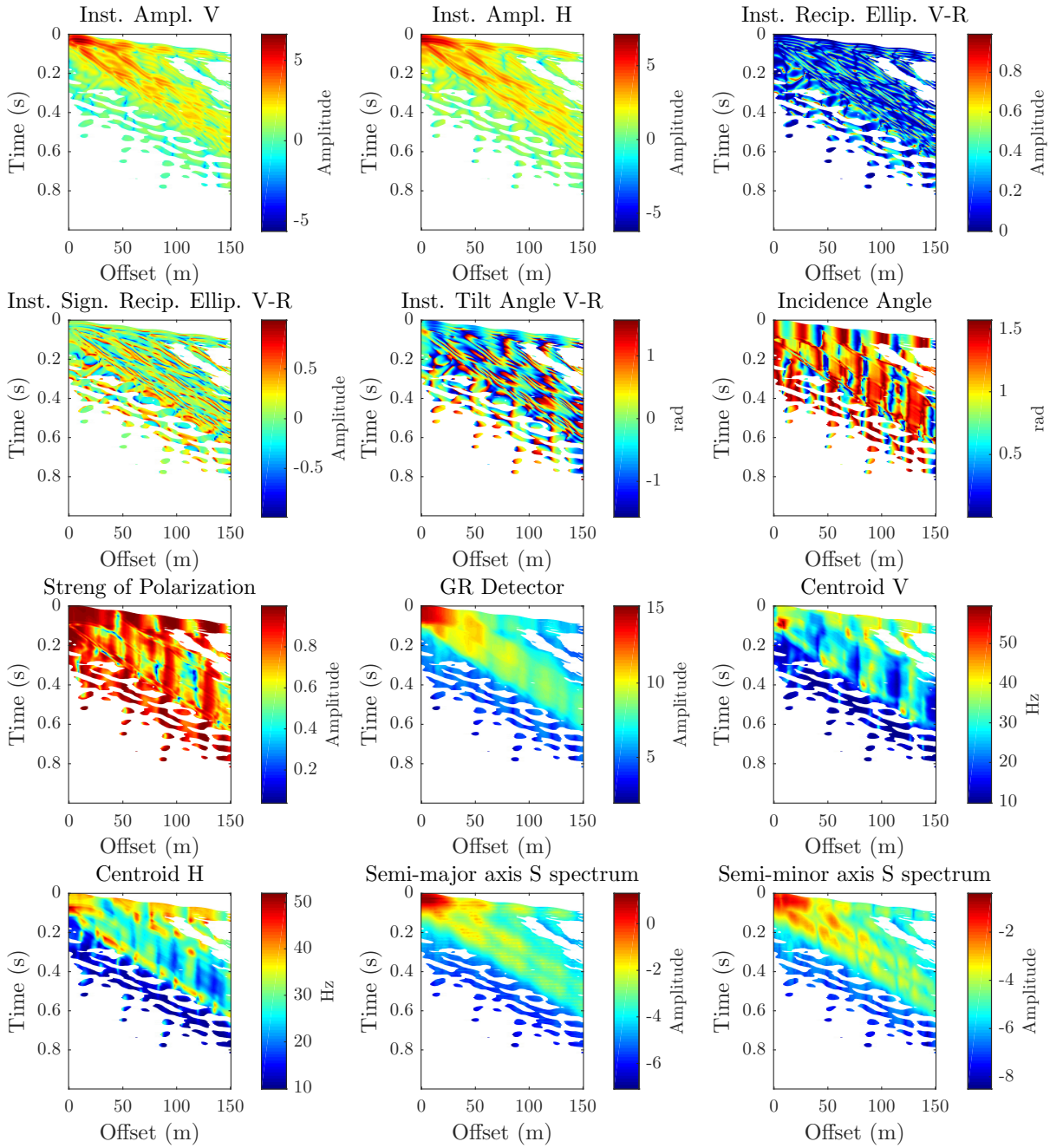

Example 2.1

For this example, we have built the velocity model showed in Figure 4.10. The thickness of the soil-column is 5 m. The source function is a Ricker wavelet with central frequency of 30 (Hz). The source has been located in 7.5 m of depth and 100 m of horizontal distance. The receivers are located on the surface with 0.1 m of depth, with 1 m space intervals, and from 0 to 150 m of horizontal distance from the source. In this simulation, we use a 70 ppw Rayleigh. The recorded data are presented in Figure 4.11.

Figure 4.10 Earth model with soil-column. In the top layer $V_P = 1800$ (m/s), $V_S = 300$ (m/s) and $\rho = 1500$ (kg/m^3). In the bottom layer $V_P = 2000$ (m/s), $V_S = 600$ (m/s) and $\rho = 2000$ (kg/m^3). The thickness of the soil-column is 5 m.

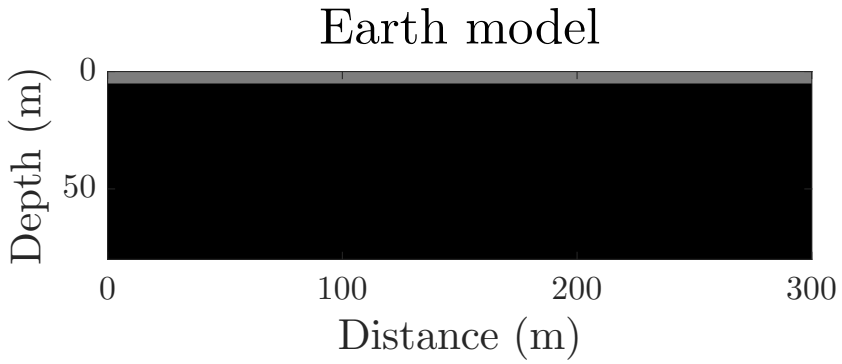

Figure 4.11 Vertical and horizontal shot gathers obtained from the model in Figure 4.10.

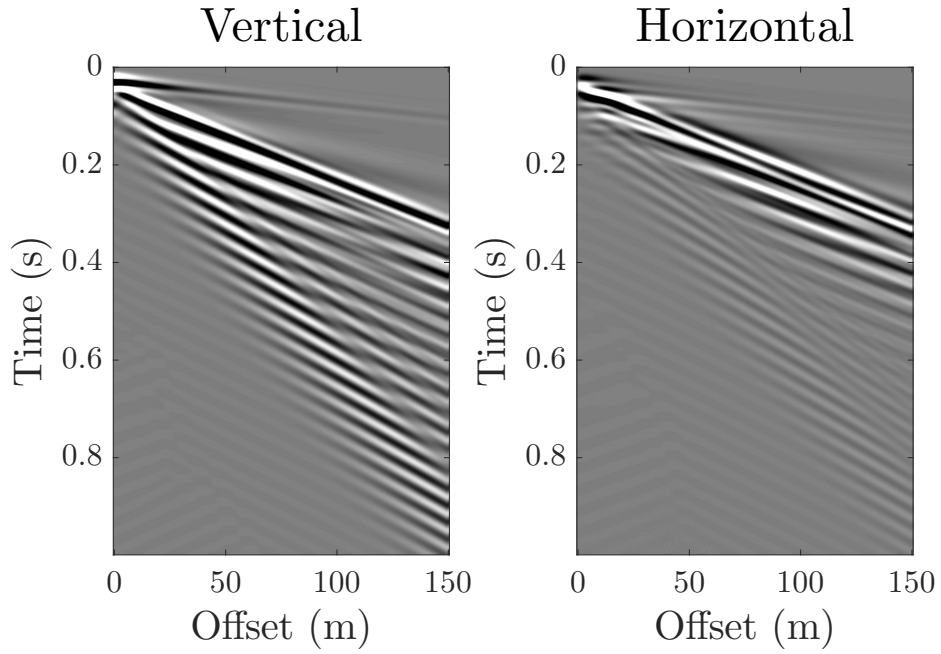

The Figure 4.12 shows the seismic attributes computed from seismic data in Figure 4.11. It is possible to identify the values of the seismic attributes in the direct body wave, the Rayleigh wave and the higher modes. In this example, the Rayleigh wave become highly dispersive because of the thickness of the soil-column.

Figure 4.12 Seismic attributes computed from shot gathers in Figure 4.11. The attributes are computed with a time window of 0.4 seconds of duration.

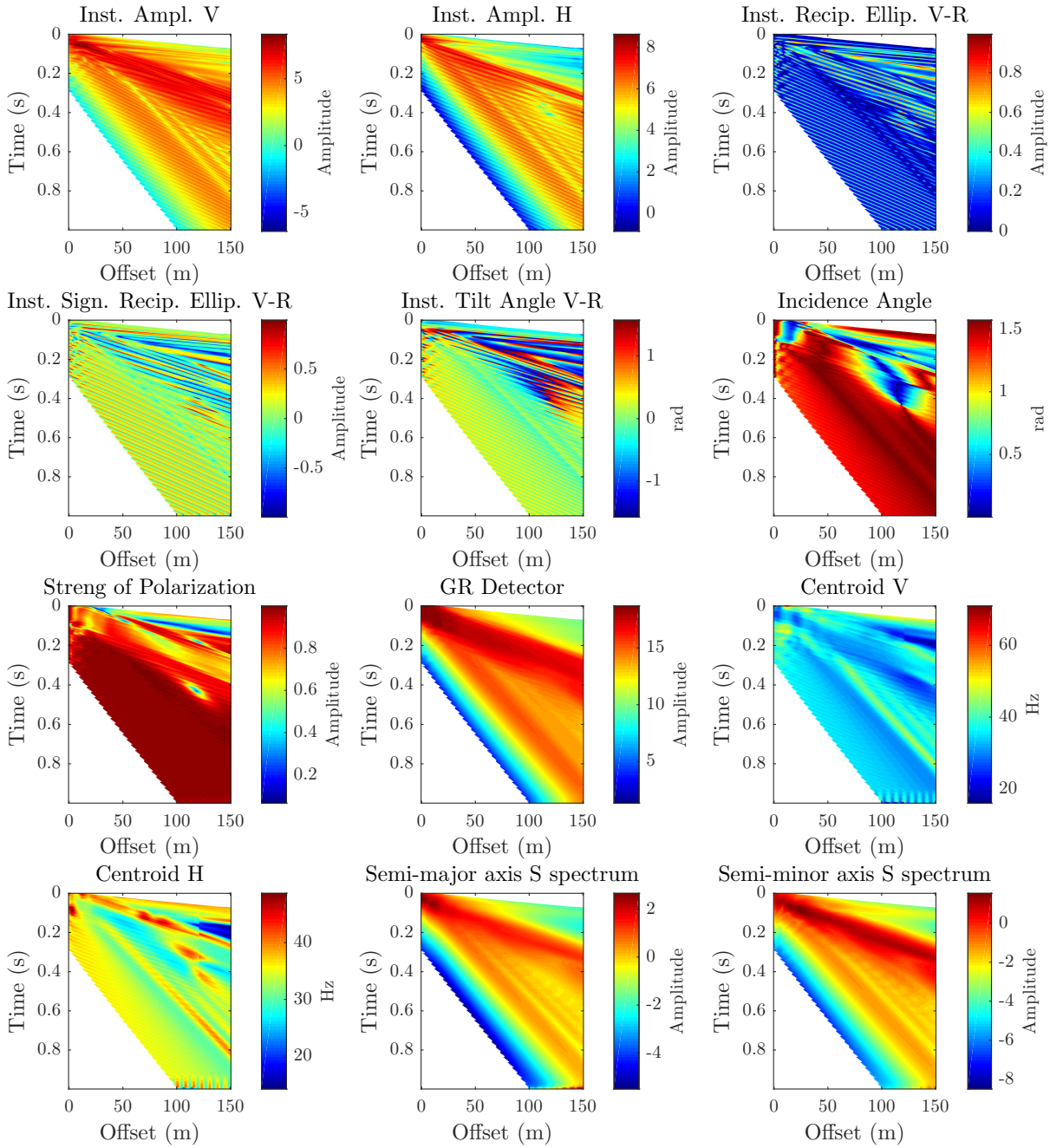

Example 2.2

For this example, we have built the velocity model showed in Figure 4.13. The thickness of the soil-column is 10 m. The source function is a Ricker wavelet with central frequency of 30 (Hz). The source has been located in 7.5 m of depth and 100 m of horizontal distance. The receivers are located on the surface with 0.1 m of depth, with 1 m space intervals, and from 0 to 150 m of horizontal distance from the source. In this simulation, we use a 70 ppw Rayleigh. The recorded data are presented in Figure 4.14.

Figure 4.13 Earth model with soil-column. In the top layer $V_P = 1800$ (m/s), $V_S = 300$ (m/s) and $\rho = 1500$ (kg/m^3). In the bottom layer $V_P = 2000$ (m/s), $V_S = 600$ (m/s) and $\rho = 2000$ (kg/m^3). The thickness of the soil-column is 10 m.

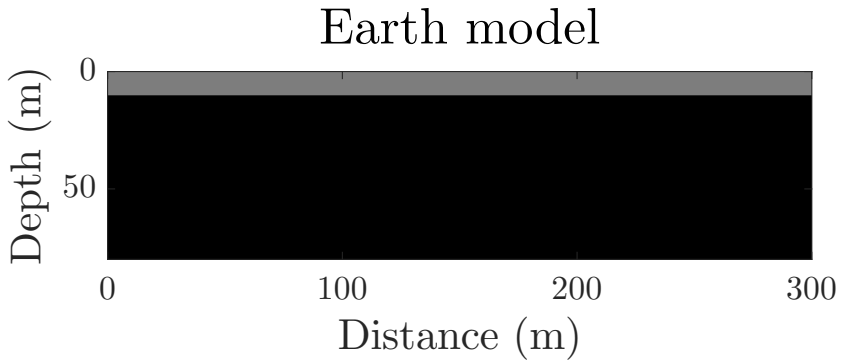

Figure 4.14 Vertical and horizontal shot gathers obtained from the model in Figure 4.13.

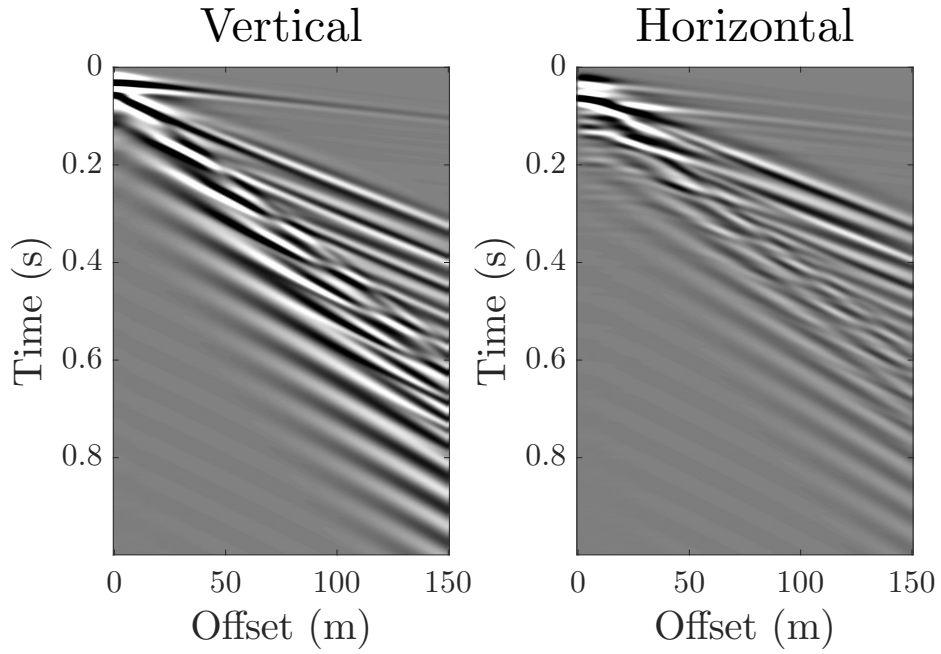

The Figure 4.15 shows the seismic attributes computed from seismic data in Figure 4.14. It is possible to identify the values of the seismic attributes in the direct body wave, the Rayleigh wave and the higher modes. In this example, the Rayleigh wave become less dispersive than in the previous example because the thickness of the soil-column is higher.

Figure 4.15 Seismic attributes computed from shot gathers in Figure 4.14. The attributes are computed with a time window of 0.4 seconds of duration.

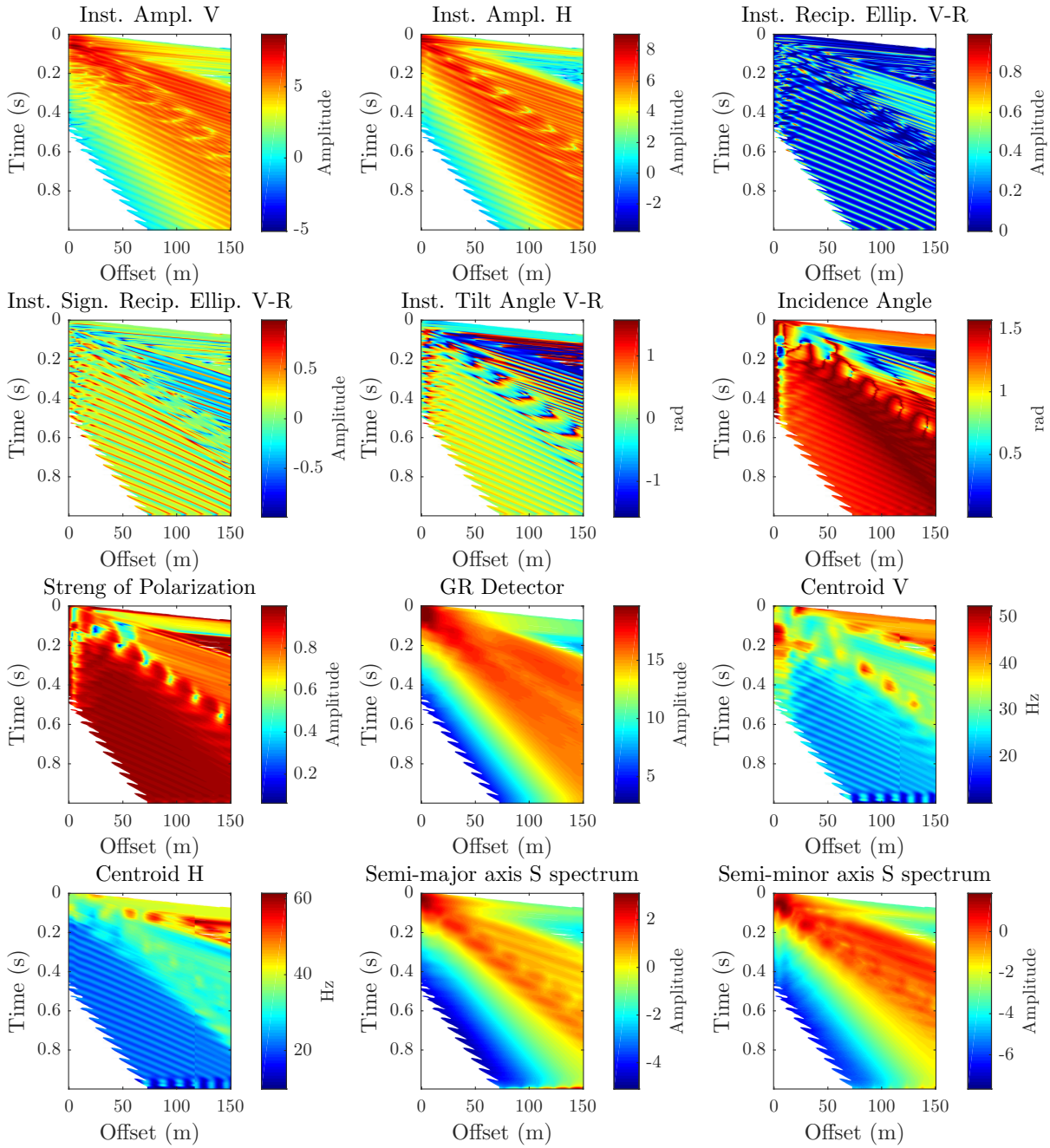

Example 2.3

For this example, we have built the velocity model showed in Figure 4.16. The thickness of the soil-column is 20 m. The source function is a Ricker wavelet with central frequency of 30 (Hz). The source has been located in 7.5 m of depth and 100 m of horizontal distance. The receivers are located on the surface with 0.1 m of depth, with 1 m space intervals, and from 0 to 150 m of horizontal distance from the source. In this simulation, we use a 70 ppw Rayleigh. The recorded data are presented in Figure 4.17.

Figure 4.16 Earth model with soil-column. In the top layer $V_P = 1800$ (m/s), $V_S = 300$ (m/s) and $\rho = 1500$ (kg/m^3). In the bottom layer $V_P = 2000$ (m/s), $V_S = 600$ (m/s) and $\rho = 2000$ (kg/m^3). The thickness of the soil-column is 20 m.

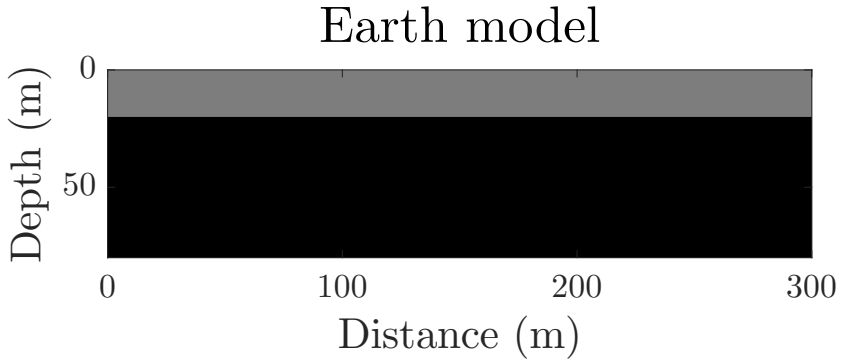

Figure 4.17 Vertical and horizontal shot gathers obtained from the model in Figure 4.16.

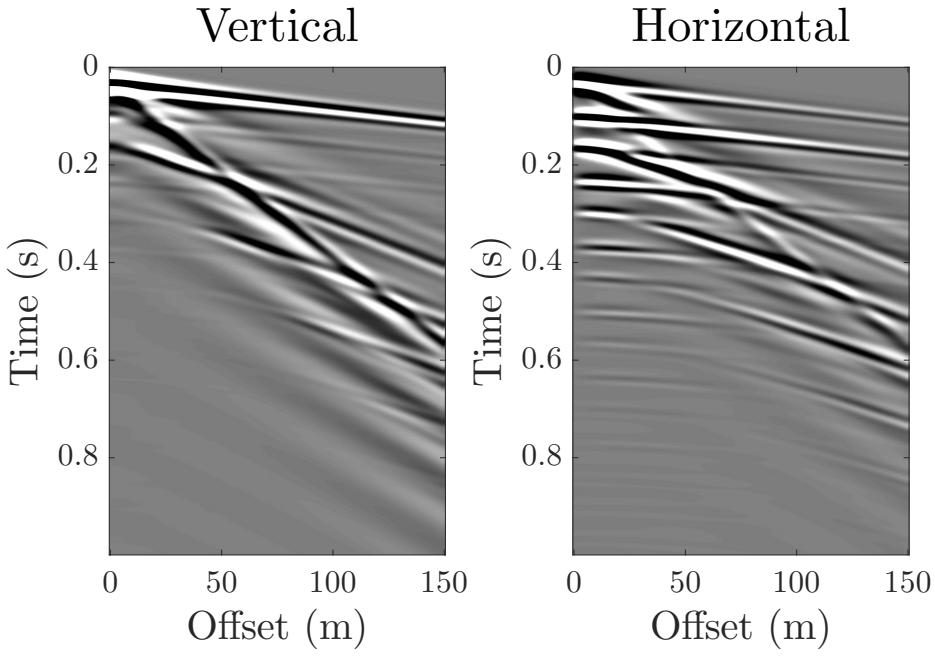

The Figure 4.18 shows the seismic attributes computed from seismic data in Figure 4.17. It is possible to identify the values of the seismic attributes in the direct body wave, the Rayleigh wave and the higher modes. In this example, the Rayleigh wave become less dispersive than in the two previous example because the thickness of the soil-column is higher.

Figure 4.18 Seismic attributes computed from shot gathers in Figure 4.17. The attributes are computed with a time window of 0.4 seconds of duration.

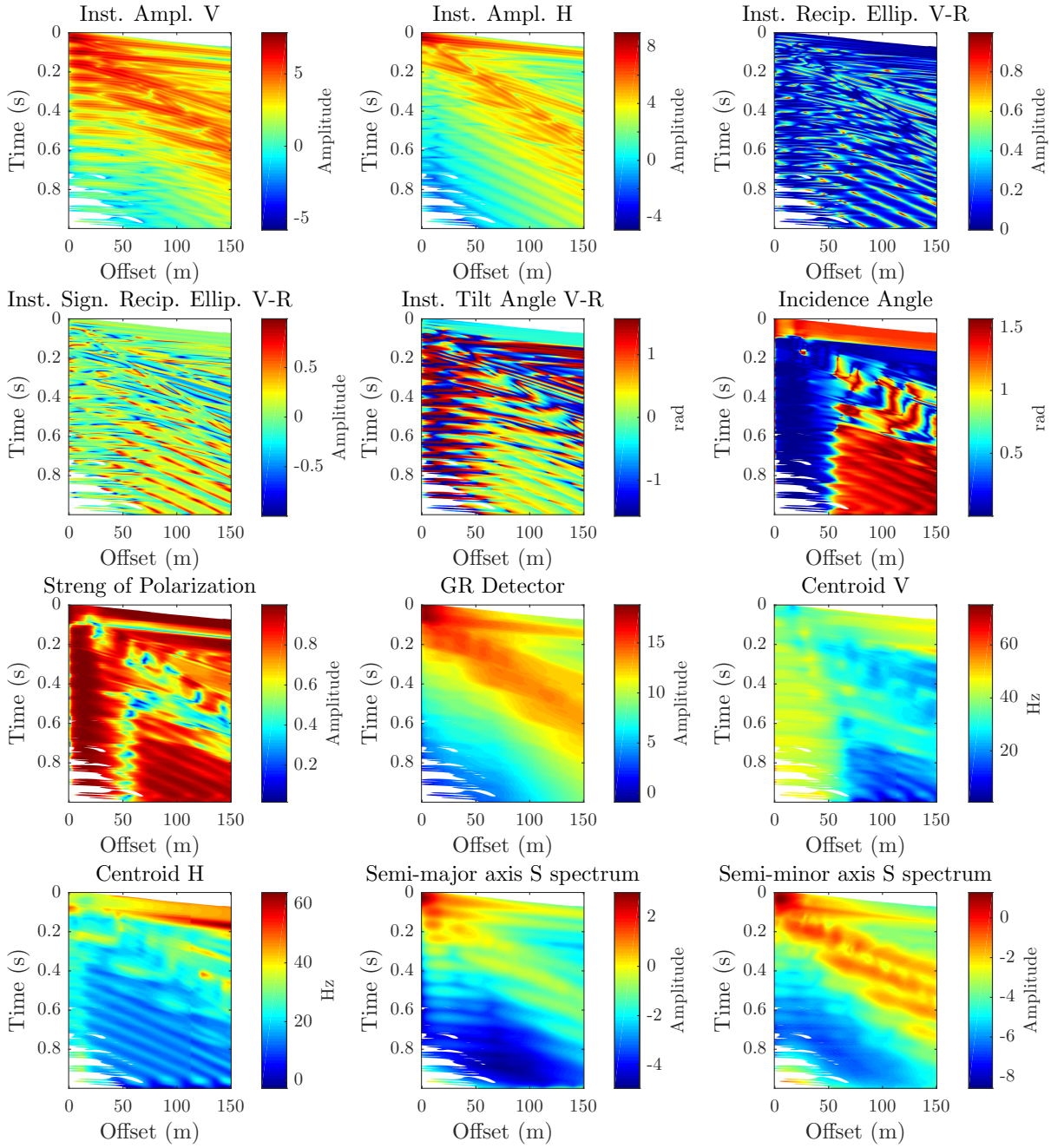

Example 3.1

For this example, we have built the velocity model showed in Figure 4.19. The bedrock is a sinusoid with amplitude $0.5\lambda_R$ and period $10\lambda_R$. The source function is a Ricker wavelet with central frequency of 30 (Hz). The source has been located in 7.5 m of depth and 100 m of horizontal distance. The receivers are located on the surface with 0.1 m of depth, with 1 m space intervals, and from 0 to 150 m of horizontal distance from the source. In this simulation, we use a 70 ppw Rayleigh. The recorded data are presented in Figure 4.20.

Figure 4.19 Earth model with weathering layer. In the top layer $V_P = 1800$ (m/s), $V_S = 300$ (m/s) and $\rho = 1500$ (kg/m^3). In the bottom layer $V_P = 2000$ (m/s), $V_S = 600$ (m/s) and $\rho = 2000$ (kg/m^3). The bedrock is a sinusoid with amplitude $0.5\lambda_R$ and period $10\lambda_R$.

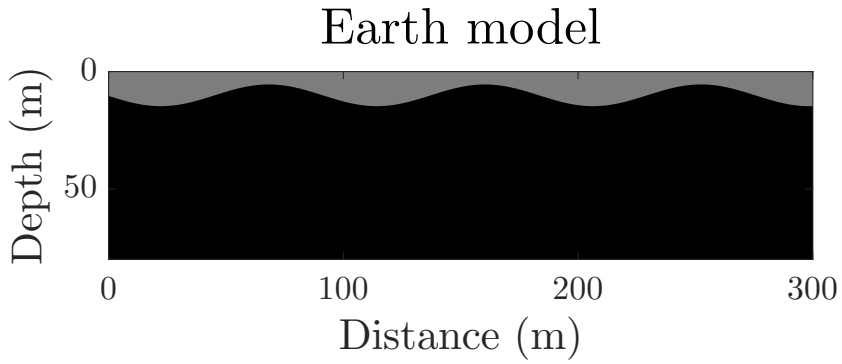

Figure 4.20 Vertical and horizontal shot gathers obtained from the model in Figure 4.19.

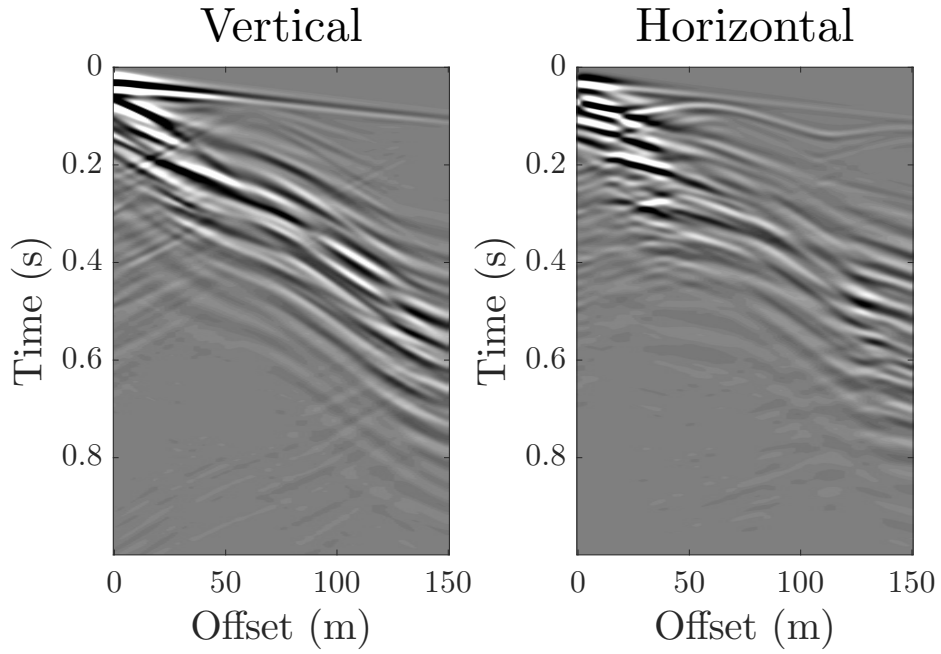

The Figure 4.21 shows the seismic attributes computed from seismic data in Figure 4.20. It is possible to identify the values of the seismic attributes in the direct body wave, the Rayleigh wave and the higher modes. In this example, the Rayleigh wave and the higher modes have small variations in the propagation velocity.

Figure 4.21 Seismic attributes computed from shot gathers in Figure 4.20.

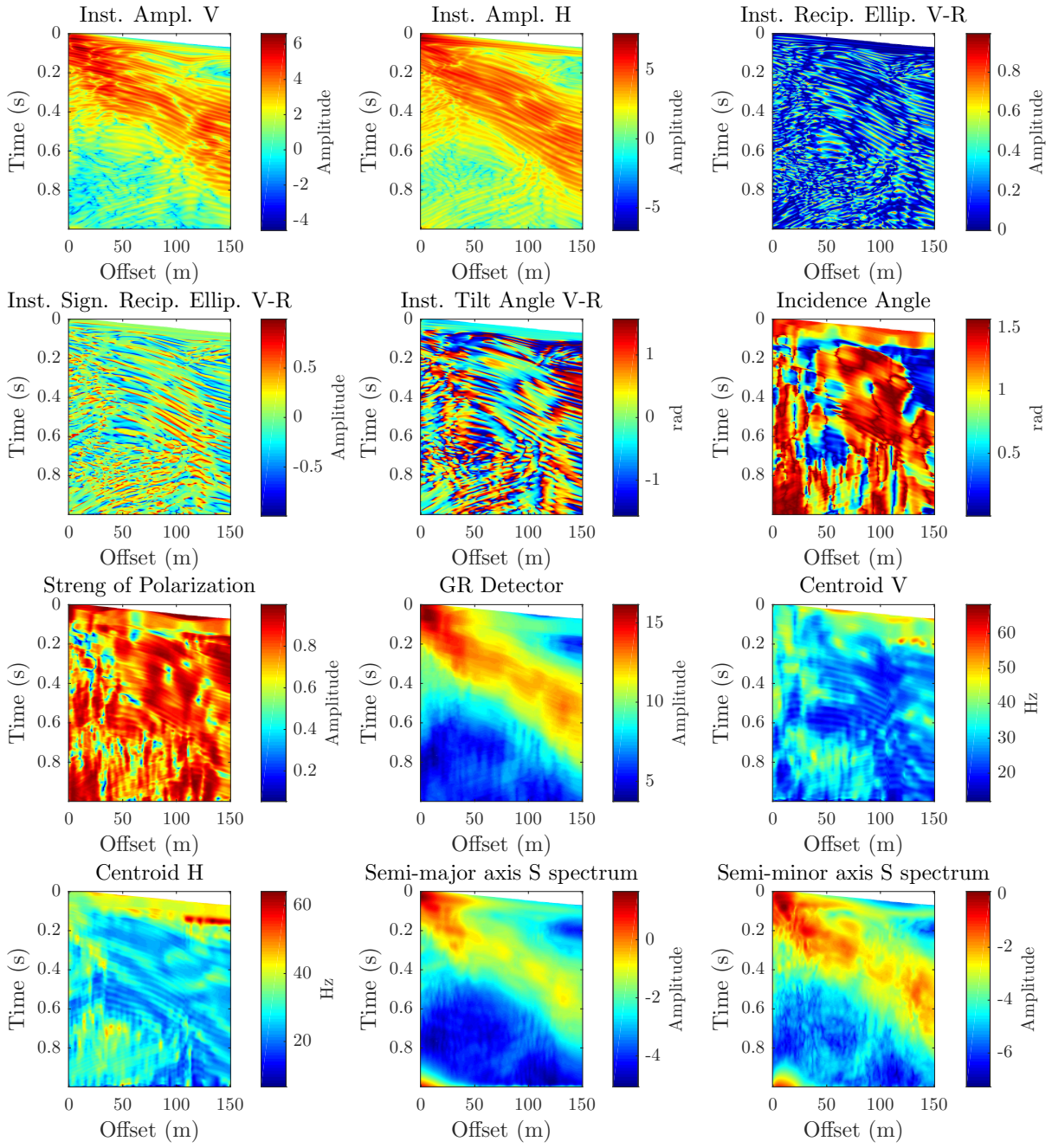

Example 3.2

For this example, we have built the velocity model showed in Figure 4.22. The bedrock is a sinusoid with amplitude $0.5\lambda_R$ and period $4\lambda_R$. The source function is a Ricker wavelet with central frequency of 30 (Hz). The source has been located in 7.5 m of depth and 100 m of horizontal distance. The receivers are located on the surface with 0.1 m of depth, with 1 m space intervals, and from 0 to 150 m of horizontal distance from the source. In this simulation, we use a 70 ppw Rayleigh. The recorded data are presented in Figure 4.23.

Figure 4.22 Earth model with weathering layer. In the top layer $V_P = 1800$ (m/s), $V_S = 300$ (m/s) and $\rho = 1500$ (kg/m^3). In the bottom layer $V_P = 2000$ (m/s), $V_S = 600$ (m/s) and $\rho = 2000$ (kg/m^3). The bedrock is a sinusoid with amplitude $0.5\lambda_R$ and period $4\lambda_R$.

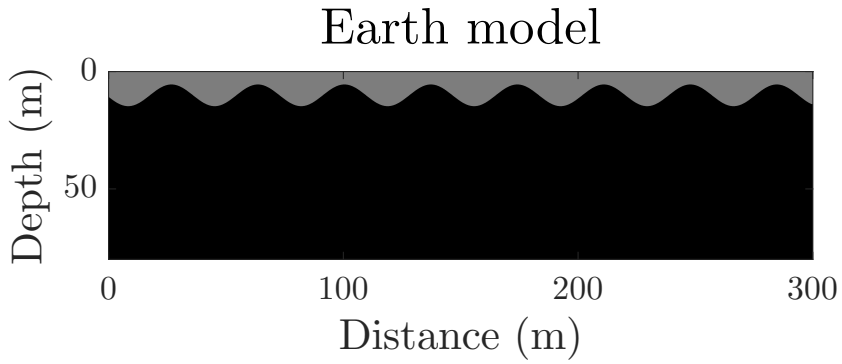

Figure 4.23 Vertical and horizontal shot gathers obtained from the model in Figure 4.22.

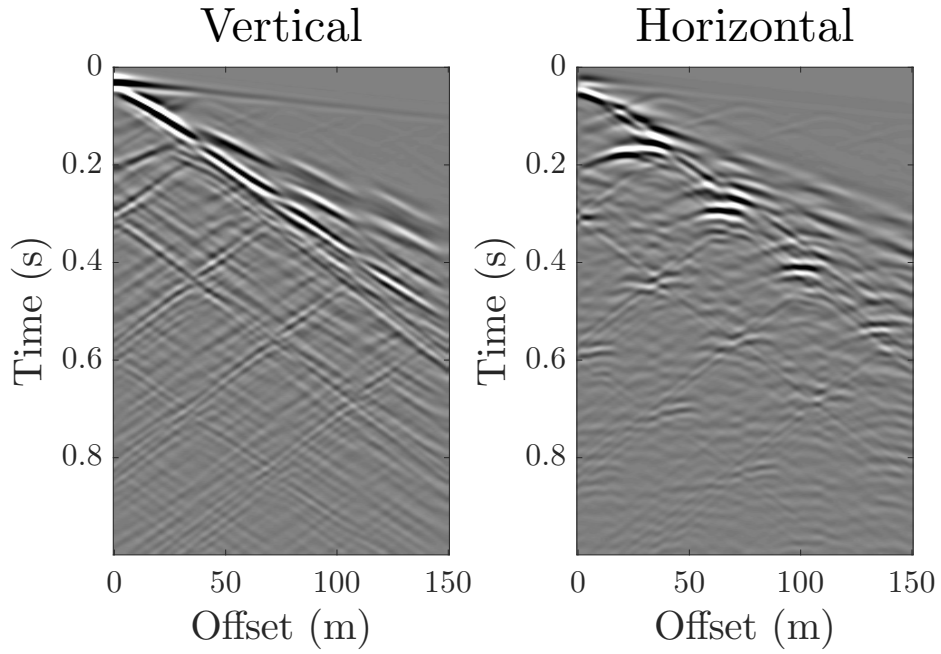

The Figure 4.24 shows the seismic attributes computed from seismic data in Figure 4.23. It is possible to identify the values of the seismic attributes in the direct body wave, the Rayleigh wave and the higher modes. In this example, the presence of scattering of Rayleigh waves is notorious.

Figure 4.24 Seismic attributes computed from shot gathers in Figure 4.23. The attributes are computed with a time window of 0.4 seconds of duration.

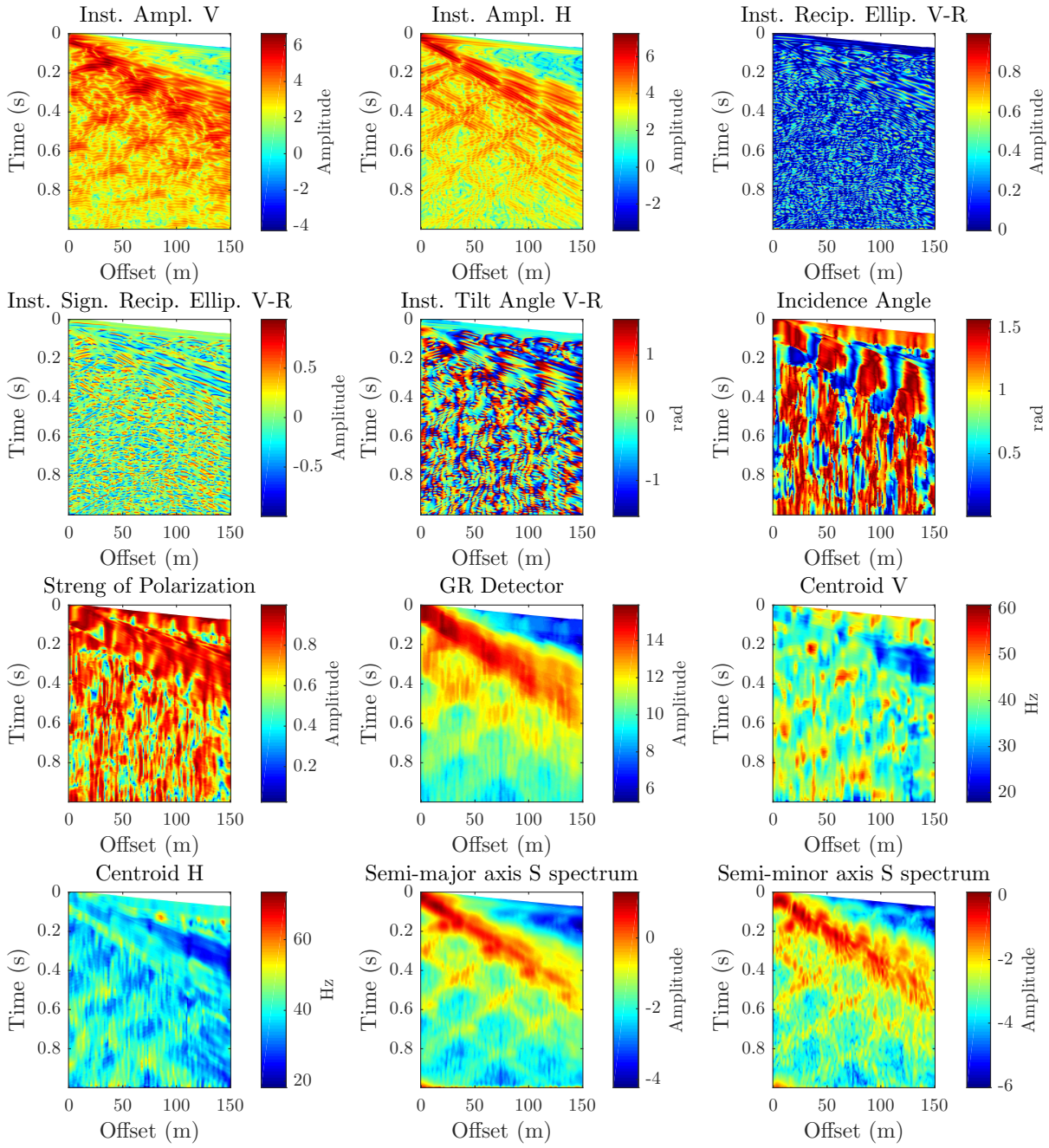

Example 3.3

For this example, we have built the velocity model showed in Figure 4.25. The bedrock is a sinusoid with amplitude $0.5\lambda_R$ and period $2\lambda_R$. The source function is a Ricker wavelet with central frequency of 30 (Hz). The source has been located in 7.5 m of depth and 100 m of horizontal distance. The receivers are located on the surface with 0.1 m of depth, with 1 m space intervals, and from 0 to 150 m of horizontal distance from the source. In this simulation, we use a 70 ppw Rayleigh. The recorded data are presented in Figure 4.26.

Figure 4.25 Earth model with weathering layer. In the top layer $V_P = 1800$ (m/s), $V_S = 300$ (m/s) and $\rho = 1500$ (kg/m^3). In the bottom layer $V_P = 2000$ (m/s), $V_S = 600$ (m/s) and $\rho = 2000$ (kg/m^3). The bedrock is a sinusoid with amplitude $0.5\lambda_R$ and period $2\lambda_R$.

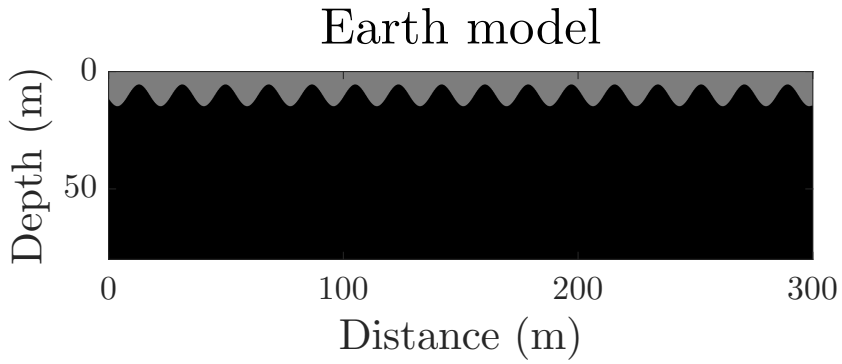

Figure 4.26 Vertical and horizontal shot gathers obtained from the model in Figure 4.25.

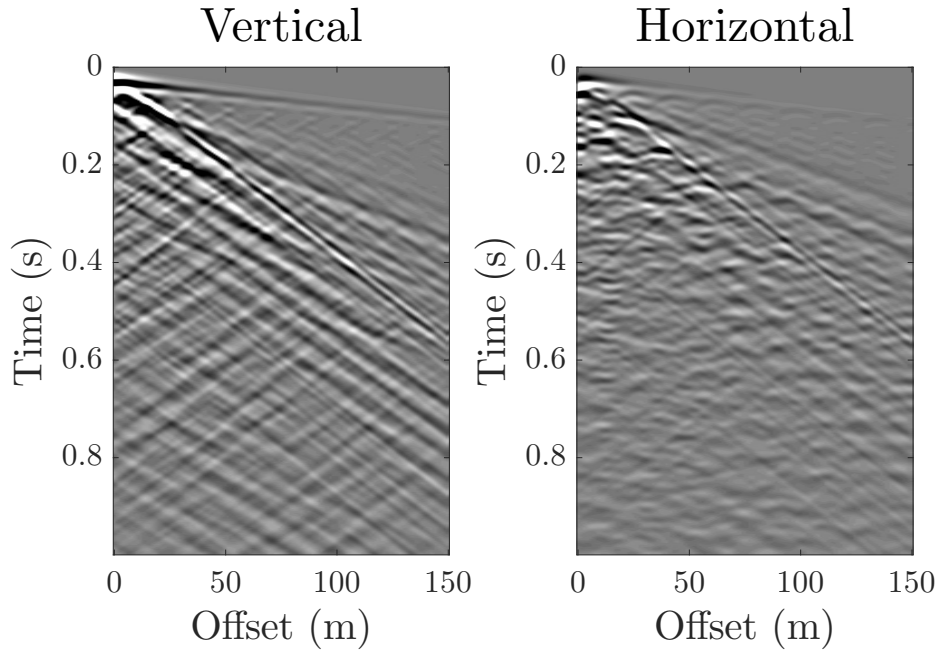

The Figure 4.27 shows the seismic attributes computed from seismic data in Figure 4.26. It is possible to identify the values of the seismic attributes in the direct body wave, the Rayleigh wave and the higher modes. In this example, the scattering of Rayleigh waves has a stronger presence than in the two previous examples.

Figure 4.27 Seismic attributes computed from shot gathers in Figure 4.26. The attributes are computed with a time window of 0.4 seconds of duration.

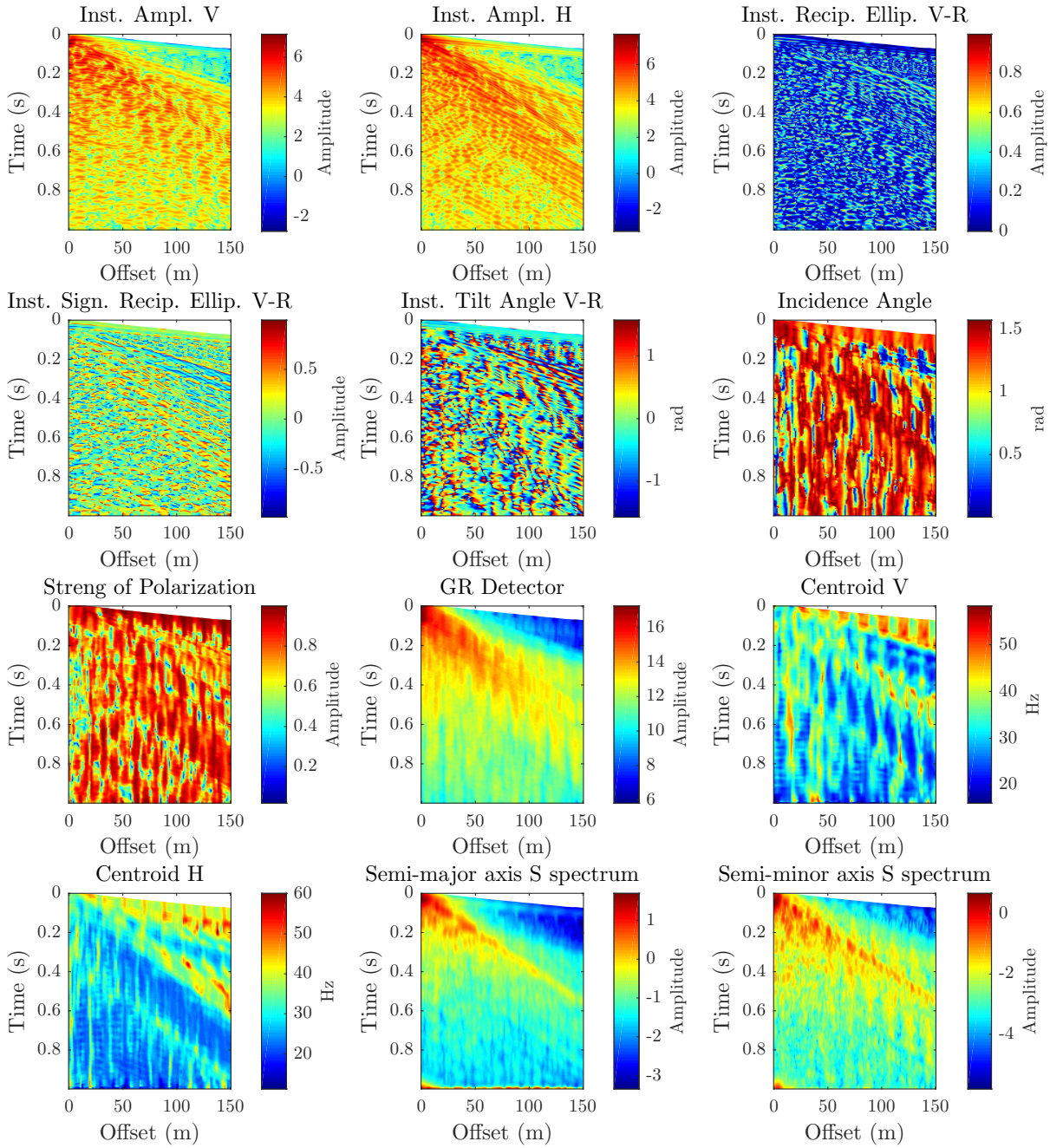

Example 4.1

For this example, we have built the velocity model showed in Figure 4.28. The topography is a sinusoid with amplitude $0.5\lambda_R$ and period $20\lambda_R$ and the mean thickness of the soil column is 10 m. The source function is a Ricker wavelet with central frequency of 30 (Hz). The source has been located in 7.5 m of depth and 100 m of horizontal distance. The receivers are located on the surface with 0.1 m of depth, with 1 m space intervals, and from 0 to 150 m of horizontal distance from the source. In this simulation, we use a 70 ppw Rayleigh. The recorded data are presented in Figure 4.29.

Figure 4.28 Earth model with soil-column. In the top layer $V_P = 1800$ (m/s), $V_S = 300$ (m/s) and $\rho = 1500$ (kg/m^3). In the bottom layer $V_P = 2000$ (m/s), $V_S = 600$ (m/s) and $\rho = 2000$ (kg/m^3). The topography is a sinusoid with amplitude $0.5\lambda_R$ and period $20\lambda_R$.

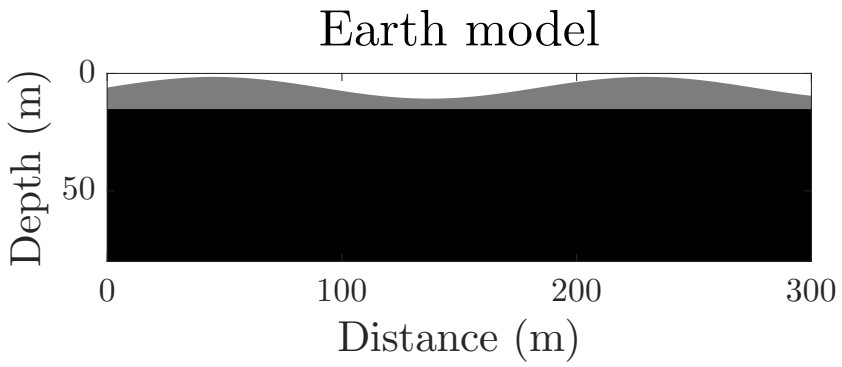

Figure 4.29 Vertical and horizontal shot gathers obtained from the model in Figure 4.28.

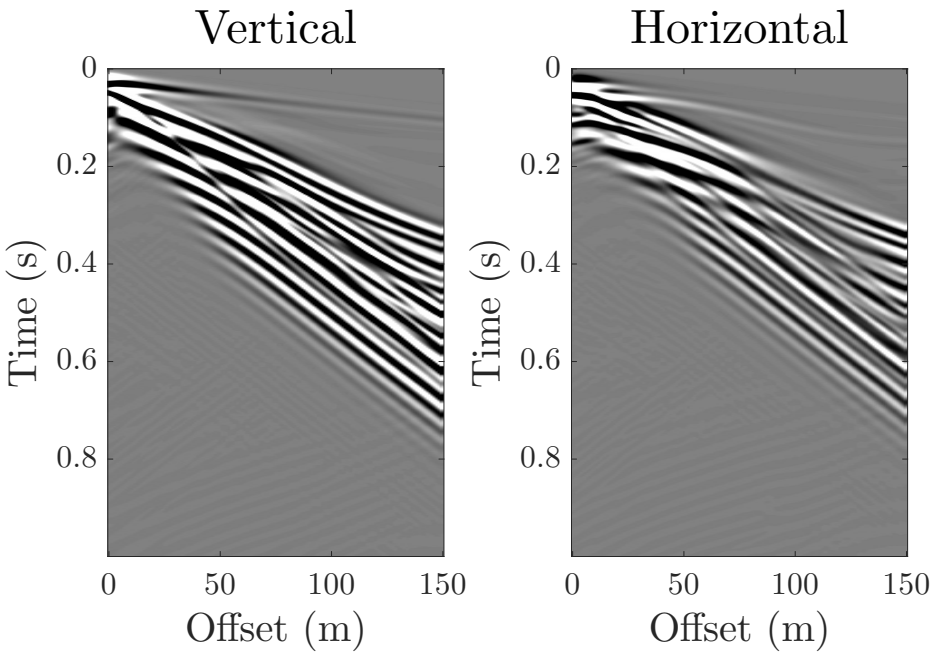

The Figure 4.30 shows the seismic attributes computed from seismic data in Figure 4.29. It is possible to identify the values of the seismic attributes in the direct body wave, the Rayleigh wave and the higher modes. In this example, some portion of the higher modes are separated from the rest, this maybe is produced by variations in the thickness of the soil-column.

Figure 4.30 Seismic attributes computed from shot gathers in Figure 4.29.

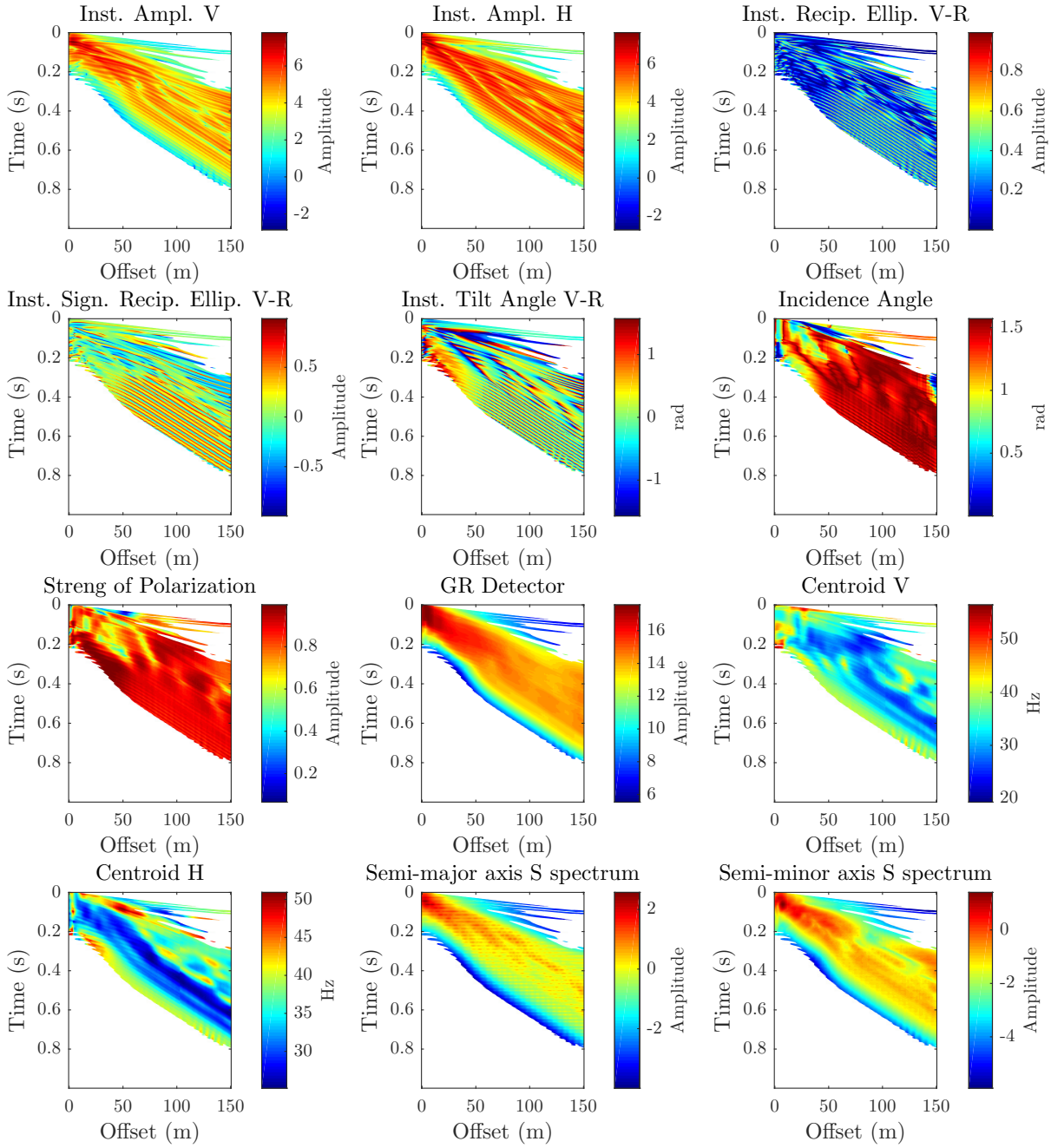

Example 4.2

For this example, we have built the velocity model showed in Figure 4.31. The topography is a sinusoid with amplitude $0.5\lambda_R$ and period $10\lambda_R$ and the mean thickness of the soil column is 10 m. The source function is a Ricker wavelet with central frequency of 30 (Hz). The source has been located in 7.5 m of depth and 100 m of horizontal distance. The receivers are located on the surface with 0.1 m of depth, with 1 m space intervals, and from 0 to 150 m of horizontal distance from the source. In this simulation, we use 70 ppw Rayleigh. The recorded data are presented in Figure 4.32.

Figure 4.31 Earth model with soil-column. In the top layer $V_P = 1800$ (m/s), $V_S = 300$ (m/s) and $\rho = 1500$ (kg/m^3). In the bottom layer $V_P = 2000$ (m/s), $V_S = 600$ (m/s) and $\rho = 2000$ (kg/m^3). The topography is a sinusoid with amplitude $0.5\lambda_R$ and period $10\lambda_R$.

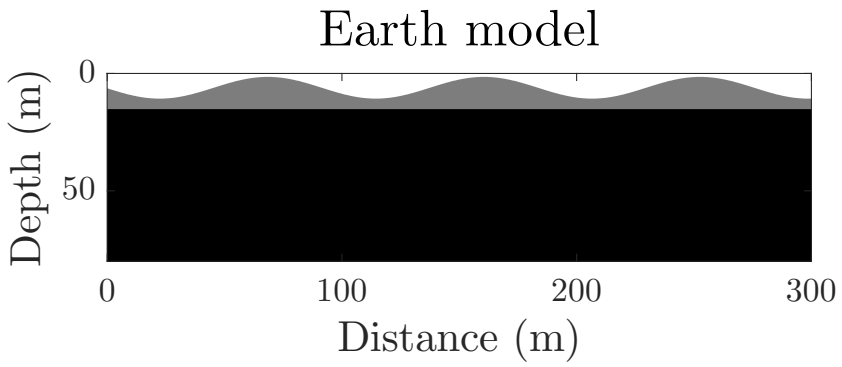

Figure 4.32 Vertical and horizontal shot gathers obtained from the model in Figure 4.31.

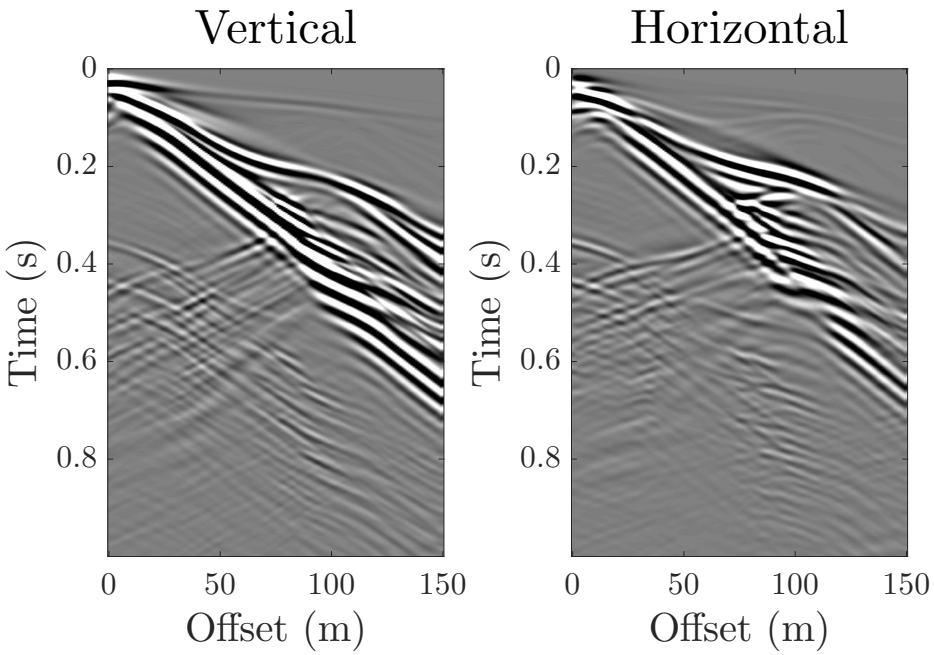

The Figure 4.33 shows the seismic attributes computed from seismic data in Figure 4.32. It is possible to identify the values of the seismic attributes in the direct body wave, the Rayleigh wave and the higher modes. In this example, some portion of the higher modes are separated from the rest, which maybe is produced by variations in the thickness of the soil-column. Additionally, Rayleigh waves scattering is caused by these variations.

Figure 4.33 Seismic attributes computed from shot gathers in Figure 4.32.

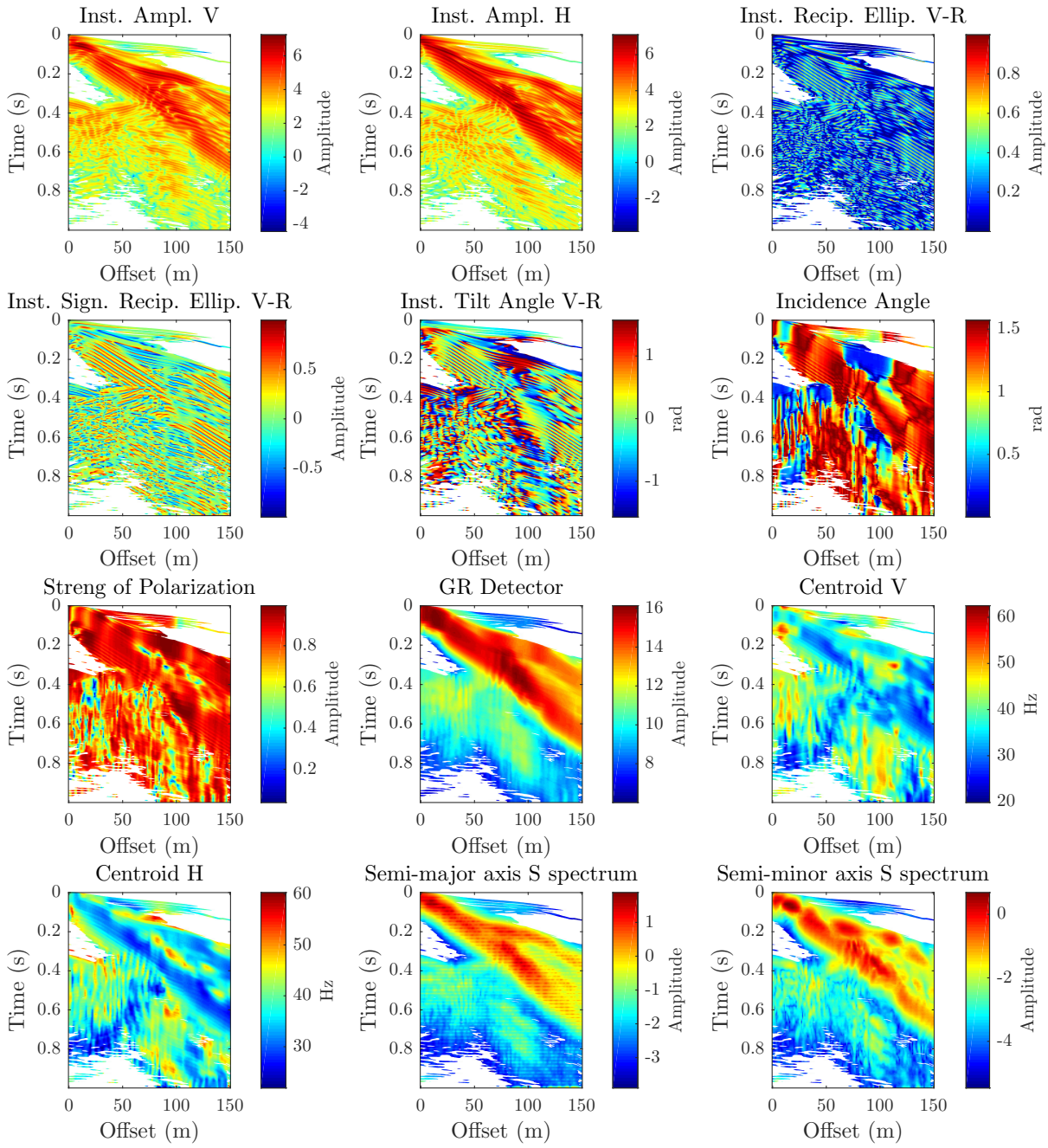

Example 4.3

For this example, we have built the velocity model showed in Figure 4.34. The topography is a sinusoid with amplitude $0.5\lambda_R$ and period $4\lambda_R$ and the mean thickness of the soil column is 10 m. The source function is a Ricker wavelet with central frequency of 30 (Hz). The source has been located in 7.5 m of depth and 100 m of horizontal distance. The receivers are located on the surface with 0.1 m of depth, with 1 m space intervals, and from 0 to 150 m of horizontal distance from the source. In this simulation, we use a 70 ppw Rayleigh. The recorded data are presented in Figure 4.35.

Figure 4.34 Earth model with soil-column of 10 m of mean thickness. In the top layer $V_P = 1800$ (m/s), $V_S = 300$ (m/s) and $\rho = 1500$ (kg/m^3). In the bottom layer $V_P = 2000$ (m/s), $V_S = 600$ (m/s) and $\rho = 2000$ (kg/m^3). The topography is a sinusoid with amplitude $0.5\lambda_R$ and period $4\lambda_R$.

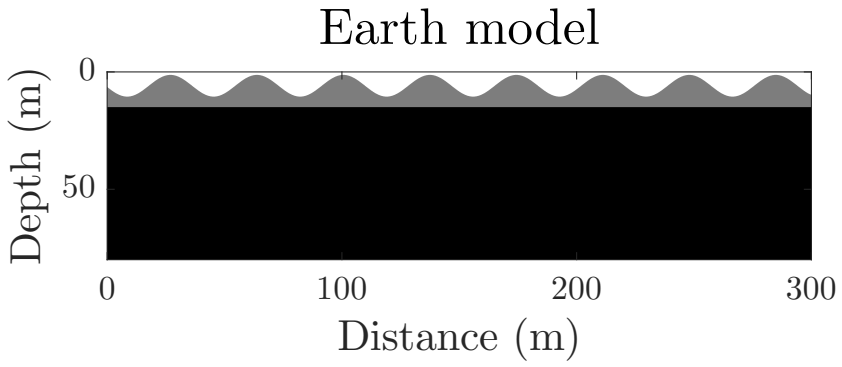

Figure 4.35 Vertical and horizontal shot gathers obtained from the model in Figure 4.34.

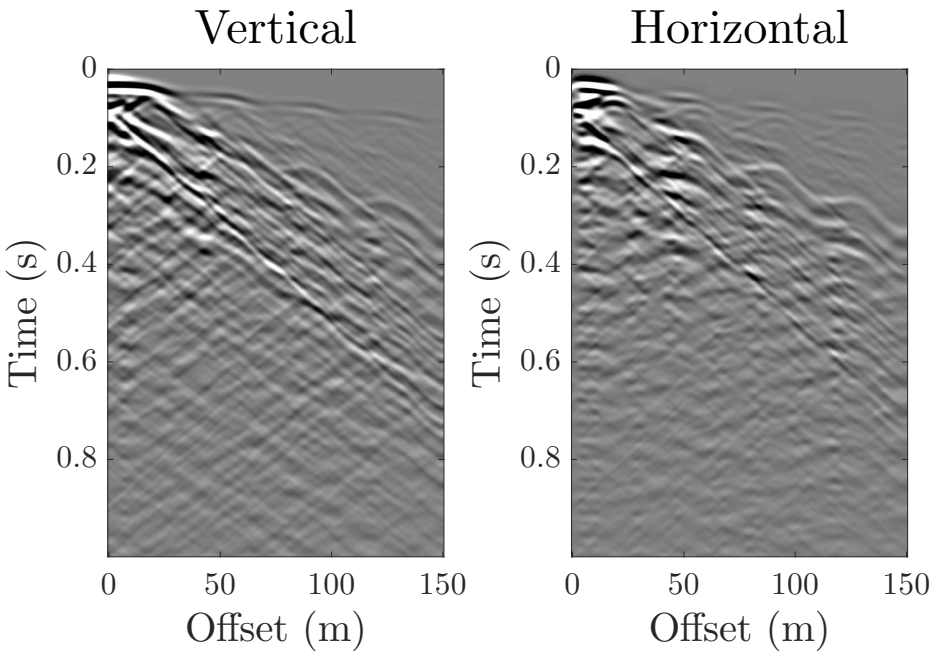

The Figure 4.36 shows the seismic attributes computed from seismic data in Figure 4.35. It is possible to identify the values of the seismic attributes in the direct body wave, the Rayleigh wave and the higher modes. In this example, some portion of the higher modes are separated from the rest, which maybe is produced by variations in the thickness of the soil-column. Additionally, Rayleigh waves scattering is caused by these variations.

Figure 4.36 Seismic attributes computed from shot gathers in Figure 4.35.

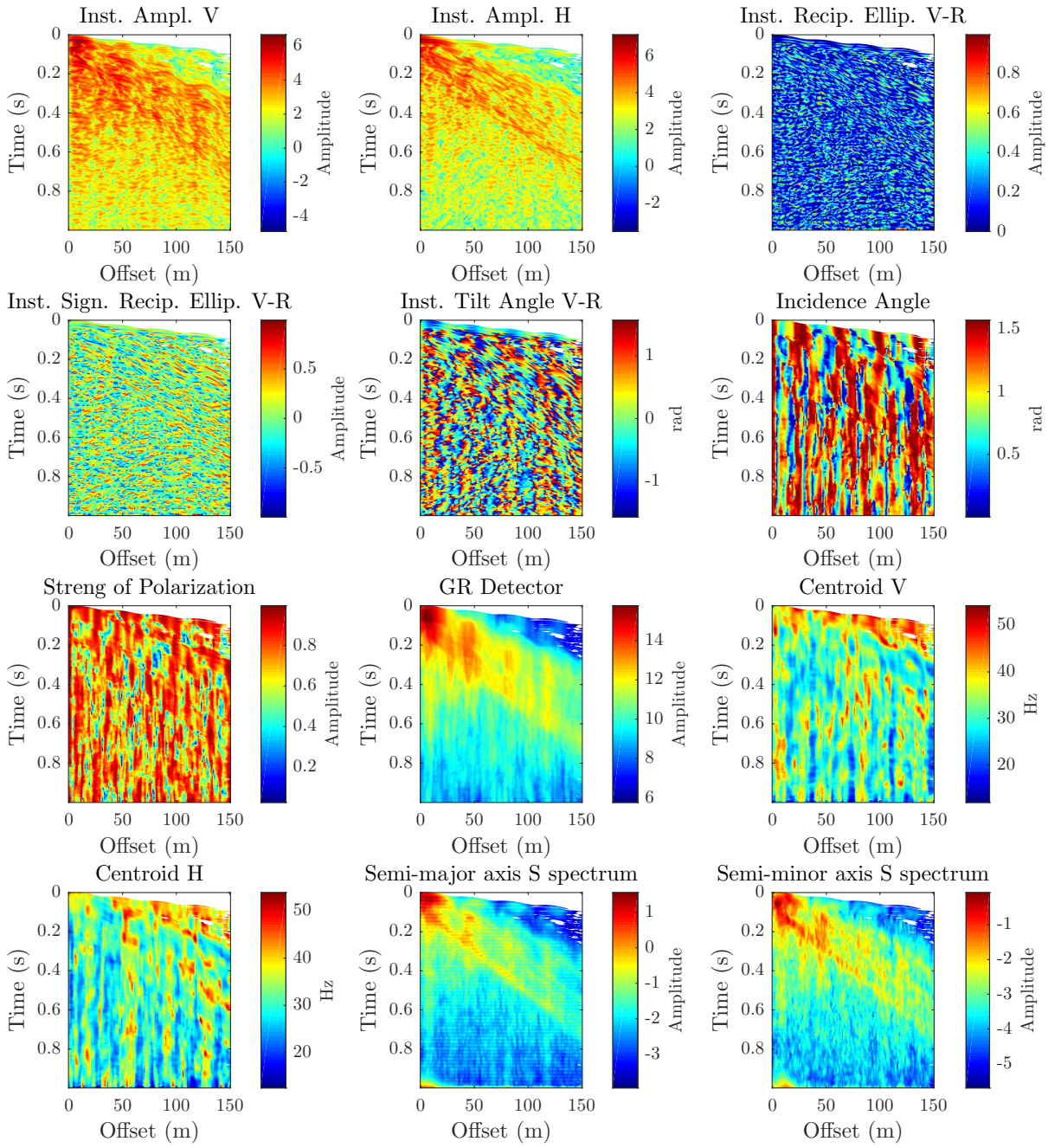

Example 4.4

For this example, we have built the velocity model showed in Figure 4.34. The topography is a gaussian hill with amplitude $2.6\lambda_R$ and variance $1.3\lambda_R$. The source function is a Ricker wavelet with central frequency of 30 (Hz). The source has been located in 7.5 m of depth and 100 m of horizontal distance. The receivers are located on the surface with 0.1 m of depth, with 1 m space intervals, and from 0 to 150 m of horizontal distance from the source. In this simulation, we use a 70 ppw Rayleigh. The recorded data are presented in Figure 4.35.

Figure 4.37 Earth model with soil-column of 10 m of mean thickness. In the top layer $V_P = 1800$ (m/s), $V_S = 300$ (m/s) and $\rho = 1500$ (kg/m^3). In the bottom layer $V_P = 2000$ (m/s), $V_S = 600$ (m/s) and $\rho = 2000$ (kg/m^3). The topography is a gaussian hill with amplitude $2.6\lambda_R$ and variance $1.3\lambda_R$.

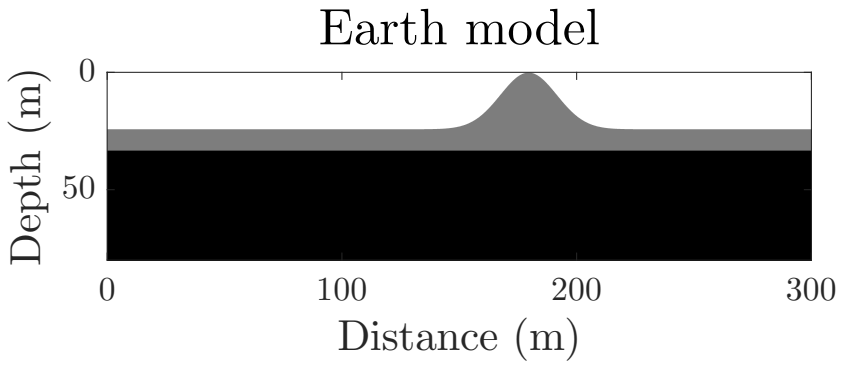

Figure 4.38 Vertical and horizontal shot gathers obtained from the model in Figure 4.37.

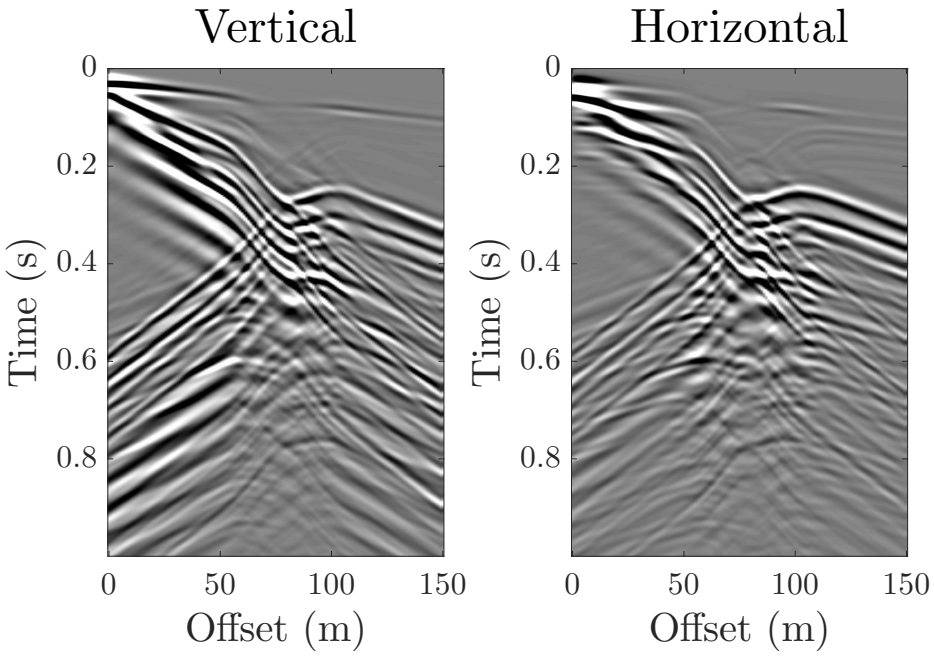

The Figure 4.39 shows the seismic attributes computed from seismic data in Figure 4.38. It is possible to identify the values of the seismic attributes in the direct body wave, the Rayleigh wave and the higher modes. In this example, a great portion of energy from higher modes, it is scattered because of strong variation of thickness of the soil column in the hill.

Figure 4.39 Seismic attributes computed from shot gathers in Figure 4.38.

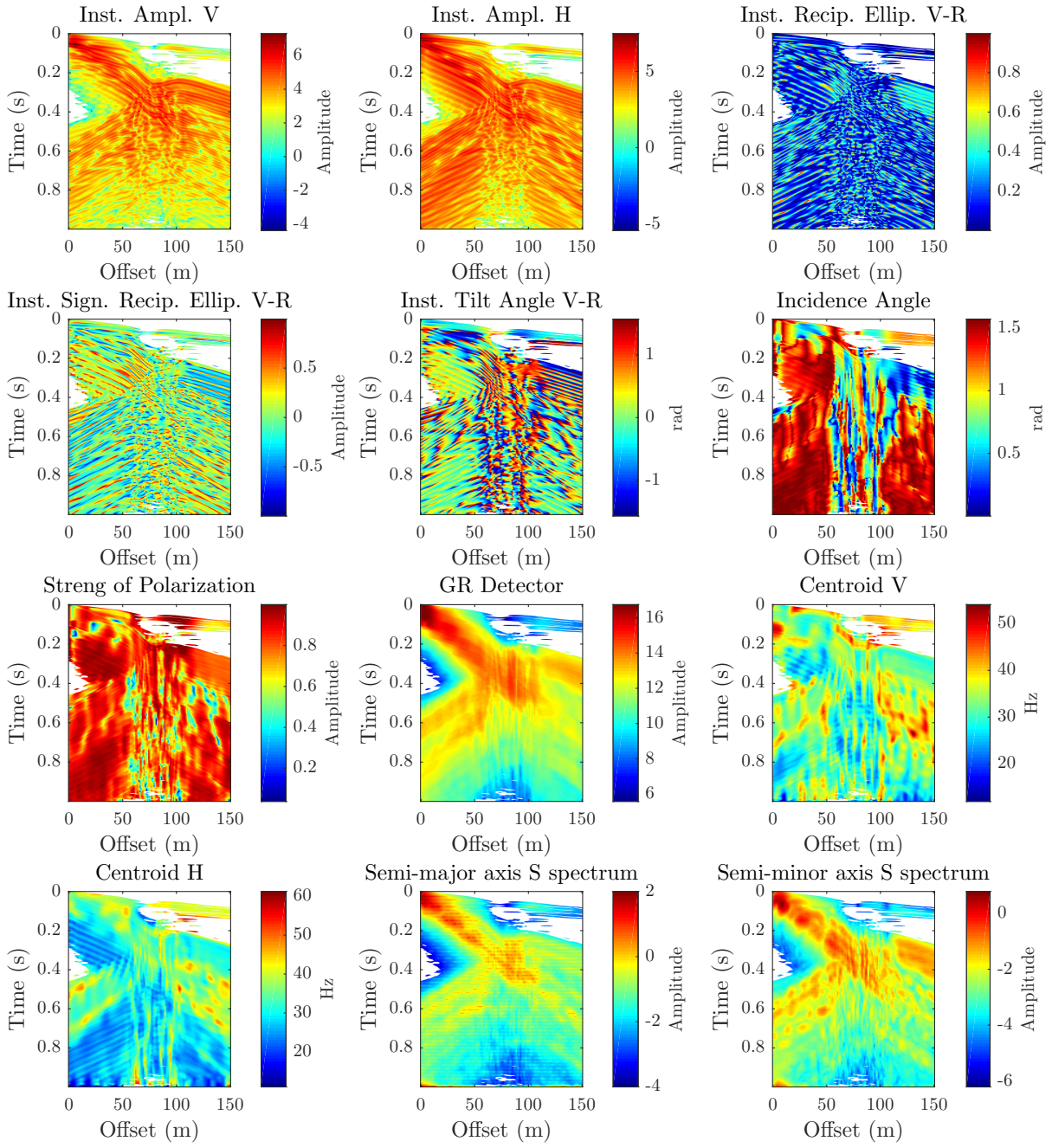

4.3 Discussion and conclusions

The moveout of the surface waves is strongly depending on the near-surface geometry and composition. From the simulation results, it is shown that surface waves propagation is affected by the surface topography, the soil-column and the irregular bedrock. From examples 1.1 to 1.3 it is possible to observe that the irregular topography affects the moveout of the Rayleigh wave and, when the topography is highly rough a great part of the Rayleigh wave energy is scattered. The computed seismic attributes enhance the Rayleigh wave properties. In Figures 4.3, 4.6 and 4.9 it is shown that the instantaneous amplitudes, the GR detector, the semi-major and the semi-minor axis S spectrum allow to identify the surface-waves scattering.

The Rayleigh wave dispersion is highly related to the thickness of the soil-column layer. From examples 2.1 to 2.3, it is observed that higher modes are produced when surface waves are propagated through earth models with thin soil-column. The higher modes of the Rayleigh wave are identified by the computed seismic attributes. In Figures 4.12, 4.15 and 4.18, it is noticed that the centroid frequencies are greater in the faster modes than the slower modes. Moreover, the strength of Polarization is higher in the slower modes and the the instantaneous amplitudes, the GR detector, the semi-major and the semi-minor axis S spectrum is higher in the faster modes.

According to the simulation results, it is possible to say that the surface waves scattering is strongly depending on thickness variations of the soil-column. From examples 3.1 to 4.4, it is observed that seismic waves propagation in earth models with soil-column and irregular topography or irregular bedrock gives rise to surface-waves scattering and backscattering. On the other hand, the seismic attributes enhance the Rayleigh wave properties. In Figures from 4.24 to 4.39, it is noticed that the instantaneous amplitudes, GR detector and the semi-axes of the S spectrum have high values inside the ground roll cone. Specially, In Figures 4.27 it is observed the presence of lines with the same slope of the Rayleigh wave moveout but in the opposite direction, indicating the presence of backscattered surface-waves.

For all of the above, we can conclude the following sentences:

- The higher variations in the surface topography, the higher scattered energy.
- The thinner soil-column layer, the higher the Rayleigh waves dispersion.
- The greater thickness variation of the soil-column layer, the higher scattered and backscattered surface waves.

Chapter 5

Comparison between seismic attributes of surface waves in synthetic and real data

Abstract

Realistic synthetic seismic data are very useful to geophysicists because they help to tune the processes and analysis used in seismic imaging. A way to know how realistic are some synthetic data is by means of the comparison of seismic attributes in both real and synthetic data. A comparison of the behavior of the seismic attributes of the surface waves between synthetic and real seismic data is presented. The synthetic acquisition was performed by elastic wave propagation modeling using finite differences and earth's models presented in the previous chapter. The real data correspond to three different acquisitions in Colombian surveys. Different surface waves behavior is noted in each type of data and the seismic attributes shown the similitudes ad differences between the real and synthetic seismic data.

5.1 Introduction

Real seismic data contain a variety of information corresponding to the propagation of different types of seismic waves. For their part, the synthetic data are acquired through controlled experiments and, therefore, the identification of each of the seismic events is simpler. In the previous chapters, we have concentrated on studying the behavior of surface waves in synthetic and real data from seismic attributes, which allows to enhance the information contained in shot gathers.

From Chapter 3, we conclude that seismic attributes for surface waves detection allow to numerically differentiate between surface waves from reflections. In some cases, this differentiation is realized by determining thresholds in a heuristic way. Moreover, some attributes have high correlation and it is necessary a stage of attribute selection to have an optimal set of attributes. These seismic attributes can be clustered in families where each family can describe an attribute in particular. From Chapter 5 we conclude that the seismic attributes computed from synthetic data enhance the Rayleigh wave, the higher modes and the surface waves scattering.

In this chapter, we focus on comparing the behavior of the seismic attributes of the surface waves between synthetic and real seismic data. The synthetic data were obtained by elastic wave propagation modeling and they were presented in the previous chapter. The real data consists of three types of data acquired in Colombia which are noted different surface waves behavior. For each field dataset twelve attributes are computed and the behavior of the results obtained is analyzed. The seismic attributes are clustered in families depending on the surface-waves features enhanced by each one.

5.2 Field data examples

The first dataset corresponds to a 2D-3C acquisition using a relative low frequency source (close to the frequencies commonly used for oil prospecting). The second and third dataset are 2D-3C acquisitions using a relatively high-frequency source. Table 2.2 shows the acquisition parameters for each dataset.

Table 5.1 Information about seismic acquisitions for the three sets of real data used in this work.

Acquisition Parameters	**Field Data 1**	**Field Data 2**	**Field Data 3**
Source type	Explosive gel	Explosive gel/caps	Explosive gel/caps
Load Size	1800/2250 g	150 g	150 g
Source Depth	10 m	10 m	10 m
Receiver Interval	10 m	5 m	5 m
Maximum Offset	1.8 Km	100 m	300 m
Sampling Rate	2 ms	0.5 ms	0.5 ms
Data Bandwidth	3-120 Hz	5-450 Hz	5-500 Hz

5.2.1 Field data 1

In Figure 5.1, the three-component shot gathers of the first field dataset are shown. In the shot gathers, it is possible to observe different phenomena associated to realistic near-surface, such as Rayleigh wave dispersion, moveout of surface waves variation, surface-waves scattering and backscattering.

Figure 5.1 Vertical, Radial and Transverse components of the first field dataset.

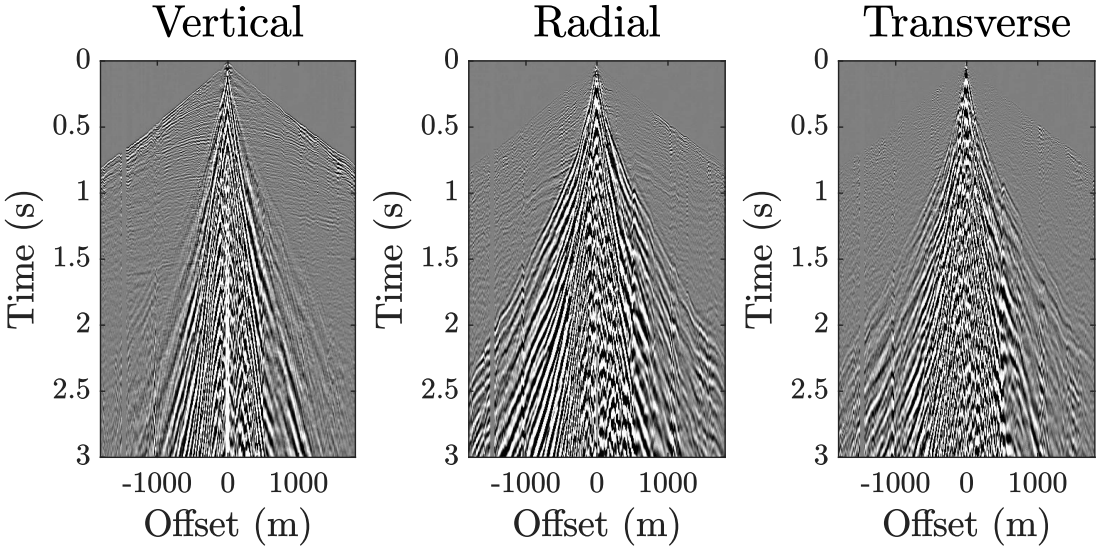

The seismic attributes computed from shot gathers are shown in the Figure 5.2. They allow to enhance each one of the previously mentioned phenomena. The instantaneous amplitude in the vertical and horizontal components have higher values inside the ground roll cone than outside of it. The instantaneous reciprocal ellipticities don't enhance the ground roll cone but they slightly let see the higher modes area. The instantaneous tilt angle ranges from $-\frac{\pi}{2}$ to $\frac{\pi}{2}$ in the higher modes zone and it is close to zero outside of that zone, so it is possible to detect the zone. Similarly, the incident angle heightens the higher modes zone because it is close to zero inside that zone and it variates in values close to π outside of that zone. The strength of polarization stands out in the higher modes zone as much as the direct body-waves zone. The GR detector strongly enhance the Rayleigh waves and scattering. The frequency centroids exhibit all the ground roll cone because they are lower values in that cone. Finally, it is possible to observe that the semi-axis of the S spectrum heightens the Rayleigh wave.

In the Table 5.2, the seismic attributes with the best visual enhancement for each of the surface-waves phenomena are shown. The attribute selection was performed in a qualitative way by visual inspection.

Table 5.2 The seismic attributes with the best visual enhancement for each of the surface-waves phenomena in field data 1.

Surface-waves phenomena	**Seismic attributes**
Rayleigh wave	Semi-axis S spect, GR detector
Dispersion (Higher modes)	Instan. Ampl., Instan. Ang. , Str. of Pol.,
Scattering and Backscattering,	GR detector, Centroids

Figure 5.2 Seismic attributes computed from shot gathers in Figure 5.1. The attributes are computed with a time window of 0.4 seconds of duration.

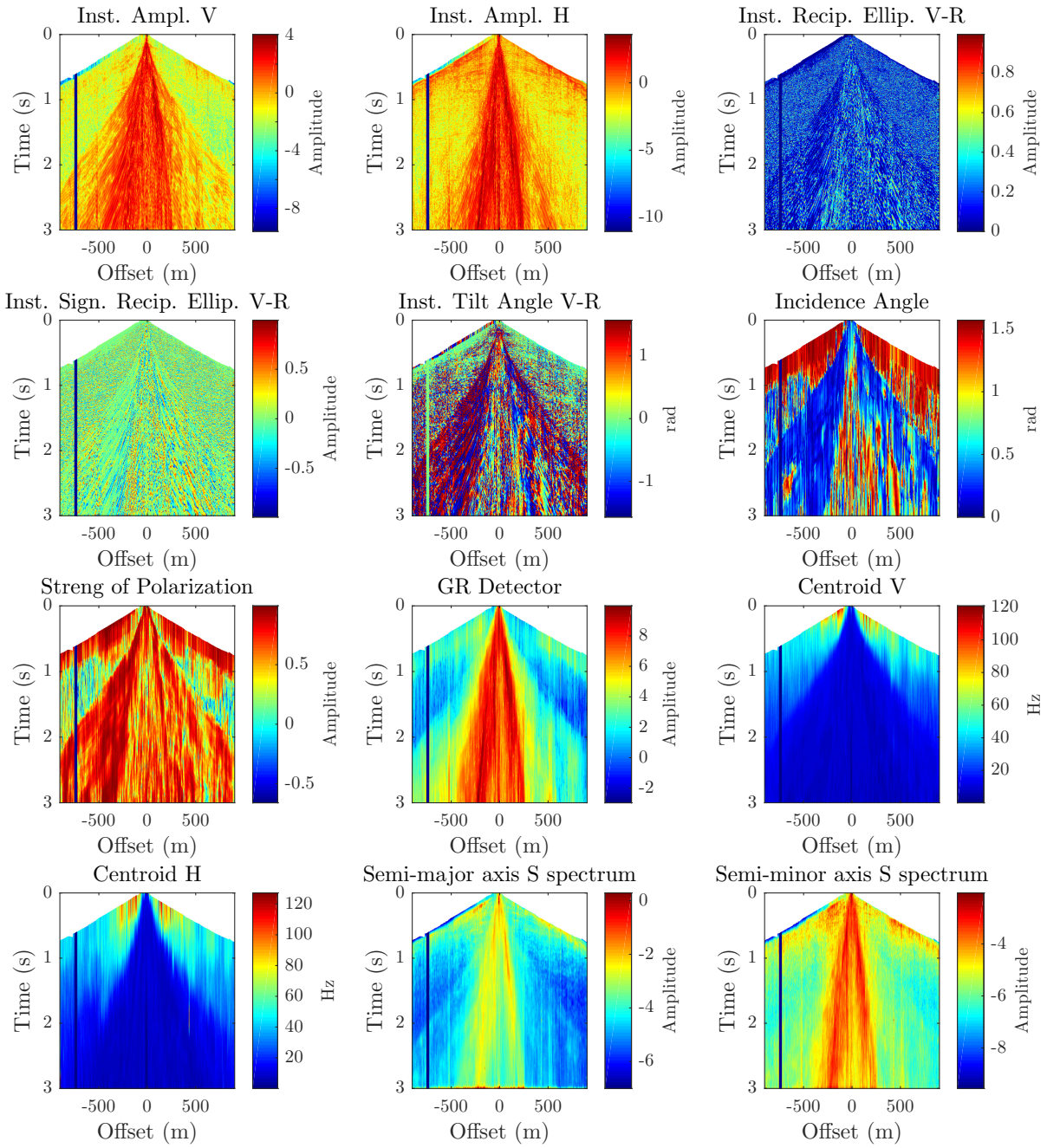

5.2.2 Field data 2

The Figure 5.3 shows the three-component shot gathers of the second field dataset. In the shot gathers, it is possible to observe the Rayleigh wave and some higher modes. In contrast to the previous field data, the surface-waves are not a cone but are two tilted bands, which between them, body-waves reflections and multiples are observed. Additionally, the energy of surface-waves backscattering is noticed in the radial and vertical component.

Figure 5.3 Vertical, Radial and Transverse components of the second field dataset.

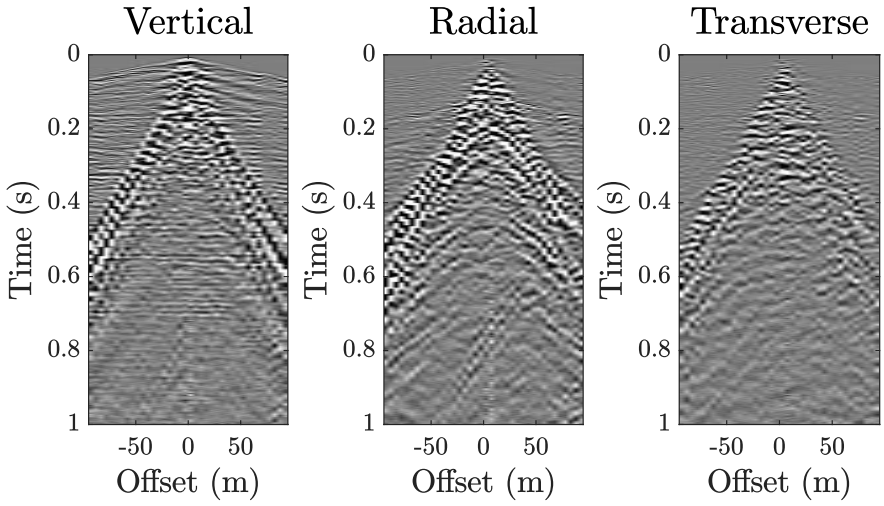

The seismic attributes computed from shot gathers of the second field data are shown in the Figure 5.4. They allow to enhance each one of the surface-waves phenomena. The instantaneous amplitude in the vertical and horizontal components have higher values in the Rayleigh wave zone than outside of it. The instantaneous reciprocal ellipticities don't enhance any information related with surface-waves neither body-wave. Like in the first field dataset, the instantaneous tilt angle ranges from $-\frac{\pi}{2}$ to $\frac{\pi}{2}$ in the higher modes zone and it is close to zero outside of that zone, so it is possible to detect the zone. Moreover, the backscattering is noticed too. Similarly, the incident angle heightens the higher modes zone and the backscattering zone because it is close to zero there and it variates in values close to π outside of that zones. The strength of polarization enhances the higher modes zone as much as the direct body-waves zone. The GR detector strongly increase the visualization of the Rayleigh waves and it slightly emboss the backscattering zone. The frequency centroids exhibit all the Rayleigh wave bands because they are lower values there and they are higher values in the bottom of the shot gathers because great part of the energy there correspond to signal noise. Finally, it is possible to observe that the semi-axis of the S spectrum heightens the Rayleigh wave bands.

In the Table 5.3, the seismic attributes with the best visual enhancement for each of the surface-waves phenomena in the second field dataset are shown. The attribute selection was performed in a qualitative way by visual inspection.

Table 5.3 The seismic attributes with the best visual enhancement for each of the surface-waves phenomena in field data 2.

Surface-waves phenomena	**Seismic attributes**
Rayleigh wave	Instan. Ampl., Semi-axis S spect, GR detector
Dispersion (Higher modes)	Instan. tilt Ang., Incidence Ang. , Str. of Pol.
Scattering and Backscattering,	GR detector, Centroids, Instan. tilt Ang.

Figure 5.4 Seismic attributes computed from shot gathers in Figure 5.3. The attributes are computed with a time window of 0.1 seconds of duration.

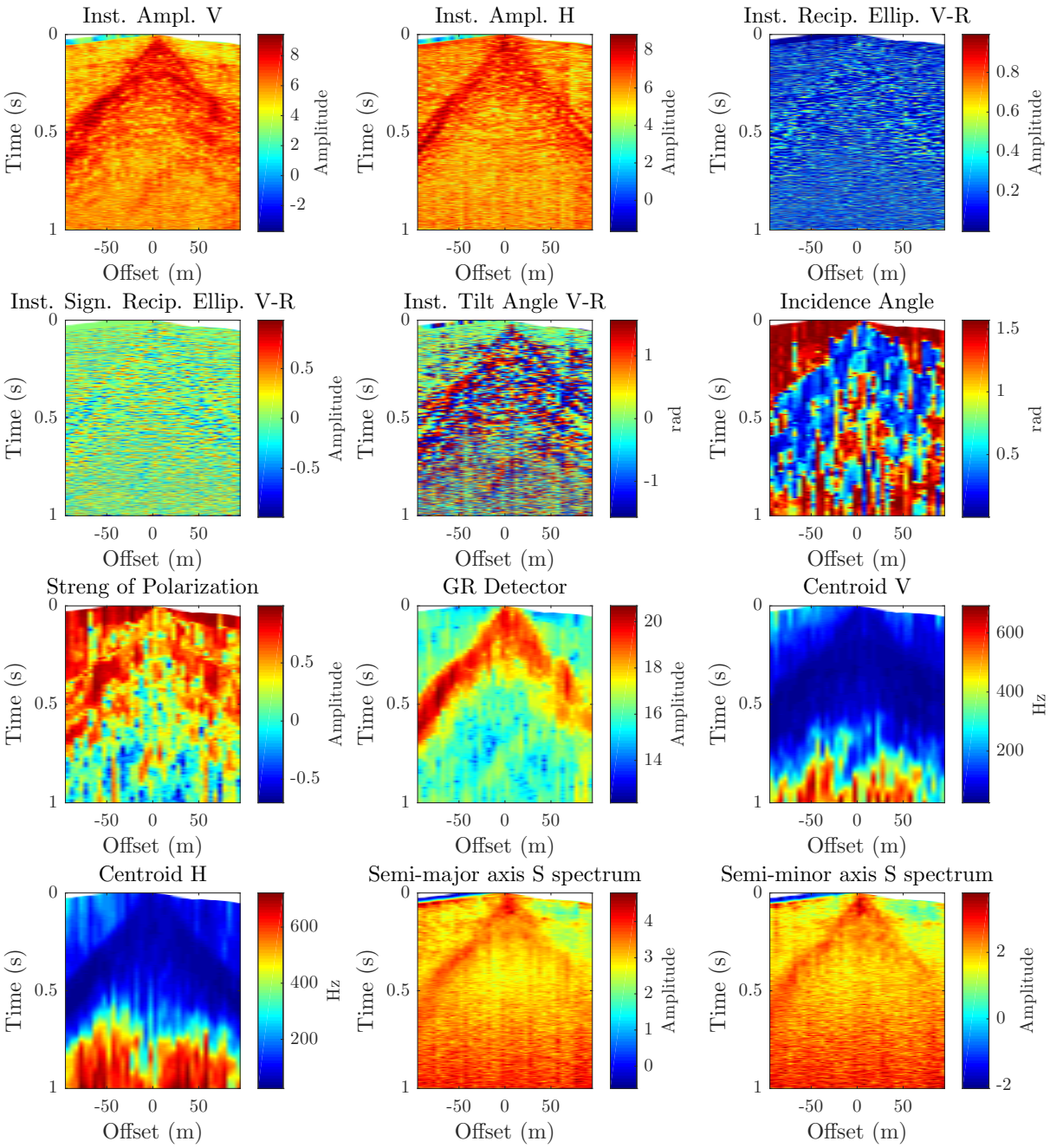

5.2.3 Field data 3

The Figure 5.5 shows the three-component shot gathers of the third field dataset. In the shot gathers, it is possible to observe the strong energy of surface waves. In the shot gather, the moveout of the surface waves is strongly affected and it is difficult to identify each of the phenomena related to surface waves. Great part of the surface-waves energy is scattered and reverberated.

Figure 5.5 Vertical, Radial and Transverse components of the third field dataset.

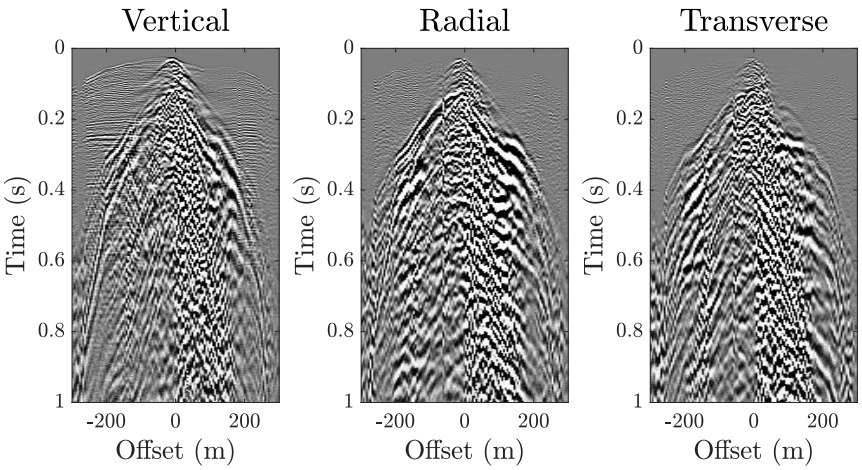

The seismic attributes computed from shot gathers of the third field data are shown in the Figure 5.6. It this example, it is difficult for seismic attributes to enhance each one of the surface-waves phenomena. The instantaneous amplitude in the vertical and horizontal components have higher values in one side of the shot gather in a zone may be related to surface-waves reverberations. The instantaneous reciprocal ellipticities don't enhance any information related with surface-waves neither body-wave. Like the previous field dataset, the instantaneous tilt angle ranges from $-\frac{\pi}{2}$ to $\frac{\pi}{2}$ in the surface-waves zone and it is close to zero outside in the purely body-waves zone, so it is possible to detect the ground roll zone. Similarly, the incident angle heightens the Rayleigh waves and some energy of the higher modes because it is close to zero there and it variates in values close to π outside there. The strength of polarization enhances the pure Rayleigh wave as much as the direct body-waves zone. The GR detector strongly increase the visualization of the surface-waves reverberation and it slightly emboss the Rayleigh waves zone. The frequency centroids exhibits all the surface-waves zone because they are lower values there and they are higher values in the bottom of the shot gathers because great part of the energy there correspond to signal noise. Finally, it is possible to observe that the semi-axis of the S spectrum heightens the Rayleigh wave reverberations.

In the Table 5.4, the seismic attributes with the best visual enhancement for each of the surface-waves phenomena in the third field dataset are shown. The attribute selection was performed in a qualitative way by visual inspection.

Table 5.4 The seismic attributes with the best visual enhancement for each of the surface-waves phenomena in field data 3.

Surface-waves phenomena	**Seismic attributes**
Rayleigh wave	Ins. Ampl., GR detector, Str. of Pol.
Dispersion (Higher modes)	Ins. Ang., Incidence Ang. , Centroids, Str. of Pol.
Scattering and Backscattering,	GR detector, Ins. Ang., semi-axis S spc, Ins. Ampl.

Figure 5.6 Seismic attributes computed from shot gathers in Figure 5.5. The attributes are computed with a time window of 0.1 seconds of duration.

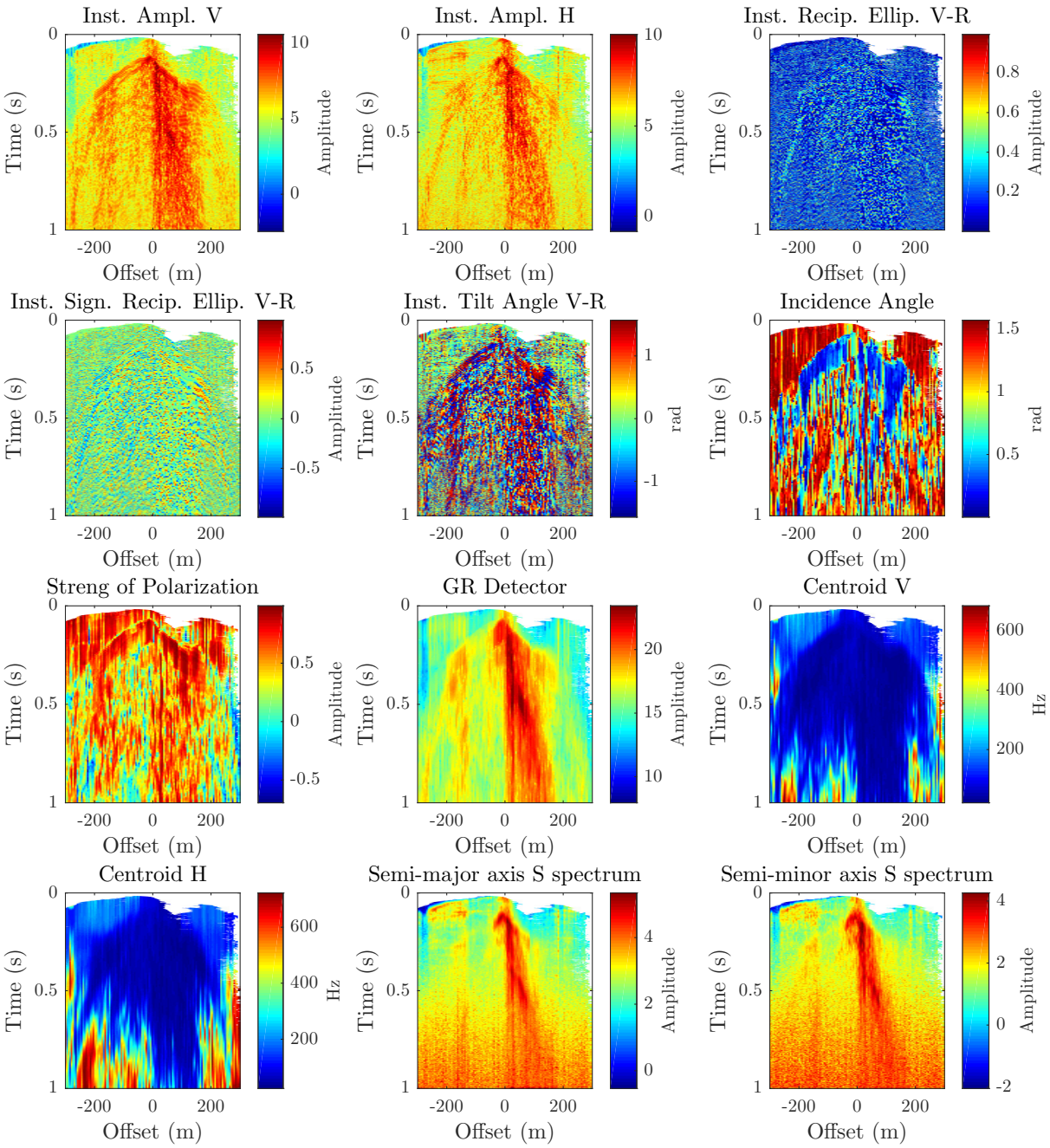

5.3 Analysis and discussion

In synthetic experiments, to have realistic Earth's velocity models with irregular near-surface is necessary to reproduce all the seismic wave phenomena presented in real data. The greater complexity of the velocity model, the greater complexity of the seismic data. From shot gathers and seismic attributes, we can note that the total complexity of the ground roll that was obtained in the field data couldn't be achieved, although the performed synthetic experiments in this work took into account some soil-column features (surface topography, irregular bedrock) that allowed to reproduce some realistic surface-waves phenomena (dispersion, scattering, backscattering).

In general, the seismic attributes behavior in the synthetic data is similar to the behavior in the real data. Some attributes allow to enhance specific features of surface-waves phenomena. The instantaneous amplitudes (vertical and horizontal) are higher in the surface-waves zone (Rayleigh wave and higher modes) than in body waves. This results from the amplitudes of the seismic signal of the surface waves are greater than the amplitudes of body waves. The instantaneous ellipticities don´t have a pattern to recognize some of the surface-waves phenomena features. The behavior os these attributes are chaotic in both, synthetic and real data. The instantaneous tilt angle and the incidence angle allow to identify higher modes of Rayleigh waves. This can be observed specially in the field data, where the instantaneous tilt angle is close to zero outside of the surface waves zone while the incidence angle is close to zero in that zone. Similarly, the strength of polarization generally enhances the higher modes zone and sometimes the body-waves zone. For its part, the GR detector is an efficient detector of Rayleigh wave and its higher modes. In all cases, the synthetic and real data, the GR detector enhanced the surface-waves cone in field data 1 and the surface-waves band in the field data 2. The frequency centroids helped to identify the combined surface-waves phenomena, which generally have frequency content lower than the rest of the information in seismic data. These attributes are highly sensitives to noise. In the field data examples 2 y 3, the affectation in the centroids at the bottom of the shot gathers is notorious. Finally, the semi-axes of the S spectrum heighten the information of the Rayleigh wave and its higher modes. When great part of the surface-waves energy is reverberated, these attributes tend to enhance more the reverberations than the pure Rayleigh wave (see Field data 1).

The differences between the synthetic data and the real data are due to the velocity models used are different in each case. The real velocity model is unknown and the synthetic velocity models weren't design them from real data. The synthetic velocity models are exclusively for showing the dependence of the surface-waves propagation on the near-surface structure. In that sense, from the experiments it is shown that the dispersion, the scattering and the backscattering of surface waves is caused by the surface topography and irregular bedrock.

5.4 Conclusions

We have performed a comparison of the behavior of the seismic attributes of the surface waves between synthetic and real seismic data. The surface-waves propagation depends strongly on the near-surface structure. From results, it is shown that the greater complexity of the velocity model in the near-surface, the greater complexity of the surface-waves propagation. Some seismic attributes allow to enhance specific features associated to specific surface-waves phenomena. Moreover, the seismic attributes behavior tends to be the same in both, the synthetic and real data. The differences between synthetic and real experiments are due to the velocity models are different in each case.

Chapter 6

Conclusions and Future Works

In this work, we supplied a way to obtain synthetic multi-component seismic data with realistic ground roll. We implemented a 2D finite difference elastic wave propagation modeling using velocity models with irregular near-surface to compute the synthetic seismic data, which were contrasted with field data by comparing the behavior of seismic attributes computed from both synthetic and field data. The comparison showed that the principal features of ground roll present in the field data, which were acquired in Colombia, were reproduced in the synthetic data.

The main conclusions obtained during the develop of the project and the future works that would give continuity to this work are presented below.

6.1 Conclusions

- Ground roll is a broad concept that involves the mixture of a variety of seismic-wave types that propagate close to the earth surface. Among these seismic-wave types we can find: Rayleigh waves, higher modes of Rayleigh waves, scattering, S-wave refractions and reverberations. From seismic attributes analysis (polarization and planarity), it is shown that the mixture of these wave-types causes ground roll to propagate in more than one preferential plane, and each polarization plane depends on the angle of arrival of each of the scattering waves. This is the principal reason by which polarization filters has a low performance when they are probed in field data.

- A methodology to select the best seismic attributes to detect and classify surface waves in multicomponent seismic records was designed. The methodology uses machine learning tools to ensure the optimization of the process by minimizing the error in the detection and classification of surface waves. The set of seismic attributes selected

may change depending on the type of the seismic record, because the features of the seismic waves vary in accordance with the acquisition-type and the land-zone of study.

- A 2D finite differences method with second order accuracy in time and fourth order accuracy in space to model elastic wave propagation in presence of free-surface topography was implemented. The surface topography is contemplated in the earth models aiming to produce realistic seismic data. We use the improved vacuum formulation, which is based in the parameter averaging scheme, in order to solve the free-traction condition in the surface topography. The implemented method requires a number of points per wavelength higher than conventional modeling to ensure accurate Rayleigh wave, resulting in a higher computational cost. The advantage of this method is the capacity of adaptive with the shape of the surface topography without considerably alter the numerical solution.

- Several synthetic experiments of surface waves propagation through earth models with irregular near-surface to obtain realistic ground roll were developed. In total, thirteen simulations of seismic wave propagation experiments were performed, which were organized in four different types of experiments. Irregular-topography effect, soil-column effect, irregular-bedrock effect, soil-column and irregular-topography effect. From the results of each experiment and the seismic attribute analysis, we can conclude that: The higher variations in the surface topography, the higher scattered energy; the thinner soil-column layer, the higher the Rayleigh waves dispersion and; the greater thickness variation of the soil-column layer, the higher scattered and backscattered surface waves.

- A comparison of the behavior of the seismic attributes of the surface waves, between synthetic and real seismic data to analyze how realistic is the simulated ground-roll, was performed. In general, the seismic attributes behavior in the synthetic data is similar to the behavior in the field data. Some attributes allow to enhance specific features of surface-waves phenomena. The differences between the synthetic data and the field data are because the velocity models used are different in each case. The true velocity model is unknown and the synthetic velocity models were not designed from field data. The synthetic velocity models were made up exclusively for showing the dependence of the surface-waves propagation on the near-surface structure. From the experiments, it is shown that the dispersion, the scattering and the backscattering of surface waves is caused by the surface topography and irregular bedrock.

6.2 Future works

- To design adaptive polarization filters that taken into account more than one attribute. The filter should have the skill to set its parameters in each one of the zones in the seismic gather and to act according to the features of the data in each zone. We suggest to evaluate the designed filter with the synthetic seismic data computed in this work, by increasing the complexity of the data and analyzing the filter performance in each case.

- To make a comparison of different methods of pattern recognition in order to select the method that ensures the best detection and classification of surface waves in multicomponent seismic data. In our work, we use *k*-means, our suggestion is to probe with other methods using the both approaches supervised and unsupervised learning.

- To use multi-station attributes in order to extract information of wave propagation velocity from seismic data, since the attributes used, which were computed trace by trace, do not contain velocity information. We suggest the use of the Radon transform since it allows to transform the information of parabolas in the time-space domain to points in the $\tau - \pi$ domain.

- To extend to 3D elastic wave modeling to compute the transverse component of seismic data. For this it is suggested to make a variable mesh of the velocity models, being finer in the proximities to the surface with complex topography, in such a way as to assure the accuracy of the computation of surface waves and the implementation viability in the computational tools available in the research group and the University.

- To study the feasibility of using 3D elastic wave modeling with the spectral-element method in the computational tools available in the research group and the University. According to the state of the art, this method ensures the accuracy of the computation of the propagation of seismic waves in media with complex topography, but at a high computational cost. A tool called SPECFEM3D allows to model seismic waves using the spectral-element method, it is provided by the *Theoretical and Computational Seismology* research group at Princeton University and it can be downloaded for free following the steps in this link http://geodynamics.org/cig/software/specfem3d/.

- To add scattering points in velocity models in order to study, by means of seismic attributes, the effect of scattering points on the propagation of surface waves. Scattering points can be added using wide impedance contrasts in the velocity model. In

[Almuhaidib and Toksöz, 2014], it is established that these scattering points cause scattering with body-to-surface and surface-to-body conversions.

- The next big step in this research is to solve the inverse problem by designing a method of inversion of surface waves that uses misfit functions based on the information extracted by seismic attributes from multicomponent seismic data. To do this work we suggest making the previous future works.

Bibliography

[Almuhaidib and Toksöz, 2014] Almuhaidib, A. M. and Toksöz, M. N. (2014). Numerical modeling of elastic-wave scattering by near-surface heterogeneities. *Geophysics*, 79(4):T199–T217.

[Almuhaidib and Toksöz, 2015] Almuhaidib, A. M. and Toksöz, M. N. (2015). Finite difference elastic wave modeling with an irregular free surface using ader scheme. *Journal of Geophysics and Engineering*, 12(3):435.

[Bai and Kennett, 2000] Bai, C.-y. and Kennett, B. (2000). Automatic phase-detection and identification by full use of a single three-component broadband seismogram. *Bulletin of the Seismological Society of America*, 90(1):187–198.

[Bear et al., 1999] Bear, L. K., Pavlis, G. L., and Bokelmann, G. H. (1999). Multi-wavelet analysis of three-component seismic arrays: Application to measure effective anisotropy at pinon flats, california. *Bulletin of the Seismological Society of America*, 89(3):693–705.

[Berenger, 1994] Berenger, J.-P. (1994). A perfectly matched layer for the absorption of electromagnetic waves. *Journal of computational physics*, 114(2):185–200.

[Berg et al., 1994] Berg, P., If, F., Nielsen, P., and Skovgaard, O. (1994). Analytical reference solutions. *Modeling the earth for oil exploration*, pages 421–427.

[Bobbit, 1984] Bobbit, J. I. (1984). Three-componet rayleigh wave filter. *Society of Exploration Geophysicists*, 54:772–775.

[Chew and Liu, 1996] Chew, W. and Liu, Q. (1996). Perfectly matched layers for elastodynamics: a new absorbing boundary condition. *Journal of Computational Acoustics*, 4(04):341–359.

[Chiu et al., 2007] Chiu, S., Whitmore, N., and Gurch, M. (2007). Polarization filter by eigenimages and adaptive subtraction to attenuate surface-wave noise. *Proc. CSPG CSEG CWLS Conv*, pages 445–449.

[Chiu et al., 2008] Chiu, S. K., Howell, J. E., et al. (2008). Attenuation of coherent noise using localized-adaptive eigenimage filter. In *2008 SEG Annual Meeting*. Society of Exploration Geophysicists.

[Collino and Tsogka, 2001] Collino, F. and Tsogka, C. (2001). Application of the perfectly matched absorbing layer model to the linear elastodynamic problem in anisotropic heterogeneous media. *Geophysics*, 66(1):294–307.

[De Franco, 2001] De Franco, R. y Musacchio, G. (2001). Polarization filter with singular value decomposition. *Geophysics*, 66:932–938.

[De Meersman, 2008] De Meersman, K. (2008). Ground roll polarization filtering with spatial smoothness constraints. In *2008 SEG Annual Meeting*. Society of Exploration Geophysicists.

[de Meersman and Kendall, 2005] de Meersman, K. and Kendall, R. (2005). A complex svd-polarization filter for ground roll attenuation on multi-component data. In *67th EAGE Conference & Exhibition*.

[De Meersman et al., 2006] De Meersman, K., Van der Baan, M., and Kendall, J.-M. (2006). Signal extraction and automated polarization analysis of multicomponent array data. *Bulletin of the Seismological Society of America*, 96(6):2415–2430.

[Donno et al., 2006] Donno, D., Spagnolini, U., and Nehorai, A. (2006). Seismic shape parameters estimation and ground-roll suppression using vector-sensor beamforming. In *OCEANS 2006*, pages 1–6. IEEE.

[Filnn, 1965] Filnn, E. A. (1965). Signal analysis using rectilinearity and direction of particle. In *Proceedings of the IEEE*, number 53, pages 1874–1876, 10.1109/PROC.1965.4462.

[Foti et al., 2014] Foti, S., Lai, C., Rix, G., and Strobbia, C. (2014). *Surface Wave Methods for Near-Surface Site Characterization*. Taylor & Francis.

[Garvin, 1956] Garvin, W. (1956). Exact transient solution of the buried line source problem. In *Proceedings of the Royal Society of London A: Mathematical, Physical and Engineering Sciences*, volume 234, pages 528–541. The Royal Society.

[Gilbert and Knopoff, 1960] Gilbert, F. and Knopoff, L. (1960). Seismic scattering from topographic irregularities. *Journal of Geophysical Research*, 65(10):3437–3444.

[Hastings et al., 1996] Hastings, F. D., Schneider, J. B., and Broschat, S. L. (1996). Application of the perfectly matched layer (pml) absorbing boundary condition to elastic wave propagation. *The Journal of the Acoustical Society of America*, 100(5):3061–3069.

[Hestholm and Ruud, 1998] Hestholm, S. and Ruud, B. (1998). 3-d finite-difference elastic wave modeling including surface topography. *Geophysics*, 63(2):613–622.

[Honarkhah and Caers, 2010] Honarkhah, M. and Caers, J. (2010). Stochastic simulation of patterns using distance-based pattern modeling. *Mathematical Geosciences*, 42(5):487–517.

[Hudson and Knopoff, 1967] Hudson, J. and Knopoff, L. (1967). Statistical properties of rayleigh waves due to scattering by topography. *Bulletin of the Seismological Society of America*, 57(1):83–90.

[Jin and Ronen, 2005] Jin, S. and Ronen, S. (2005). Ground roll detection and attenuation by 3C polarization analysis. In *67th EAGE Conference & Exhibition*.

[Joswig, 1990] Joswig, M. (1990). Pattern recognition for earthquake detection. *Bulletin of the Seismological Society of America*, 80(1):170–186.

[Jurkevics, 1988] Jurkevics, A. (1988). Polarization analysis of three-component array data. *Bulletin of the Seismological Society of America*, 78(5):1725–1743.

[Kendall et al., 2005] Kendall, R., Jin, S., Ronen, S., and De Meersman, K. (2005). An svd-polarization filter for ground roll attenuation on multicomponent data. In *EAGE/SEG Research Workshop-Multicomponent Seismic-Past, Present and Future*.

[Köhler et al., 2008] Köhler, A., Ohrnberger, M., Riggelsen, C., and Scherbaum, F. (2008). Unsupervised feature selection for pattern search in seismic time series. In *Journal of Machine Learning Research. In: Workshop and Conference Proceedings: New Challenges for Feature Selection in Data Mining and Knowledge Discovery*, volume 4, pages 106–121.

[Köhler et al., 2010] Köhler, A., Ohrnberger, M., and Scherbaum, F. (2010). Unsupervised pattern recognition in continuous seismic wavefield records using self-organizing maps. *Geophysical Journal International*, 182(3):1619–1630.

[Komatitsch and Martin, 2007] Komatitsch, D. and Martin, R. (2007). An unsplit convolutional perfectly matched layer improved at grazing incidence for the seismic wave equation. *Geophysics*, 72(5):SM155–SM167.

[Kragh and Peardon, 1995] Kragh, E. and Peardon, L. (1995). Ground roll and polarization. *First Break*, 13(9):369–378.

[Lai and Rix, 1998] Lai, C. G. and Rix, G. J. (1998). *Simultaneous inversion of Rayleigh phase velocity and attenuation for near-surface site characterization*. PhD thesis.

[Levander, 1990] Levander, A. R. (1990). Seismic scattering near the earth's surface. *Pure and Applied Geophysics*, 132(1-2):21–47.

[Lines et al., 1999] Lines, L. R., Slawinski, R., and Bording, R. P. (1999). A recipe for stability of finite-difference wave-equation computations. *Geophysics*, 64(3):967–969.

[Liu, 1999] Liu, X. (1999). Ground roll supression using the karhunen-loeve transform. *Geophysics*, 62 (2):564–566.

[Lombard et al., 2008] Lombard, B., Piraux, J., Gélis, C., and Virieux, J. (2008). Free and smooth boundaries in 2-d finite-difference schemes for transient elastic waves. *Geophysical Journal International*, 172(1):252–261.

[Lowrie, 2007] Lowrie, W. (2007). *Fundamentals of Geophysical*. Cambridge University Press.

[M. et al., 1991] M., J. G., M., M. I., and A., G. S. (1991). Principal component transforms of triaxial recordings by singular value decomposition. *Geophysics*, 56:528–533.

[Mars et al., 2004] Mars, J., Glangeaud, F., and Mari, J. (2004). Advanced signal processing tools for dispersive waves. *Near Surface Geophysics*, 2(4):199–210.

[Martel et al., 1977] Martel, L., Munasinghe, M., and Farnell, G. (1977). Transmission and reflection of rayleigh wave through a step. *Bulletin of the Seismological Society of America*, 67(5):1277–1290.

[Moczo et al., 2014] Moczo, P., Kristek, J., and Gális, M. (2014). *The finite-difference modelling of earthquake motions: Waves and ruptures*. Cambridge University Press.

[Moczo et al., 2002] Moczo, P., Kristek, J., Vavryčuk, V., Archuleta, R. J., and Halada, L. (2002). 3d heterogeneous staggered-grid finite-difference modeling of seismic motion with volume harmonic and arithmetic averaging of elastic moduli and densities. *Bulletin of the Seismological Society of America*, 92(8):3042–3066.

[Moczo et al., 2007] Moczo, P., Robertsson, J. O., and Eisner, L. (2007). The finite-difference time-domain method for modeling of seismic wave propagation. *Advances in Geophysics*, 48:421–516.

[Morozov and Smithson, 1996] Morozov, I. B. and Smithson, S. B. (1996). Instantaneous polarization attributes and directional filtering. *Geophysics*, 61(3):872–881.

[Ohrnberger, 2001] Ohrnberger, M. (2001). Continuous automatic classification of seismic signals of volcanic origin at mt. merapi, java, indonesia.

[Perelberg and Hornbostel, 1994] Perelberg, A. I. and Hornbostel, S. C. (1994). Applications of seismic polarization analysis. *Geophysics*, 59(1):119–130.

[Pinnegar, 2006] Pinnegar, C. (2006). Polarization analysis and polarization filtering of three component signals with the time frequency S transform. *Geophysical Journal International*, 165(2):596–606.

[Riggelsen et al., 2007] Riggelsen, C., Ohrnberger, M., and Scherbaum, F. (2007). Dynamic bayesian networks for real-time classification of seismic signals. In *European Conference on Principles of Data Mining and Knowledge Discovery*, pages 565–572. Springer.

[Robertsson, 1996] Robertsson, J. O. (1996). A numerical free-surface condition for elastic/viscoelastic finite-difference modeling in the presence of topography. *Geophysics*, 61(6):1921–1934.

[Samson and Olson, 1981] Samson, J. and Olson, J. (1981). Data-adaptive polarization filters for multichannel geophysical data. *Geophysics*, 46(10):1423–1431.

[Sheriff, 2002] Sheriff, R. E. (2002). Encyclopedic dictionary of applied geophysics.

[Shieh and Herrmann, 1990] Shieh, C.-F. and Herrmann, R. B. (1990). Ground roll: Rejection using polarization filters. *Geophysics*, 55(9):1216–1222.

[Sánchez et al., 2016] Sánchez, I. J., Serrano, J. O., Niño, C. A., Sierra, D. A., and Agudelo, W. A. (2016). Svd polarization filter taking into account the planarity of ground roll energy. *Ciencia, Tecnología y Futuro*, 6(3):5–16.

[Solano et al., 2016] Solano, C. P., Donno, D., and Chauris, H. (2016). Finite-difference strategy for elastic wave modelling on curved staggered grids. *Computational Geosciences*, 20(1):245–264.

[Tiapkina et al., 2012] Tiapkina, O., Landrø, M., Tyapkin, Y., and Link, B. (2012). Single-station SVD-based polarization filtering of ground roll: Perfection and investigation of limitations and pitfalls. *Geophysics*, 77(2):V41–V59.

[Tokimatsu, 1995] Tokimatsu, K. (1995). Geotechnical site characterization using surface waves. *Proceedings of 1st International Conference on Earthquake Geotechnical Engineering*, 3(8):1333–1368.

[Vidale, 1986] Vidale, J. E. (1986). Complex polarization analysis of particle motion. *Bulletin of the Seismological society of America*, 76(5):1393–1405.

[Virieux, 1986] Virieux, J. (1986). P-SV wave propagation in heterogeneous media: Velocity-stress finite-difference method. *Geophysics*, 51(4):889–901.

[Yilmaz, 2001] Yilmaz, O. (2001). *Seismic Data Analysis: Processing, Inversion, and Interpretation of Seismic Data*, volume 2. Society Exploration Geophysicists.

[Yilmaz, 2015] Yilmaz, Ö. (2015). *Engineering Seismology with Applications to Geotechnical Engineering:*. Investigations in Geophysics. Society of Exploration Geophysicists.

[Zeng et al., 2012] Zeng, C., Xia, J., Miller, R. D., and Tsoflias, G. P. (2012). An improved vacuum formulation for 2d finite-difference modeling of rayleigh waves including surface topography and internal discontinuities. *Geophysics*, 77(1):T1–T9.

[Zhang and Chen, 2006] Zhang, W. and Chen, X. (2006). Traction image method for irregular free surface boundaries in finite difference seismic wave simulation. *Geophysical Journal International*, 167(1):337–353.

[Zhang et al., 2014] Zhang, Y., Xu, Y., Xia, J., Ping, P., and Zhang, S. (2014). On dispersive propagation of surface waves in patchy saturated porous media. *Wave Motion*, 51(8):1225–1236.